THERMODYNAMICS AND THERMAL−FLUID TRANSPORT OF A DUAL−STAGE SODIUM THERMAL ELECTROCHEMICAL CONVERTER (NA-TEC)

A Dissertation
Presented to
The Academic Faculty

by

Alexander Limia

In Partial Fulfillment
of the Requirements for the Degree
Doctor of Philosophy in the
George W. Woodruff School of Mechanical Engineering

Georgia Institute of Technology
August 2020

THERMODYNAMICS AND THERMAL−FLUID TRANSPORT OF A DUAL−STAGE THERMAL ELECTROCHEMICAL CONVERTER (NA−TEC)

Approved by:

Dr. Shannon K. Yee, Advisor
School of Mechanical Engineering
Georgia Institute of Technology

Dr. Thomas F. Fuller
School of Chemical and Biomolecular Engineering
Georgia Institute of Technology

Dr. Andrei G. Fedorov
School of Mechanical Engineering
Georgia Institute of Technology

Dr. Comas Haynes
Georgia Tech Research Institute
Georgia Institute of Technology

Dr. Seung Woo Lee
School of Mechanical Engineering
Georgia Institute of Technology

Date Approved: May 8, 2020

To my wife Valery D. Limia

And to my parents, Angélica M. Calderón and José Limia

ACKNOWLEDGEMENTS

First, I would like to thank my wife Valery D. Limia for all her love, patience, and support during my time in graduate school. I am blessed to have her invaluable presence in my life. I want to thank my mother Angélica M. Calderón for all the sacrifices she made to ensure that I could obtain the best possible education. She worked hard her entire life so that one day her son could partake in the American dream, and I am eternally grateful for her selfless love. I also thank my father José Limia, who endowed me with a desire for knowledge. Opportunities for a young man were limited in his native Cuba, so he prepared me well to take advantage of my different circumstances in Florida.

I am grateful to my advisor Dr. Shannon K. Yee, with whom I have explored the exciting field of electrochemical thermal energy conversion. I have learned much from him over the years, including proper laboratory procedures, how to think critically about my research, and the significant value of a good presentation. Most importantly, Shannon has always taken great interest in my personal and career development. I also want to express gratitude to my committee members: Dr. Andrei G. Fedorov, who challenged me to probe deeply into the fundamentals of my work and inspired me with his approach to scientific research; Dr. Seung Woo Lee, with whom I collaborated with on the Na-TEC project and who guided me well during the teaching practicum; Dr. Thomas F. Fuller, from whom I learned about many electrochemistry concepts; and Dr. Comas Haynes, who has been a great mentor to me through the Sloan program. I also thank Dr. Peter Kottke, who was pivotal in my progression through graduate school. I am grateful for his availability and patience with me as I sought to learn from his vast experience and insight.

I would like to thank all the past and current members of STEEL, including: Akanksha Menon, David Rodin, Sampath Kommandur, Patrick Creamer, Venkatesh Chinnakonda, Shawn Gregory, Shahin Shafiee, Bettina Arkhurst, Sonja Brankovic, Daron Spence, Jordan Kocher, Josh Rinehart, Amalie Atassi, and Frank Feng. I especially want to thank: Jong Min Ha, who was a dependable and selfless laboratory partner, along with being a great friend; Aravindh Rajan, who always pushed me think more critically and broadly about my research; and Dr. Andrey Gunawan, who helped advance much of my work and was always charitable with his time. I would also like to thank the various undergraduate students with whom I had the pleasure of working with: Andres Menendez, whose codes were instrumental for the Na-TEC modeling work; Daniel Silverstein, who gathered much of the data analyzed in Chapter 4; Nachiket Naik; Harsh Kaitan; Mariana Mendonça; Nicholas Tucker; Rhitesh Bhatt; and Saif Kabariti. I also thank the various friends I met in graduate school who made Atlanta feel more like home, especially: Alejandro Barrios, Garrett Schieber, Andrew Schrader, Evan Bush, Marc Papakyriakou, Kiarash Gordiz, the remaining "Exodus" crew (David Arellano, Esteban Carrillo, Samuel Petter), and Pol Llado.

I also wish to acknowledge various people from my time at the University of Miami. I thank Susie Picar, who encouraged me to fulfill my potential, convinced me to take worthy risks, and always showed me great kindness. I also thank Dr. Neil Johnson, Dr. Amir Rahmani, and Dr. Shihab Asfour, who gave me my first research opportunities; Dr. Kau Fui Wong, who taught me, in his unique manner, to appreciate the field of thermodynamics; and Dr. Howard Gordon, who was always available to give me academic and career advice. I also want to thank Dr. Evelyn Wang, Dr. Nenad Miljkovic, and Dr.

Daniel Preston, who advised me during the 2013 MIT Summer Research Program. This was the first time I conducted laboratory scale thermal-fluid research, and my memorable experience in their lab ultimately convinced me to pursue a graduate degree.

Finally, I would like to thank the Georgia Tech Catholic Center, and in particular Fr. Joshua Allen, for keeping me grounded and emboldening me to think more profoundly. My Christian faith is indispensable, and it was significantly nurtured throughout my time in graduate school. If I accomplished anything at all, may all the credit go to God who, undeserving as I may be, has placed so many people in my life which have helped me flourish.

TABLE OF CONTENTS

LIST OF TABLES

LIST OF FIGURES

LIST OF SYMBOLS AND ABBREVIATIONS

Latin

A	area [m^2]
A_c	cross-section area [m^2]
A_{lv}	liquid-vapor interface area [m^2]
A_{ls}	liquid-solid interface area [m^2]
A_p	projected interface cross-section area [m^2]
A_{sv}	solid-vapor interface area [m^2]
B	temperature independent exchange current density [$A\ K^{1/2}\ N^{-1}$]
Br	Brinkmann number, $u_0^2\mu/k_{eff}/T_0$
Bo	Bond number
C_A	Na-TEC areal costs [$]
c_f	Forchheimer form drag coefficient
c_p	specific heat at constant pressure [J/kg/K]
C_V	Na-TEC volumetric costs [$]
$C_\$$	total Na-TEC cost ($C_\$ = C_A + C_V$) [$]
d	diameter [m]
D_K	Knudsen diffusion coefficient [m^2/s]
D_O	ordinary diffusion coefficient [m^2/s]
D_{ij}	binary diffusion coefficient [m^2/s]
D_p	solid diameter (sphere, cylinder) [m]
d_p	pore diameter [m]

e	ellipse eccentricity
F	Faraday's constant [96485 c/mol]
$\vec{F}$	interfacial force [N]
f	parasitic heat loss fraction $\dot{Q}''_{loss}/\dot{Q}''_{in}$, generic function
$F_{1\text{-}2}$	radiation view factor
G	morphology factor
$Gr_{\sqrt{\kappa}}$	modified Grashof number, $\beta(T-T_\infty)\rho^2\kappa^{3/2}/\mu^2$
h	height of corrugated unit [m]
h_{fg}	latent heat of vaporization [J/kg/K]
I	current [A]
j	current density [A cm^{-2}]
j_0	exchange current density [A cm^{-2}]
j_1	first-stage current density [A cm^{-2}]
j_{lim}	limiting current density [A cm^{-2}]
j_{sc}	short circuit current density [A cm^{-2}]
k	thermal conductivity [W/m-K]
K_{12}	surface curvature [m^{-1}]
k_{eff}	effective thermal conductivity [W/m-K]
Kn	Knudsen number
K_{PB}	total power block cost ($C_\$/W_e$) [$/W]
L	length of liquid-return path, characteristic length [m]
L_e	electrode thickness
L_{elec}	distance between electrodes [m]

L_{ev}	evaporator diffusion length [m]
L_{ex}	experimental coupon length [m]
L_{ls}	liquid-solid interface length [m]
L_{lv}	liquid-vapor interface length [m]
L_p	L_{lv} - $L_{ls}\,cos\,\theta_{ca}$ [m]
L_{pc}	porous coupon length [m]
l_{tot}	length for conduction heat transfer [m]
m	counting variable (2:5)
M	sodium molar mass [22.98 g/mol]
$\dot{m}$	mass flowrate [kg/s]
$\dot{m}_{max}$	maximum mass flowrate [kg/s]
M_{Ar}	argon molar mass, 39.95 [g]
n	counting variable (1:4)
N	Number: engines, Zone 3 corrugated units, external shields, cylindrical shields
N_{seg}	number of electrolyte segments
Nu	Nusselt number
P	pressure [Pa]
P_{atm}	atmosphere pressure [Pa]
Pe	Peclet number
P_i	gas partial pressure (i = Na, Ar) [Pa]
P_L	breakthrough/Laplace gauge pressure [kPa]
P_{loss}	pressure loss [Pa]
Pr	Prandtl number

P_{sat}	saturation pressure [Pa]
P_w	sodium vapor saturation pressure at the wall [Pa]
Q	heat [W]
$\dot{Q}''_{in}$	heat input [W m^{-2}]
$\dot{Q}''_{loss}$	parasitic heat loss [W m^{-2}]
$\bar{R}$	universal gas constant [8.314 J/kg/K]
r_a	inner radius [m]
r_b	outer radius [m]
R_c	conduction thermal resistance [K/W]
r_{ct}	charge transfer resistance [Ω]
R_{eq}	equivalent thermal resistance [K m^2 W^{-1}]
R_K	Knudsen flow mass transfer resistance [m/s]
r_{load}	external load resistance [Ω]
R_{mass}	mass transfer resistance [m/s]
R_{rad}	radiation thermal resistance [K/W]
r_{Th}	Thevenin-equivalent ohmic resistance [Ω cm^2]
R_{th}	total thermal resistance [K/W]
R_v	viscous flow mass transfer resistance [m/s]
Re_x	Reynold's number, $\rho u_D x/\mu$
S	supersaturation of sodium vapor, $P_{Na}/P_{sat}(T_w)$
SS 316	stainless steel 316
T	temperature [^{o}C, K]
t	thickness [m]

T_{cond} condenser temperature [^{o}C, K]

T_{evap} evaporator, evaporator interface temperature [^{o}C, K]

$t_{gap,h}$ axial direction thickness of the corrugated unit [m]

$t_{gap,v}$ axial direction thickness of the corrugated unit [m]

T_H average hot-side temperature [^{o}C, K]

T_{in} porous insert inlet temperature [°C, K]

T_{int} intermediate temperature [^{o}C, K]

T_{out} condensation interface temperature [°C, K]

t_{tot} total experiment time [hours]

T_w solid wall temperature [°C, K]

t_{wait} experimental wait time [s, hours]

T_∞ environment temperature [°C, K]

u absolute velocity [m/s]

u_D Darcy velocity [m/s]

V voltage [V], volume [m^3]

V_1 volume in upper flange [m^3]

W_e electrical power [W]

x axial distance [m]

Greek

α sphere packing angle, parallelogram acute angle

β volumetric thermal expansion coefficient [K^{-1}]

β_1, β_2 empirical fitting parameters

ΔP_{inc} experiment pressure increment

ΔV	volume between electrodes
δ	uncertainty
δs	differential length [m]
ε	surface emissivity
ζ	geometric parameter for a parallelogram
η	thermal efficiency
η_{reg}	regeneration efficiency
θ_{ca}	contact angle
κ	permeability [m^2]
λ	geometric parameter for packed spheres
μ	dynamic viscosity [Pa·s]
ξ	overpotential [V]
ρ	density [kg m^{-3}]
σ	Stefan-Boltzmann constant [$5.67 \cdot 10^{-8}$ W m^{-4} K^{-1}]
σ_{lv}	surface tension [N/m]
σ_{ls}	liquid-solid surface energy [J/m^2]
σ_{sv}	solid-vapor surface energy [J/m^2]
σ_{β}	ionic conductivity of β"-alumina [Ω^{-1} m^{-1}]
τ	porous structure tortuosity
φ	porosity
ψ	angle defined for a packed sphere geometry
ω	mass fraction

Subscript

0	characteristic property of the system
1	first stage in dual-stage Na-TEC
2	second stage in dual-stage Na-TEC
316	stainless Steel 316
a	anode
Ar	argon
c	cathode
cs	cylindrical shield (Zone 4)
cond	condenser
eff	effective property
es	external shield (Zone 3)
ev	geometric average along evaporator $-L_{ev} < x < 0$
evap	evaporator
f	fluid (liquid or gas)
g	gas
i	represents anode or cathode, counting variable
j	counting variable
l	liquid
meas	experimentally measured value
Na	Sodium
oc	open-circuit
pc	geometric average in porous coupon $L_{ex} - L_{pc} < x < L_{ex}$

pi	geometric average in porous insert $0 < x < L_{ex} - L_{pc}$
rad	radiation
spk	spoke
s	solid
V	vanadium
Z(i)	i^{th} zone property
β	β”-alumina electrolyte

SUMMARY

The sodium thermal electrochemical converter (Na-TEC) is a heat engine that generates electricity through the isothermal expansion of sodium ions within a β''-alumina solid-electrolyte. The Na-TEC can thermodynamically achieve conversion efficiencies above 45% when operating between thermal reservoirs at 1150 K and 550 K. However, thermal management limitations have constrained previous single-stage devices to thermal efficiencies below 20%. To mitigate these limitations, the isothermal expansion can be divided into two stages: one at the evaporator temperature and another at an intermediate temperature (650 K – 1050 K). This dual-stage Na-TEC takes advantage of regeneration and reheating, and could be amenable to improved thermal management through a reduction of parasitic losses. This dissertation investigates the thermodynamic operating limits of a dual-stage Na-TEC. The dual-stage device is shown to improve the thermal efficiency by up to 7.5% points over the best performing single-stage device. An application regime map for the single- and dual-stage Na-TEC in terms of the power density and the total parasitic loss is also established. Finally, a reduced-order thermal model is used to analyze the performance of a quasi-axisymmetric dual-stage Na-TEC design with a maximum thermal efficiency of 29%.

This dissertation also explores the liquid-pumping subcomponent of the Na-TEC, which consists of a capillary wick in the high-temperature evaporator used to generate the driving force. Sodium corrosion at high temperature leads to several degradation mechanisms that reduce the long-term performance of the Na-TEC. To enable low-temperature pumping solutions, a unique sodium capillary pump for the Na-TEC is

explored, whereby low-pressure sodium vapor is condensed within a non-wetting stainless steel porous structure. A net force at the solid-liquid-vapor interface effectively pushes liquid sodium towards a high-pressure bulk liquid region, in contrast to traditional evaporator wicks. First, a breakthrough pressure experiment is used to measure the temperature-dependent interfacial pressure of liquid sodium on the stainless steel porous structure. These results quantify the maximum pressure that can be sustained by the interface at various temperatures, and the wetting transition temperature can be linearly extrapolated from the data. A separate experiment is then conducted to study the performance (mass flowrate vs. pressure head) of this capillary pumping mechanism. To guide the operation of this experiment, a conjugate transport model is developed to characterize sodium vapor diffusion within the porous structure. Results demonstrating the potential for liquid sodium pumping with this mechanism are discussed in detail. Experimental uncertainties for both experiments are addressed, and future improvements are considered.

CHAPTER 1. INTRODUCTION

1.1 Introduction to the Na-TEC

1.1.1 Motivation

Annual residential energy consumption is expected to increase 8% in OECD countries and 87% in non-OECD countries from 2020 to 2050, rising globally from about 59.8 quadrillion Btu to 90.5 quadrillion Btu.[1] The majority of this energy will be delivered in the form of electricity (global electrical demand is expected to grow by 2.5% yearly). Most electricity is currently generated in centralized thermal power plants, but as electric grids modernize to meet the expected rise in demand, distributed power generation will become more prominent because it can improve grid reliability, enable energy storage, and accommodate carbon-free alternatives (*e.g.*, solar, wind). Combined heat and power (CHP) systems generate electricity and thermal energy simultaneously, and they represent a potential solution for distributed energy needs. The majority of deployed CHP systems in the United States consist of gas and steam turbines, but several other technologies are under development for this application, including micro-turbines, fuel cells, and thermally regenerative electrochemical systems (TRES). The latter are steady-state, closed systems that use heat to drive an electrochemical reaction.[2] This dissertation focuses on one specific type of TRES, a sodium thermal electrochemical converter (Na-TEC), which can provide a solution for small CHP systems in the 1-10 kW range while using a variety of fuel sources.

1.1.2 Fundamental Operating Principles of the Na-TEC

The sodium thermal electrochemical converter (Na-TEC) converts heat directly into electricity using the isothermal expansion of sodium ions through an electrode-electrolyte assembly. The key component in the operation of the Na-TEC is a sodium ion-conducting solid-electrolyte known as β''-alumina ($Na_2O{\bullet}MgO{\bullet}5Al_2O_3$).[3] β''-alumina consists of a layered structure of γ-phase Al_2O_3 blocks separated by monolayer thick ionic conduction planes populated with Na_2O (Figure 1.1), and it is stabilized with MgO.[4] This electrolyte allows the preferential transport of sodium cations, thereby enabling the direct conversion of heat into electricity as sodium ions isothermally expand from a region of high chemical potential to a region of low chemical potential.

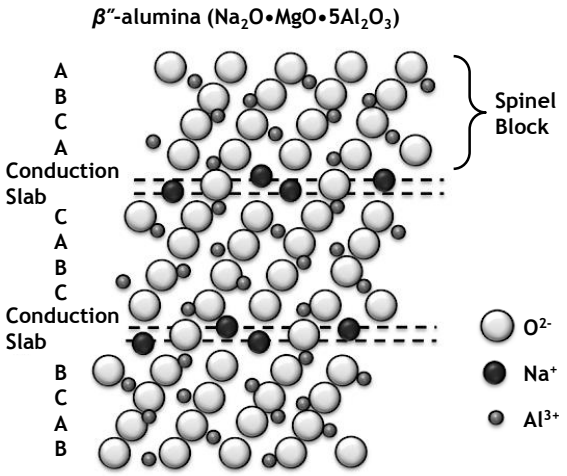

Figure 1.1 Crystal structure of β″-alumina in the $\mathbf{11\bar{2}0}$ plane, demonstrating spinel blocks separated by conduction slabs. MgO is not depicted. Adapted from ref. [5]

The reversible thermodynamic operation of a single-stage Na-TEC has been introduced previously [6] and is depicted in Figure 1.2a. In single-stage operation, liquid sodium enters a high temperature evaporator ($T_{evap} \approx 1150$ K) where it is heated and

vaporized just below its boiling point. The sodium vapor moves through a porous (inert) anode, forming a triple phase boundary (Na-electrode-electrolyte) where sodium is oxidized.[7] A vapor pressure difference between the high temperature evaporator plenum and the lower temperature condenser plenum ($T_{cond} \approx 500$ K) establishes an electrochemical potential gradient across the β''-alumina that drives the sodium cation conduction. Simultaneously, the electrons travel through an external load where power is extracted. The electrons and sodium cations then recombine at a porous (inert) cathode to form low pressure sodium vapor. For a thin, high aspect ratio solid-electrolyte, the transfer of sodium from the high to low pressure region can be modeled as an isothermal expansion of sodium vapor. For this internally reversible and isothermal process, the power output caused by the flow of electric current is supported by the heat input to the electrolyte. The low-pressure vapor is then sensibly cooled and condenses to a liquid. The liquid sodium is pumped back into the evaporator to complete the thermodynamic cycle. The ideal thermodynamic cycle can be modeled using six internally reversible processes: (1)-(2) isobaric liquid heating, (2)-(3) vaporization, (3)-(4) isothermal ion expansion through the electrolyte which generates work, (4)-(5) isobaric vapor cooling, (5)-(6) condensation, and (6)-(1) isentropic pumping. Figure 1.2b shows this thermodynamic cycle in temperature-entropy coordinates. Process (3)-(4) in the T-S diagram demonstrates the similarity of this cycle to the highly efficient Ericsson cycle.[8]

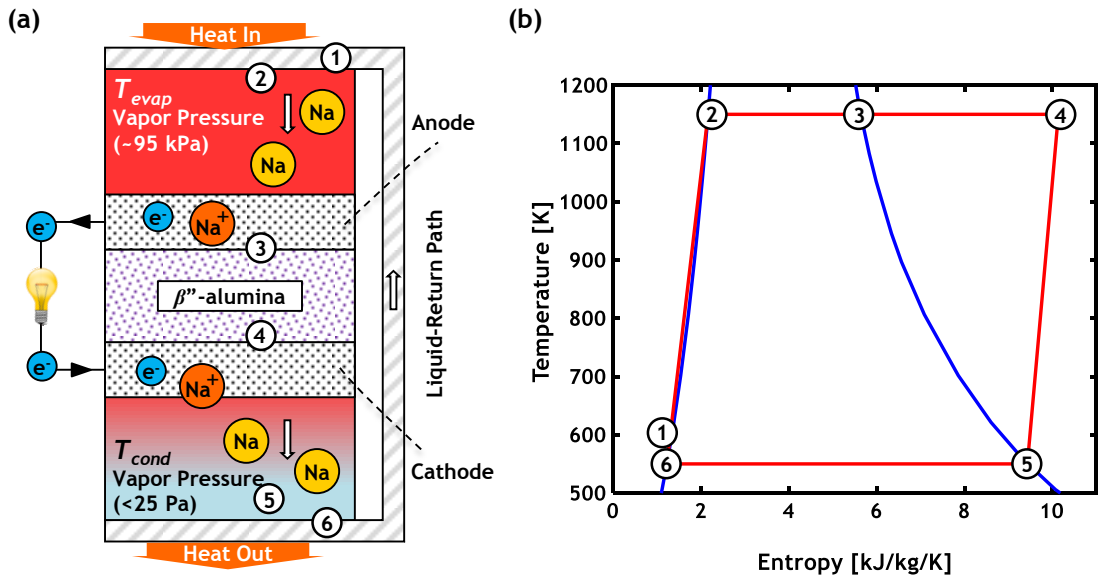

Figure 1.2 (a) Schematic illustration of a single-stage Na-TEC. (b) Temperature-Entropy (T-S) diagram of the ideal dual-stage Na-TEC thermodynamic cycle (red lines) overlaid on top of the sodium saturation curves (blue lines), where each number corresponds to a state of the system.

The Na-TEC is an attractive TRES because it can theoretically achieve > 90% of the Carnot efficiency for all ranges of operating temperatures.[9] Some of the advantages of the Na-TEC include its: (i) high operating temperature, which leads to a high theoretical thermal efficiency compared to other TRES (upwards of 45% for a system operating between thermal reservoirs at 1150 K and 550 K), (ii) high specific power density (in the range of 0.1 kW/kg_{Na}), (iii) scalability to multiple power outputs (typically in the range of 100 W to 10 kW per module), (iv) ability to provide high-grade process cogeneration heat, (v) flexibility with heat source (concentrated solar power, radioisotope generator, *etc.*).[10, 11] The thermal efficiency of the Na-TEC competes with several diverse technologies (*e.g.*, single-junction photovoltaics, combustion engines, thermionics) while operating at lower temperature ratios (Figure 1.3a). However, it is surpassed by traditional power generation cycles (*e.g.*, Rankine), which are designed to operate at much larger scales. The specific

power and the power density of the Na-TEC (Figure 1.3b) can exceed those of many solid-state generators like photovoltaics, thermoelectrics, and other electrochemical technologies (*e.g.*, fuel cells).

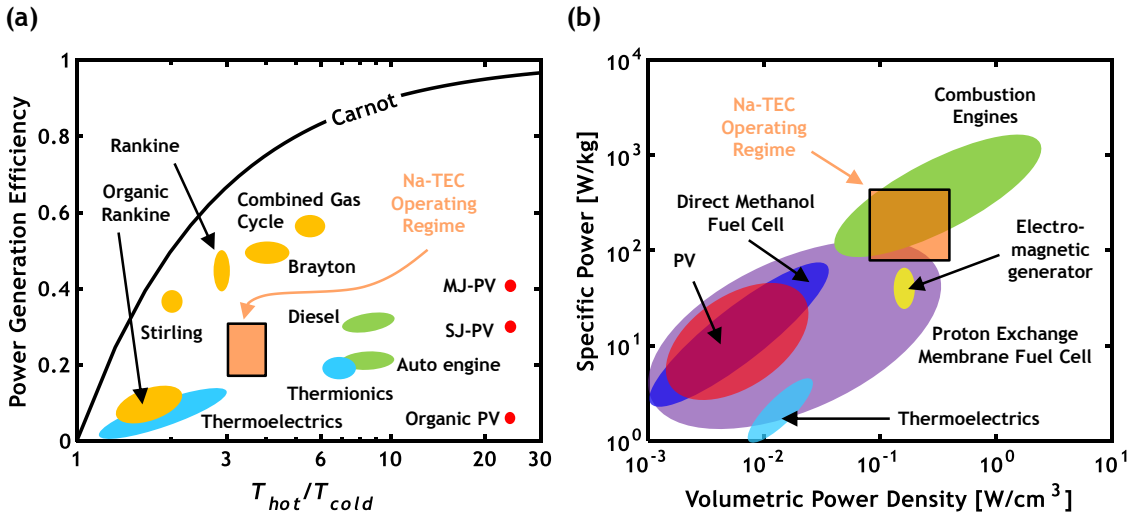

Figure 1.3 (a) Power generation efficiency vs. temperature ratio (between hot and cold reservoirs) for various technologies. PV is photovoltaic, SJ-PV is single-junction photovoltaic, and MJ-PV is multi-junction photovoltaic. Na-TEC efficiency range assumes the use of a dual-stage device (see Chapter 2, 3). Adapted from ref. [12, 13]. (b) Specific power vs. volumetric power density for various technologies. Adapted from ref. [14]

1.2 Review of Previous Na-TEC Research

1.2.1 Historical Development of the Na-TEC

This technology was originally conceived in 1968 at Ford Scientific Laboratory under the name "sodium heat engine".[15] Early work by Weber and Cole described the foundational thermodynamic principles used to analyze the thermal efficiency and the total power generated by this technology, and the device was rebranded as the alkali metal thermoelectric converter (AMTEC).[6, 16] In the 1980's, the Jet Propulsion Laboratory began to consider the feasibility of using AMTEC as the power-generating block for

unmanned spacecraft.[17] In 1990, two seminal papers were published from this laboratory in which a detailed electrochemical model for the AMTEC is developed; this model continues to be used in most AMTEC analyses.[18, 19] In earlier experiments, sodium was typically allowed to condense on the anode-side of the electrolyte to act as the current-carrying electrode, but in 1992 a vapor-fed AMTEC cell was conceptualized to increase the voltage and ameliorate many long term material challenges with liquid-anode operation.[20] Throughout the 1990's, the technological development of the AMTEC was accelerated to satisfy the mission power requirements for the Pluto Express Fly-By spacecraft.[21] The PX-series AMTEC cells were developed by Advanced Modular Power Systems, and comprehensive modeling was undertaken by Phillip's Laboratory and the Institute for Space and Nuclear Power Studies at the University of New Mexico.[22] Results for functioning PX-3 and PX-5 AMTEC cells are summarized by Merrill and Mayberry.[23] A comprehensive review of the development of the AMTEC was published by Wu *et al.* in 2009.[11] The practical thermal efficiency of AMTECs have approached 20% for systems operating with evaporator temperatures of 1150-1050 K and condenser temperatures of 625-550 K (Carnot efficiencies > 40%). For example, a thermal efficiency of 19% for a device running > 3,000 hours was achieved in 1981 through a collaboration between Ford and NASA.[24] Later on, a maximum efficiency of 15% was reported in 1998 by Merrill *et al.* for a PX-3A cell developed for the NASA Pluto/Express mission.[25]

More recent efforts in Na-TEC (*i.e.,* AMTEC) research primarily involve the optimization of the device performance by using novel materials, the integration of the device into broader energy systems, and numerical simulations of Na-TEC transport processes. For example, one study considered a Na-TEC coupled to a thermoelectric

bottoming cycle for co-generation in modular nuclear power plants.[26] Another study considers a hybrid system that uses the heat released from sodium condensation to power a triple-effect absorption refrigerator.[27] A group at the Karlsruhe Institute of Technology in Germany built an AMTEC test facility (ATEFA) capable of reaching up to 1275 K.[28] This group studied the feasibility of using AMTEC for a concentrated solar power plant, and demonstrated a pathway to produce 2 MW of electric power.[29] Recent studies have also studied the potential for Na-TEC to recover the waste heat from direct-carbon fuel cells (*e.g.*, molten carbonate fuel cells).[30, 31]

1.2.2 Thermal Modeling of the Na-TEC

Several thermal modeling efforts have been undertaken for the Na-TEC. One of the earliest detailed thermal models was for an AMTEC recirculating test cell, which uses an explicit solution scheme to calculate the temperature field.[32] Orbital Sciences Corporation later developed a comprehensive thermal and electrical model for multi-tube AMTEC cells which relies on a SINDA thermal analyzer code coupled to the ITAS radiation interchange code to calculate radiation view factors.[33] Extensive parametric modeling work was also undertaken by Lodhi's group at Texas Tech University, which included an optimization of the geometric dimensions and material properties of the PX-3A cell for increased thermal efficiency, and a thermal circuit analysis for a Na-TEC coupled to a thermionic energy converter.[34-36] Reduced-order thermal models have been developed for coupled Na-TEC systems, including a radial cell designed to deliver 50 kW with an efficiency of 22%, and a cell combined with a parabolic-dish solar collector delivering 18.5 kW with an overall efficiency of 20.6%.[37, 38] A thermal resistance model was recently used to optimize a Na-TEC (through the electrolyte dimensions and the wick

parameters) to produce 100 W.[39] Furthermore, following the initial conceptualization of a Scalable AMTEC Integrated Reactor Space-powered system (SAIRS) [40], a new lumped-parameter model (TAPIRS) has been developed to study the in-orbit failure modes and the transient response to a load-demand shift for this system.[41, 42]

The most detailed and extensive physical modeling effort undertaken for the Na-TEC is the AMTEC Performance and Evaluation Analysis Model (APEAM) developed to study the performance of the PX-series cells by Tournier and El-Genk.[43] APEAM consists of three sub-models: a sodium vapor pressure loss model, a cell electrical model, and a radiation/conduction heat transfer model.[44-46] APEAM was benchmarked against experimental results for the PX-3A cells and it estimates a maximum thermal efficiency of 22.5% with a power output of 9.7 W, assuming a number of reasonable engineering design modifications are applied.[47] Focusing specifically on thermal considerations, their radiation/conduction sub-model assumes that all structural surfaces are gray and diffuse, and it approximates all view factors using a combined algebraic/numerical approach.[48] After applying the appropriate boundary conditions, the PX cell geometry is discretized into > 100 nodes, reciprocity and enclosure relations are satisfied, and the temperature of each node is found using Gauss-Jordan elimination.[46] A similar approach is used to study how the cell performance is affected by the angle of an axisymmetric conical evaporator standoff.[49] Following upon the APEAM framework, a lumped thermal-electrochemical model was developed by idealizing the interior of a PX-3A cell as a network of three closed surfaces.[50] This model was recently updated to incorporate Monte-Carlo ray tracing, and it was validated against data from a PX-3A cell.[51]

1.2.3 Liquid Sodium Pumping in the Na-TEC

Liquid sodium in the Na-TEC condenser is pumped back into the high pressure evaporator using an electromagnetic pump or a capillary mechanism.[11] Capillary wicks for sodium recirculation in a Na-TEC cell are passive by nature, allowing for improved efficiency by removing the power requirements for an electromagnetic pump. Some of the first capillary wicks for zero-G operation were tested at high temperatures within a fully operating single-tube cell.[52] Experiments continued on these wick return cells, demonstrating their durability at temperatures between 875 K-1013 K.[53] Four main elements of wick design were identified: grooves for liquid sodium collection, drainage holes, transport arteries, and porous wicks to sustain the interface at the evaporator.[54] Creare Inc. later developed a micromachined condenser with surface contours to enhance the spreading of sodium drops on the condensing surface.[55] Given the low emissivity of liquid sodium [56], this spreading reduces parasitic radiative losses as liquid sodium coats the condenser. Na-TEC cells using this new wick achieved conversion efficiencies up to 15%.[56]

A systematic optimization of the liquid sodium return wick for PX-series cells was performed by Tournier and El-Genk.[57] They suggested the use of a composite wick to account for the competing requirements of efficient liquid transport and a large capillary driving force. This same team developed a two-dimensional thermal-hydraulic model of the evaporator wick to determine the dryout limit, and integrated it to their successful APEAM model.[58] They report temperature and electric power operation limits ($T_{evap} \leq$ 1136 K, $W_e \leq 16$ W) to remain below the capillary limit. In 2012, Wu *et. al.* studied the effect of the working fluid and porous wick temperature on the flowrate and heat transfer

characteristics in the Na-TEC evaporator by employing an axisymmetric geometry and various effective thermal conductivity models.[59] They later developed a 3D numerical model to study the impact on the evaporation of sodium by adding a bayonet tube into a capillary pumped loop.[60] A recent parametric study incorporates radiative heat transfer within the low-pressure Na-TEC plenum to study the condensate film thickness and the Nusselt number as a function of radial position in the condenser.[61] Following on this work, these authors generalized a numerical approach to study condensation in the Na-TEC using the volume-of-fluid (VOF) approach.[62]

1.3 Scope of Present Work

This dissertation consists of five chapters following this introductory chapter, and has two key focus areas:

1) This thesis explores the thermodynamic operation and design of a dual-stage Na-TEC. The Na-TEC can theoretically achieve conversion efficiencies above 45% when operating between thermal reservoirs at 1150 K and 550 K, but previous single-stage devices have been limited to thermal efficiencies below 20%. Poor thermal management of the Na-TEC (*i.e.*, thermal parasitic loss of heat that is not utilized in the conversion to electricity) prevents the realization of higher thermal efficiencies. To reduce parasitic thermal losses, the energy conversion step of the Na-TEC can be divided into two stages. The addition of a second stage for energy conversion improves the thermal management of the Na-TEC due to the lower average temperature of the device. No other group has previously considered dividing the isothermal expansion step into multiple stages.

2) This thesis also considers the use of a non-wetting porous structure that can enable low-temperature capillary pumping solutions in the Na-TEC condenser to mitigate against such issues. Capillary structures in Na-TECs have been exclusively developed to operate in the high-temperature evaporator where the driving force for liquid sodium transport is generated. However at high temperatures, sodium corrosion facilitates the dissolution of alloying elements in the containment materials (most notably nickel, very common in high temperature alloys), initiates the formation of intermetallic compounds, and leads to the embrittlement of metallic enclosures. [63, 64] In the long-term, these degradation mechanisms will reduce the pumping pressure head of the capillary structure and diminish the overall performance of the Na-TEC.

The following thesis questions are answered:

i. What are the thermodynamic operating limits for a dual-stage Na-TEC?

In Chapter 2, the fundamental electrochemical, thermodynamic, and transport properties of the single-stage Na-TEC are discussed in detail. For a dual-stage Na-TEC, the isothermal expansion can be divided into two stages; one at the evaporator temperature (1150 K) and another at an intermediate temperature (550 K - 1050 K). The dual-stage Na-TEC takes advantage of regeneration and reheating, and is amenable to improved thermal management through a reduction of the average temperature of the device. The addition of a second stage reduces the thermal parasitic losses, leading to higher practical efficiencies. To determine the optimal thermodynamic operating conditions, the expressions for power and efficiency are derived for the dual-stage Na-TEC. Using knowledge about the electrochemical processes in a single-stage Na-TEC coupled with previous experimental

data, the expected thermal efficiency and maximum power of a dual-stage device are determined. Furthermore, a thermodynamic regime map in terms of the power density and the total parasitic loss is established to inform the preferred application domains of the single- and dual-stage Na-TEC's.

ii. To what degree can a reduced-order model be used to effectively design a dual stage Na-TEC to operate at the maximum practical efficiency?

The thermal management of the dual-stage Na-TEC is the critical challenge in achieving high thermal efficiencies. Chapter 3 introduces a detailed thermal analysis, using a reduced-order finite-element model, to estimate the thermal parasitic losses of a dual-stage Na-TEC design. First, a high-level design with axisymmetric geometry, including sizes and material selection, is presented. Using a thermal circuit, only conduction losses are initially considered to establish an upper limit for the power and efficiency. A simplified analytical model is also developed to estimate thermal conduction through the liquid-return path between the evaporator and condenser. Radiation is then considered in the interior and exterior of the device in the limit of surface-to-surface exchange. To further reduce computational time, equivalent emissivities are used to express the effect of complex geometries having multiple radiating surfaces. Finally, an iterative method between the finite-element model and the thermodynamic model is used to estimate the power and efficiency of this design while accounting for parasitic losses from these various mechanisms. A cost analysis for this dual-stage Na-TEC design, based on the reduced-order model, is also presented.

iii. What temperature-dependent interfacial pressures can be generated between a stainless-steel porous structure and liquid sodium?

To develop a low-temperature capillary pump, it is necessary to measure the maximum interfacial pressure between a porous structure and liquid sodium. Liquid sodium will not immediately penetrate a non-wetting capillary ($\theta_{ca} > 90°$) because the solid-surface adhesion forces will repel the liquid to minimize contact within the capillary.[65] The term "breakthrough pressure" refers to the pressure needed to cause a fluid to penetrate a non-wetting capillary. Liquid sodium is non-wetting to stainless steel in the relevant range of Na-TEC condenser temperatures (200 °C - 400 °C), so it is the chosen material for the porous structure. In Chapter 4, an experiment designed to measure the temperature dependent breakthrough pressure of liquid sodium on a stainless steel porous sample is presented. This experiment requires an incremental pressurization of sodium until it penetrates through the porous sample. The breakthrough pressure is measured by electrodes placed downstream. These detect the flowing sodium after breakthrough when it completes an electric circuit, and they are also used to measure the flow velocity. Results for the temperature dependent breakthrough pressure are discussed, and these results are compared with breakthrough pressure models for several geometries to provide insight. The permeability of the porous structure is determined using the velocity data, and this result is also compared to permeability models for different geometries.

iv. To what degree (pressure head and discharge rate) can passive liquid-sodium pumping be maintained through the condensation of sodium vapor within a non-wetting porous structure?

A unique sodium capillary pump is described in Chapter 5 to enable low-temperature capillary pumping solutions in the Na-TEC. This pump operates by allowing low-pressure sodium vapor to condense within a non-wetting ($\theta_{ca} > 90^{o}$) porous structure; the liquid adjacent to this condensation interface is at a higher pressure than the vapor due to the interface curvature. A net force acts upon the liquid sodium at the solid-liquid-vapor interface, effectively "pushing" it towards the higher pressure bulk liquid region. This in in contrast to traditional wicks, where the liquid is "pulled" against a pressure gradient by the solid surface adhesion force. An experiment is designed to demonstrate the feasibility of this pumping mechanism by measuring the mass flowrate of liquid sodium and the total pressure head. The operation of this pumping experiment is guided by a conjugate heat transfer model which considers the coupled momentum and thermal transport processes within the non-wetting porous structure as sodium vapor is condensed. The results from two experiments are discussed in detail, both of which demonstrate evidence of liquid sodium pumping.

CHAPTER 2. THERMODYNAMIC LIMITS OF A DUAL−STAGE NA-TEC

The thermal efficiency of the single-stage Na-TEC is limited by large thermal parasitic heat losses. A dual-stage Na-TEC can potentially operate with a higher practical thermal efficiency by taking advantage of regeneration and reheat steps, and by improving the overall thermal management of the device through a reduction of the average device temperature. The separation of the isothermal expansion into multiple stages is a novel idea that has not been previously studied by other research groups. This chapter begins by introducing a detailed electrochemical model and a thermal efficiency framework for the single-stage Na-TEC in Section 2.1 and Section 2.2, respectively. In Section 2.3, a thermodynamic argument for pursuing the staging of the isothermal expansion process in the Na-TEC is presented. Section 2.4 describes the key electrochemical, thermodynamic, and transport mechanisms in a dual-stage Na-TEC. A detailed comparison between the single- and dual-stage devices is conducted in Section 2.5. Finally, Section 2.6 summarizes the key findings in this chapter, with the aim of answering the thesis question: *What are the thermodynamic operating limits for a dual-stage Na-TEC?*

2.1 Electrochemical Parameters of a Single-Stage Na-TEC

2.1.1 Single-Stage Na-TEC Voltage

The voltage produced by the Na-TEC originates from the oxidation of sodium vapor and the reduction of sodium ions at different pressures, similar to a concentration cell. The open-circuit voltage V_{oc} is determined by the Nernst equation, where the equilibrium constant is approximated by a pressure ratio (Equation 2.1). Here, the subscript *oc* refers to a property measured at open-circuit, and the subscripts *a* and *c* refer to

properties measured at the electrode/electrolyte interfaces of the anode and cathode, respectively. As current is drawn, the total voltage V (Equation 2.2) is the open-circuit voltage reduced by the combined kinetic and mass transfer polarizations ξ (*i.e.*, overpotential) and by the Ohmic potential drop across the electrolyte, computed using the Thevenin equivalent area-specific Ohmic resistance r_{Th} (*i.e.*, ionic resistance of the electrolyte, sheet resistance and contact resistance in the electrodes, Ω cm^2). Both the current density j and the area-specific resistance r_{Th} are normalized to the (planar) surface area of the electrolyte. The overpotential is calculated using a modified Butler-Volmer equation (Equation 2.3) which incorporates both the kinetic and mass transfer polarizations, with a transfer coefficient of ½.[66] The ionic resistivity of the β''-alumina ($1/\sigma_\beta$) dominates the Ohmic potential drop and it is a function of the crystalline structure, the doping concentration of additives such as MgO or Li_2O, and the operating temperature.[3] The presence of MgO is critical because without it, oxygen anions (O^{2-}) begin to populate interstitial positions in the β''-alumina conduction plane and reduce the mobility of the sodium cations.[67] The high ionic conductivity of this electrolyte, which makes it suitable for the Na-TEC, is a result of the Frenkel transport mechanism, by which sodium cations in the conduction plane shift to vacancy positions left after stable ions transfer to interstitial positions.[68] The model developed by Steinbruck *et al.* (Equation 2.4) is widely used to estimate the temperature-dependent ionic conductivity of β''-alumina.[69]

$$V_{oc} = V_{c,oc} - V_{a,oc} \approx \frac{\bar{R}T_{evap}}{F} ln \frac{P_{a,oc}}{P_{c,oc}} \tag{2.1}$$

$$V = V_{oc} + \left(\xi_c - \xi_a\right) - j r_{Th} \tag{2.2}$$

$$j_i = j_{0,i}\left(e^{-\left(\frac{1}{2}\right)\frac{F}{\bar{R}T_{evap}}\xi_i} - \frac{P_i}{P_{oc,i}} e^{\left(\frac{1}{2}\right)\frac{F}{\bar{R}T_{evap}}\xi_i} \right) \tag{2.3}$$

$$\sigma_\beta = \left[\left(1.62\times10^{-5}\right) T\, exp\left(\frac{-45.5}{T}\right) + \left(1.55\times10^{-7}\right) T\, exp\left(\frac{3722}{T}\right) \right]^{-1} \tag{2.4}$$

The subscript *i* in Equation 2.3 refers to both anode (*a*) and cathode (*c*), where $j_c = -j_a$ when charge conservation is applied. The exchange current density j_0 is a function temperature, sodium pressure, and the material of the electrode as well as its catalytic activity.[66] Due to the faster kinetics of sodium oxidation relative to its reduction within this device (*i.e.*, $j_{0,a} >> j_{0,c}$), the anode overpotential magnitude is significantly smaller than the cathode overpotential magnitude (*i.e.*, $|\xi_c| >> |\xi_a|$).[70] The exchange current density j_0 (Equation 2.5) is defined as a function of the temperature-independent exchange current density *B*; this variable has been tabulated for several electrode materials.[20, 71] Higher values of *B* correspond to more facile kinetics at the electrode/electrolyte interface. In the limit of $B \rightarrow \infty$, there is no resistance to the charge transfer kinetics at the electrode/electrolyte interface and only the mass transfer resistance (*i.e.*, sum of all pressure drops within the Na-TEC) contributes to the overpotential.

$$j_{0,i} = B\sqrt{\frac{p_{oc,i}\, p_{sat}(T)}{T}} \tag{2.5}$$

2.1.2 Sodium Pressure within the Single-Stage Na-TEC

At low pressures, the transport of sodium from the electrode/electrolyte interface to the bulk plenum is governed by molecular effusion through the small pores of the electrodes. In the cathode, the transport occurs in the free molecular flow regime (Knudsen

number $Kn \geq 10$) due to the long mean free path of sodium at the saturation pressure of typical condenser temperatures $P_{sat}(T_{cond})$.[70] The sodium vapor saturation pressure $P_{sat}(T)$ is calculated using an empirical Antoine relation.[72] For gas flowing on either side of a porous structure in this range of Kn , the rate at which sodium molecules enter and exit the pores is proportional to $P/\sqrt{T}$, a phenomenon called thermal transpiration.[73] At open circuit, the net mass transfer between the cathode/electrolyte interface and the condenser is zero, so the open-circuit pressure P_{oc} at the cathode/electrolyte interface is given by Equation 2.6. In the anode, the mean free path is much shorter than the pore dimension, so at open-circuit the pressure at the anode/electrolyte interface is equivalent to the saturation pressure at the evaporator temperature $P_{a,oc} = P_{sat}(T_{evap})$.[11]

$$\frac{P_{c,oc}}{\sqrt{T_{evap}}} = \frac{P_{sat}\left(T_{cond}\right)}{\sqrt{T_{cond}}} \Rightarrow P_{c,oc} = P_{sat}\left(T_{cond}\right)\sqrt{\frac{T_{evap}}{T_{cond}}} \tag{2.6}$$

In a closed circuit, the pressure at the electrode/electrolyte interface P_i (see Equation 2.3) is a function of the current density. In the free molecular flow regime ($Kn \geq 10$), the pressure drop for flowing sodium is determined using gas kinetic theory. In the cathode, the pressure drop as sodium exits the electrode/electrolyte interface is described by Equation 2.7, assuming an accommodation coefficient of one.[44] Likewise, there is a pressure drop as sodium crosses the gas-liquid interface in the condenser (Equation 2.8).

$$\Delta P = \frac{j}{\varphi F}\sqrt{2\pi \bar{R} M T_{evap}} \tag{2.7}$$

$$\Delta P = \frac{j}{F}\sqrt{2\pi \bar{R} M T_{cond}} \tag{2.8}$$

The pores in the electrode can be modeled as cylindrical channels with an average pore diameter d_p. The pressure drop ΔP_K for a rarefied gas transporting through a porous electrode at temperature T_{evap} is given by Equation 2.9 for a tube with a small aspect ratio ($L_e/d_p < \approx 1$), where R_K is the mass transfer resistance for Knudsen flow.[73] This equation is determined by finding the ratio of molecules that flow all the way through the channel to the total number molecules that enter the channel boundary. The dimensionless morphology factor G is typically employed as an empirical variable for modeling purposes, and it is a function of the thickness, porosity φ, and pore diameter of the electrode.[18] In the anode side of the device, the sodium vapor is at a much higher pressure and the flow occurs in the continuum regime ($Kn \rightarrow 0$). The pressure drop through a cylindrical pore is determined using the Hagen-Poiseuille law (Equation 2.10), where R_v is the mass transfer resistance for viscous flow, $\mu(T)$ is the temperature dependent sodium vapor viscosity, and $\rho(T)$ is the temperature dependent sodium vapor density. Calculating the pressure drop in the anode is necessary even though it is negligible compared to the cathode side pressure drop due to the significant difference in absolute pressures (4-6 orders of magnitude). It is especially needed to determine the limiting current (see Section 2.1.3).

$$\Delta P_K = \frac{3G}{8\pi}\frac{j}{F}\sqrt{2\pi\bar{R}MT_{evap}} = R_K\left(\frac{jM}{\varphi F}\right) \quad \rightarrow \quad G = \frac{8\pi}{3\varphi}\left(1+\frac{L_e}{d_p}\right) \tag{2.9}$$

$$\Delta P_v = \frac{32\mu L}{d_p^2\rho\varphi}\left(\frac{jM}{F}\right) = R_v\left(\frac{jM}{\varphi F}\right) \tag{2.10}$$

The dusty gas model is typically used to describe transport between the two extremes of continuum flow (Kn $\rightarrow$ 0) and free molecular flow ($Kn \geq 10$). The pressure drop in this transitional (or slip) regime ΔP_{slip} is related to the mass flux through a single cylindrical pore $jM/F/\varphi$ using an equivalent mass transfer resistance. According to the dusty gas

model, viscous flow occurs in parallel to Knudsen flow, so the mass transfer resistance is approximated by adding the viscous and Knudsen flow resistances in parallel (Equation 2.11).[74] In the limit as $Kn \rightarrow 0$, this equation becomes the Hagen-Poiseuille law (Equation 2.10) while in the limit as $Kn \rightarrow \infty$, it approaches ΔP_K (see Figure 2.1a). Therefore, Equation 2.11 can be used to approximate the flow in either regime, and it applies for flow in both the anode and the cathode. The pressures at the electrode/electrolyte interfaces P_i are found by summing all the appropriate terms (Equation 2.12, Equation 2.13), including ΣP_{loss} which accounts for pressure losses from other components within the Na-TEC. These additional pressure losses only have an appreciable effect on the low-pressure cathode side.

$$\Delta P_{slip} = \left(\frac{R_v R_K}{R_v + R_K} \right) \left(\frac{jM}{\varphi F} \right) \quad \begin{cases} \lim_{Kn \to 0} \Delta P_{slip} = \dfrac{32 \mu L_e}{d_p^2 \rho \varphi} \left(\dfrac{jM}{F} \right) \\ \lim_{Kn \to \infty} \Delta P_{slip} = \dfrac{3G}{8\pi} \dfrac{j}{F} \sqrt{2\pi \bar{R} M T_{evap}} \end{cases} \tag{2.11}$$

$$P_a = P_{a,oc} - \Delta P_{slip} \left(\rho \left(T_{evap} \right), \mu \left(T_{evap} \right) \right) \tag{2.12}$$

$$P_c = P_{c,oc} + \Delta P_{slip} \left(\rho \left(T_{cond} \right), \mu \left(T_{cond} \right) \right) + \frac{j}{\varphi F} \sqrt{2\pi \bar{R} M T_{evap}} + \frac{j}{F} \sqrt{2\pi \bar{R} M T_{cond}} + \sum P_{loss} \tag{2.13}$$

2.1.3 Single Stage Na-TEC Limiting Current and Maximum Power Density

With detailed knowledge of the pressures at the electrode/electrolyte interfaces, the limiting current can be obtained. The mass transfer limit occurs when kinetic losses are negligible (*i.e.* $B \rightarrow \infty$). When Ohmic losses are also neglected, the mass transfer limited voltage in the single-stage Na-TEC is given by Equation 2.14. The limiting current represents the maximum reaction rate of the system, such that no further change in the

voltage can increase the current.[66] Thus, the limiting current is mathematically found in the limit where $V \rightarrow -\infty$ (*i.e.*, an infinite negative bias does not yield a further increase in the current). In Equation 2.14, this occurs if the denominator (cathode pressure) goes to infinity or if the numerator (anode pressure) goes to zero. Only the latter case is physically significant, so the limiting current is given by Equation 2.15.[75] Calculations show that the limiting current density is much larger than the short-circuit current density (*i.e.*, $j_{lim}/j_{sc} >> 1$, see Figure 2.1b), implying that the cycle is not mass transfer limited in the anode. Rather the cathode charge transfer, the Ohmic losses, and the cathodic mass transfer all significantly affect the power density.[20]

$$\lim_{B\to\infty} V = \frac{\bar{R}T_{evap}}{F} ln\left(\frac{P_{a,oc} - \Delta P_{slip}\left(\rho\left(T_{evap}\right), \mu\left(T_{evap}\right)\right)}{P_{c,oc} + \left(\frac{1}{\varphi} + \frac{3G}{8\pi}\right)\frac{j}{F}\sqrt{2\pi\bar{R}MT_{evap}} + \frac{j}{F}\sqrt{2\pi\bar{R}MT_{cond}}}\right) \qquad (2.14)$$

$$P_{a2,oc} = \Delta P_{slip}\left(\rho\left(T_{evap}\right), \mu\left(T_{evap}\right), j_{lim}\right) \quad \rightarrow \quad j_{lim} \approx \frac{d_p^2 \rho \varphi}{32\mu L_e}\left(\frac{F}{M}\right) P_{a,oc} \qquad (2.15)$$

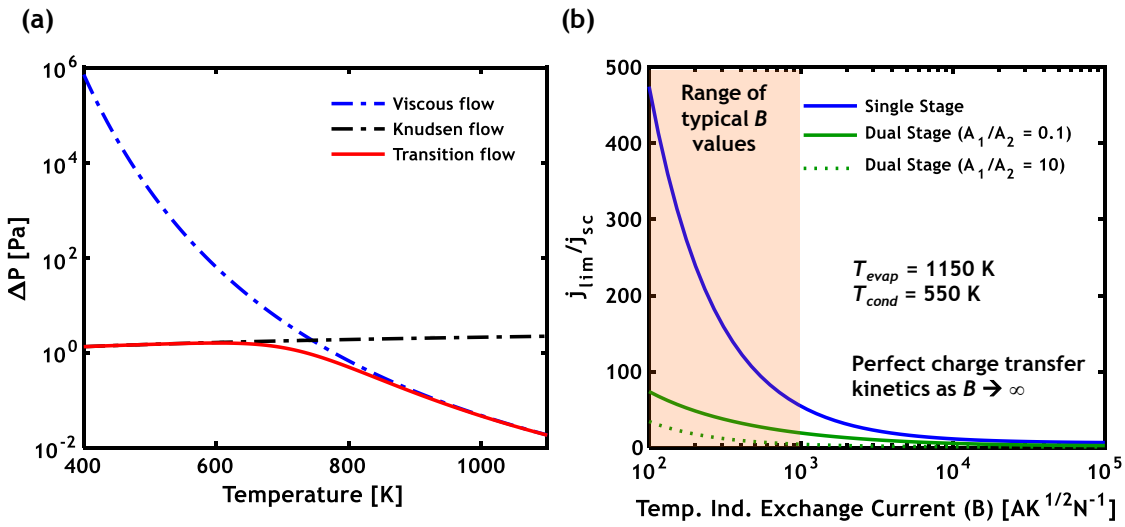

Figure 2.1 (a) Plot of the sodium vapor flow pressure drop in the transitional regime vs. temperature (L_e = 1 μm, φ = 90%, G = 10, j = 0.5 A cm^{-2}). In the limit of $Kn \rightarrow 0$, the vapor transport is described with a viscous flow model whereas in the limit of $Kn \rightarrow \infty$, the vapor transport is described with a Knudsen flow model. (b) Ratio of the limiting current and the short circuit current vs. the temperature independent exchange current (B). In general, B < 1000 A K$^{1/2}$ N^{-1}for most materials that have been previously studied.

The power density ($jV = j^2 r_{load}$) is a function of the current density and the area-specific external load resistance r_{load}, which is normalized to the total electrolyte area (*e.g.*, $r_{load} = A \cdot R_{load}$). To find the maximum power, the power density is differentiated implicitly with respect to r_{load}. This operation yields the load-matching condition (Equation 2.16), where r_{ct} is the charge transfer resistance. The charge transfer resistance is experimentally measured by taking the difference between the high and low-frequency real-axis intercepts of a Nyquist plot from an electrochemical impedance spectroscopy (EIS) measurement.[76] This load-matching condition is non-linear with the current density but can be solved numerically to yield the maximum power.

$$r_{load} = r_{Th} + \left(r_{ct,c} - r_{ct,a} \right) \quad \rightarrow \quad r_{ct,i} = -\frac{\partial \xi_i}{\partial j} \tag{2.16}$$

Figure 2.2 shows the maximum power as a function of the condenser temperature. As the condenser temperature decreases, the cathode pressure reduces and the open-circuit voltage increases. This higher open-circuit voltage is counterbalanced by an increase in the total overpotential at lower temperatures. Thus, the maximum power density saturates at low condenser temperatures, exhibiting nearly constant power within a large range of condenser temperatures. Indeed, there is only a 1.5% difference in the maximum power between the coldest possible condenser temperature where sodium solidifies ($T \approx 370$ K) and 575 K in Figure 2.2.

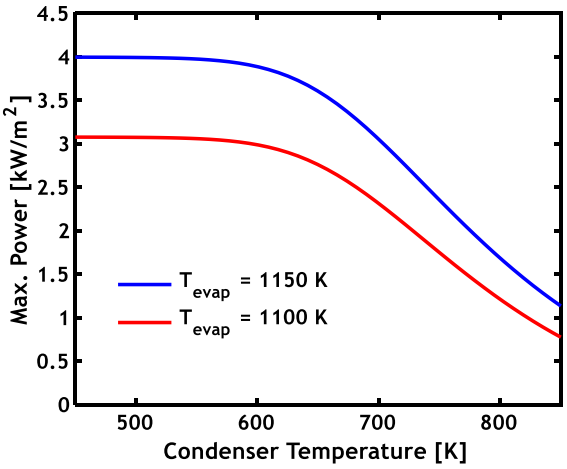

Figure 2.2 Maximum power of a single-stage Na-TEC as a function of condenser temperature (B = 120 A K$^{1/2}$ N^{-1}, G = 50, r_{Th} = 0.25 Ω cm^2).

2.2 Thermal Efficiency of a Single-Stage Na-TEC

The thermal efficiency is the ratio of the power output to the heat input (Equation 2.17), where $\dot{Q}''_{loss}$ is the thermal parasitic loss (normalized to the electrolyte area). The thermal parasitic loss (hereafter referred to as parasitic loss) is the combination of (i) heat input that does not participate in power production but simply bypasses the thermo-electrochemical process and is transferred to the condenser, and (ii) heat that is lost from the device directly to the surroundings due to poor insulation. To analyze the ideal

thermodynamic cycle (*i.e.*, no internal irreversibilities), the heat lost to the surroundings is assumed to be zero (*i.e.*, perfect insulation) so only heat that bypasses the thermo-electrochemical process is considered in the parasitic loss term. This energy loss manifests as conduction heat transfer through the walls and the capillary wick of the device plus radiative heat transfer from the cathode to the condenser.[46] From energy conservation for the cycle, the heat input (see Equation 2.17) is the sum of the heat outputs (*i.e.*, sensible cooling, the latent heat of vaporization, and parasitic loss) and the power generated. The parasitic loss is affected by the operating conditions (namely T_{evap}, T_{cond}, j), the materials, the geometry, and the surroundings.[70] For parametric calculations, the parasitic loss fraction $f = \dot{Q}''_{loss}/\dot{Q}''_{in}$ is used, which is defined as the ratio of parasitic loss (*i.e.*, heat not used for power generation) to the total heat input (Equation 2.18). Both terms are normalized to the electrolyte area. The efficiency is then recast as Equation 2.19.

$$\eta = \frac{jV}{\dot{Q}''_{in}} = \frac{jV}{jV + \frac{jM}{F}\left(h_{fg}\left(T_{cond}\right) + \int_{T_{cond}}^{T_{evap}} c_p(T)dT \right) + \dot{Q}''_{loss}} \tag{2.17}$$

$$\begin{aligned} f = \frac{\dot{Q}''_{loss}}{\dot{Q}''_{in}} &= \frac{\dot{Q}''_{loss}}{jV + \frac{jM}{F}\left(h_{fg}\left(T_{cond}\right) + \int_{T_{cond}}^{T_{evap}} c_p(T)dT \right) + \dot{Q}''_{loss}} \\ \Rightarrow \dot{Q}''_{loss} &= \left(jV + \frac{jM}{F}\left(h_{fg}\left(T_{cond}\right) + \int_{T_{cond}}^{T_{evap}} c_p(T)dT \right) \right)\left(f \Big/ (1-f) \right) \end{aligned} \tag{2.18}$$

$$\eta = \frac{jV}{\left(1+\frac{f}{(1-f)}\right)\left(jV+\frac{jM}{F}\left(h_{fg}(T_{cond})+\int_{T_{cond}}^{T_{evap}} c_p(T)dT\right)\right)} = \frac{V(1-f)}{V+\frac{M}{F}\left(h_{fg}(T_{cond})+\int_{T_{cond}}^{T_{evap}} c_p(T)dT\right)} \quad (2.19)$$

Figure 2.3 shows the cumulative effect on the efficiency from each voltage drop mechanism as the Na-TEC generates power. The efficiency and power in a single-stage Na-TEC depend on the seven variables listed in Table 2.1. The values used for each of these variables are listed in the figure captions, and are taken from previous experimental data by assuming the use of a 500 μm thick electrolyte with TiN electrodes (L_e = 32.5 μm, φ = 90%). [29, 58, 70] The top line in Figure 2.3 indicates the open-circuit limit of the efficiency. For a closed circuit, the maximum efficiency (dashed black line) occurs when the kinetic polarization does not affect the overpotential (*i.e.*, when $B \rightarrow \infty$ in Equation 2.3). The efficiency is not significantly affected when the charge transfer kinetics are included (< 9% drop in efficiency at maximum power); this implies that there are minimal benefits to increase B beyond $\approx$ 500 A $K^{1/2}$ N^{-1} at these operating conditions.[77] In contrast, the Ohmic losses significantly decrease the efficiency, particularly when operating close to the maximum power density. For the single-stage Na-TEC, the major drop in efficiency results from the large parasitic loss (gold line).[11]

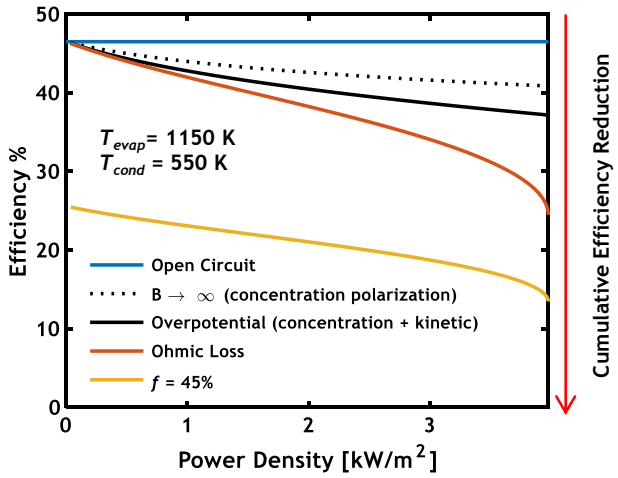

Figure 2.3 Efficiency vs. power density of the single-stage Na-TEC (T_{evap} = 1150 K, T_{cond} = 550 K, B = 120 A $K^{1/2}$ N^{-1}, G = 50, r_{Th} = 0.25 Ω cm^2). Each curve shows the cumulative effect on the efficiency as each voltage drop mechanism is subtracted from the open-circuit voltage.

Table 2.1 Single-Stage Na-TEC Parameters

Thermodynamic	T_{evap}	Evaporator Temperature [K]
	T_{cond}	Condenser Temperature [K]
Independent	j	Current Density [A cm^{-2}]
Electrochemical	r_{Th}	Thevenin Equivalent Resistance [Ω cm^2]
	G	Morphology Factor
	B	Temp. Indep. Exchange Current Density [A $K^{1/2}$ N^{-1}]
Heat Transfer	f	Parasitic Heat Loss Fraction [%]

In Figure 2.3, the parasitic loss fraction is treated as a constant (f = 45%). In a real device however, f decreases as current density increases. To illustrate this, a simple heat transfer model for the single-stage Na-TEC is employed. Losses directly to the surroundings are neglected in this heat transfer model, so the parasitic loss term only

encompasses the heat that bypasses the conversion process and is transferred directly to the condenser. This parasitic heat loss is comprised of radiation from the cathode at T_{evap} and conduction originating from the evaporator (Equation 2.20) where β_1, β_2 are fitting parameters used to approximate previous experimental data. Using $\beta_1 = 1.6 \cdot 10^{-6}$ and $\beta_2 = 1.9 \cdot 10^{-4}$, this simple model can predict results from prior modeling efforts, showing a maximum efficiency of 19%.[47] The radiative term can be linearized (Equation 2.21) so that the heat loss is proportional to ΔT, with an equivalent thermal resistance R_{eq}.

$$Q''_{loss} = \beta_1 \sigma \left(T_{evap}^4 - T_{cond}^4 \right) + \beta_2 \left(T_{evap} - T_{cond} \right) \tag{2.20}$$

$$\dot{Q}''_{loss} = \left(T_{evap} - T_{cond} \right) / R_{eq} \tag{2.21}$$

An example of the normalized power density, the normalized efficiency, and f as a function of current density using this simple heat transfer model is shown in Figure 2.4. At open-circuit, f =1 because all the heat entering the Na-TEC is lost without any power generation. Alternatively, f is minimized at some higher current density closer to the maximum power. As is the case with all TRES, the locations of maximum efficiency and maximum power do not coincide. In the case where parasitic losses are a small component of the heat output, this difference exists because the maximum efficiency occurs at lower current densities where current-dependent overpotential and Ohmic losses are smaller, whereas maximum power results from a trade-off between the voltage produced and the current drawn. Typical (single-stage) Na-TECs operate with $f \geq 45\%$ at their peak efficiencies (≈30-35% of the Carnot efficiency limit) according to various studies.[58, 78] This parasitic loss fraction is found by fitting Equation 2.18 to experimental data from previous devices. The lowest efficiencies occur when functioning close to open-circuit (where $f \rightarrow 1$) or near the short-circuit current (where $V \rightarrow 0$), although previous applications have not operated in these regimes.

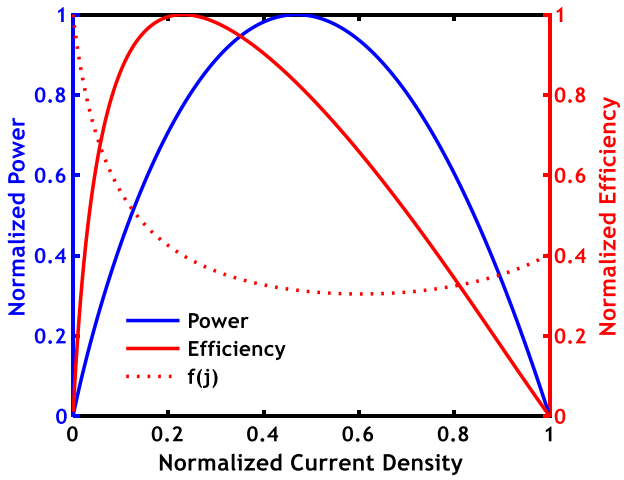

Figure 2.4 Simulated power and efficiency curves vs. current density (each normalized to the maximum value) using the simple heat transfer model (Equation 2.20). The dashed red curve is the thermal parasitic loss fraction f. (T_{evap} = 1150 K, T_{cond} = 550 K, B = 120 A $K^{1/2}$ N^{-1}, G = 50, r_{Th} = 0.25 Ω cm^2).

2.3 Thermodynamic Staging of the Na-TEC

To improve the efficiency of the Na-TEC, the isothermal expansion step of the cycle can be separated into two stages, one at the evaporator temperature and another at an intermediate temperature. This increase in efficiency is demonstrated with the following thermodynamic argument. First, consider N heat engines interacting between two thermal reservoirs and exchanging heat with one another as depicted in Figure 2.5a. Next, assume there are N-1 regenerators between the heat engines that regenerate the rejected heat, each having some variable regenerator efficiency η_{reg}. The total efficiency of these N engines, with N-1 regenerators in-between them, interacting between two fixed-temperature thermal reservoirs is given by Equation 2.22.[79] This expression is derived by finding the ratio of total work to heat input $(W_{e,1} + W_{e,2} + \ldots + W_{e,N})/(\eta_1 / W_{e,1})$ for a small number of engines (*e.g.*, $N \leq 4$) until the recursive pattern is recognized. In the limit that each regenerator operates with η_{reg} = 100%, the total efficiency simplifies to Equation 2.23.

$$\eta_N = \eta_1 + \sum_{i=1}^{N-1}\left[\left(\eta_{i+1}\right)\prod_{j=1}^{i}\left[\eta_{reg,j}\left(1-\eta_j\right)\right]\right] \tag{2.22}$$

$$\eta_N = 1-\prod_{i=1}^{N}\left(1-\eta_i\right) \tag{2.23}$$

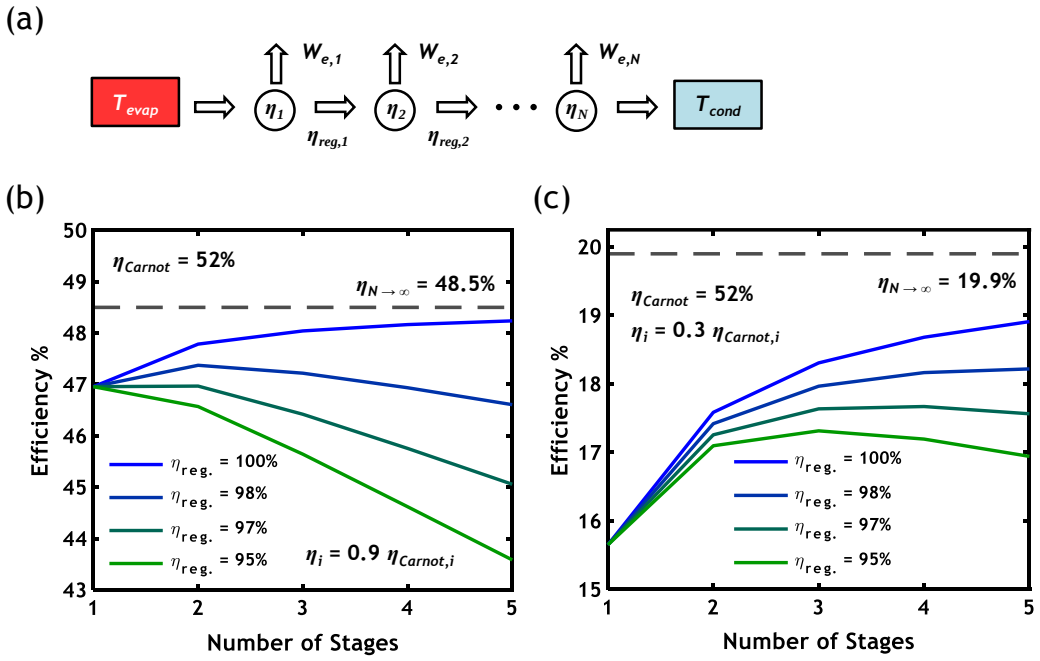

Figure 2.5 Schematic showing *N* heat engines interacting between two thermal reservoirs with regeneration efficiencies $\eta_{reg,i}$ of the heat output from the first *N*-1 engines, each producing power $W_{e,i}$. (b) Efficiency of a multi-stage Na-TEC with T_{evap} = 1150 K, T_{cond} = 550 K as a function of the number of stages and the regeneration efficiency (each individual stage is assumed to operate at 90% of its respective ideal Carnot efficiency for a given temperature drop across a given stage). (c) Same as (b) but with each individual stage assumed to operate at 30% of its respective ideal Carnot efficiency for a given temperature drop across a stage.

Using this framework, each engine can be assumed to be a single-stage Na-TEC with 90% of the Carnot efficiency.[9] When the conversion step in the Na-TEC is divided into multiple stages, each individual stage can be modeled as a single-stage Na-TEC. Using Equation 2.22, the total efficiency of a multi-stage Na-TEC operating between fixed

temperature reservoirs can be found for any number of stages. In Figure 2.5b, for η_{reg} = 100%, the overall efficiency is a monotonically increasing function of the number of stages. For 97% < η_{reg} < 98%, the optimum number of stages is two and for η_{reg} < 95%, it is preferable to operate with a single-stage Na-TEC. Based on Figure 2.5b, a point of diminishing returns exists at two stages using an asymptotic extrapolation for η_{reg} = 100%. This suggests that the improvements in efficiency after two stages may not be worth the added engineering complexity. Even if each stage operated at 30% of the Carnot efficiency (corresponding to efficiencies demonstrated in practice for single-stage devices), two stages would still be an adequate compromise between efficiency and engineering complexity (Figure 2.5c). It must be noted that this model does not account for the possibility for reheating after each stage. Nevertheless, it is useful for illustrating the effect of additional stages on the total efficiency.

2.4 Operation and Electrochemical Parameters of a Dual-Stage Na-TEC

2.4.1 Dual-Stage Na-TEC Operation

To improve the efficiency of the Na-TEC, the isothermal expansion step of the cycle is separated into two stages: one at T_{evap} and another at an intermediate temperature T_{int}. The operation of a dual-stage Na-TEC is depicted schematically in Figure 2.6a. Liquid sodium is isobarically heated (1)-(2) and vaporized (2)-(3) in the evaporator. Sodium cations then expand isothermally from the evaporator into an intermediate plenum (3)-(4), where the bulk pressure within this plenum is the sodium saturation pressure at an intermediate temperature (T_{int}). As the sodium vapor cools isobarically, the heat is 100% regenerated in the second-stage electrolyte (4)-(5) because heat loss to the surroundings for the ideal thermodynamic cycle is neglected (*i.e.*, perfect insulation, the heat cannot escape anywhere else). The sodium then undergoes a second isothermal expansion occurring at T_{int} from the intermediate plenum to the condenser (5)-(6), where reheat can be supplied.

The low pressure sodium vapor then cools (6)-(7) and condenses (7)-(8). Finally, the liquid sodium is isentropically pumped back to the evaporator (8)-(1). The ideal dual-stage thermodynamic cycle in temperature-entropy (T-S) coordinates is depicted in Figure 2.6b. This figure shows how the Na-TEC can take advantage of reheat and regeneration steps when two stages are implemented. The expansion in the second-stage can be partially driven by regenerating the sensible isobaric heat transfer after the first-stage expansion. Reheat can then be introduced to extend the isothermal expansion in the second stage, which can be supplied from the same reservoir supplying heat to the evaporator. The separation of the isothermal expansion process of the Na-TEC into two stages is a novel concept that has not been previously considered by other research groups.

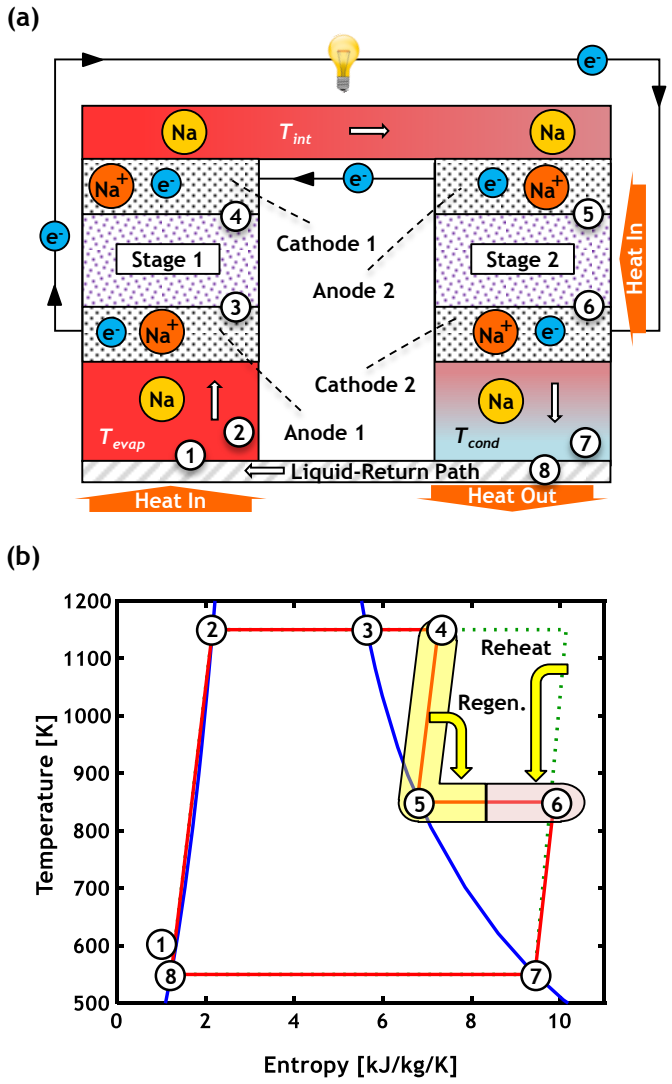

Figure 2.6 (a) Schematic illustration of a dual-stage Na-TEC. (b) Temperature-Entropy (T-S) diagram of the ideal dual-stage Na-TEC thermodynamic cycle (red lines) overlaid on top of the sodium saturation curves (blue lines), where each number corresponds to a state of the system. A single-stage Na-TEC cycle (green dotted lines) operating with the same temperatures as the dual-stage cycle is plotted underneath. The yellow and pink highlighted regions show the regeneration and reheat steps.

2.4.2 Dual-Stage Na-TEC Voltage

The total voltage generated by the dual-stage Na-TEC is the sum of the open-circuit voltage of both stages (*i.e.*, connected electrically in series) reduced by the electrode overpotentials and the Ohmic contributions from each stage (Equation 2.24). The index *i*

=1, 2 corresponds to properties of the first- and second-stage respectively. The current density and the area-specific resistance of each stage are normalized to the (planar) surface area of each stage's β''-alumina electrolyte (A_1, A_2). The total current is then conserved through the circuit if the two stages are connected electrically in series ($j_1 A_1 = j_2 A_2$). The overpotential is a function of the temperature and the current density in each stage. As with the single-stage Na-TEC, the first-stage anode overpotential is negligible because of the faster charge transfer kinetics at high temperatures. The anode overpotential of the second-stage, however, cannot be neglected because it is of the same order of magnitude as the cathode overpotentials of each stage (*i.e.*, $|\xi_{c,1}|$, $|\xi_{a,2}|$, $|\xi_{c,2}| >> |\xi_{a,1}|$).

$$V = \sum_{i=1}^{2} \left[V_{oc,i} + \left(\xi_{c,i} - \xi_{a,i} \right) - j_i r_{Th,i} \right] \tag{2.24}$$

2.4.3 Sodium Pressure within the Dual-Stage Na-TEC

The pressures in the four electrode/electrolyte interfaces in the dual-stage Na-TEC are found by employing the same methods used for the single-stage Na-TEC. The bulk pressure in the intermediate plenum is assumed to be the saturation pressure at the intermediate temperature T_{int}. At open circuit, the pressure in the first-stage anode follows the same form as in the single-stage Na-TEC anode, $P_{a1,oc} = P_{sat}(T_{evap})$. In the first-stage cathode, the pressure depends on the mean free path of the sodium vapor in the intermediate plenum. Using 10 μm for the characteristic pore diameter in the electrode, $0.1 \leq Kn \leq 10$ for temperatures $\approx$710 K < T < $\approx$1000 K. In many applications T_{int} will be within this range, but for several other applications T_{int} > 1000 K and the vapor will exist in the continuum regime. For uniformity, the open-circuit pressure in the intermediate plenum is simply set to the bulk pressure, even though the vapor is not technically within the continuum regime. Thus, the first-stage cathode open-circuit pressure is $P_{c1,oc} = P_{sat}(T_{int})$ and the second-stage anode open-circuit pressure is $P_{a2,oc} = P_{sat}(T_{int})$. Finally, the second-stage cathode operates

in the free-molecular flow regime, so the open-circuit pressure is $P_{c2,oc} = P_{sat}(T_{cond})\sqrt{T_{int}/T_{cond}}$, similar to Equation 2.6. In a closed circuit, the pressures at the electrode/electrolyte interfaces are affected by the same physical mechanisms as in the single-stage Na-TEC. Therefore, these pressures are given by Equation 2.25 - Equation 2.28. Additional pressure loss mechanisms (ΣP_{loss}) have an appreciable effect on only three of these interfaces (first-stage cathode, second-stage anode, and second-stage cathode).

$$P_{a1} = P_{a1,oc} - \Delta P_{slip}\left(T_{evap}, \rho\left(T_{evap}\right), \mu\left(T_{evap}\right), \varphi_1, j_1, G_1\right) \tag{2.25}$$

$$P_{c1} = P_{c1,oc} + \Delta P_{slip}\left(T_{evap}, \rho\left(T_{int}\right), \mu\left(T_{int}\right), \varphi_1, j_1, G_1\right) + \frac{j_1}{\varphi_1 F}\sqrt{2\pi \bar{R} M T_{evap}} + \sum P_{loss} \tag{2.26}$$

$$P_{a2} = P_{a2,oc} - \Delta P_{slip}\left(T_{int}, \rho\left(T_{int}\right), \mu\left(T_{int}\right), \varphi_2, j_2, G_2\right) - \frac{j_2}{\varphi_2 F}\sqrt{2\pi \bar{R} M T_{int}} - \sum P_{loss} \tag{2.27}$$

$$P_{c2} = P_{c2,oc} + \left(\frac{1}{\varphi_2} + \frac{3G_2}{8\pi}\right)\frac{j_2}{F}\sqrt{2\pi \bar{R} M T_{int}} + \frac{j_2}{F}\sqrt{2\pi \bar{R} M T_{cond}} + \sum P_{loss} \tag{2.28}$$

2.4.4 Dual-Stage Na-TEC Limiting Current and Maximum Power Density

The limiting current of the dual-stage Na-TEC is determined by the mass transport within the second-stage anode (Equation 2.29). This is because the limiting current corresponding to the first stage anode is larger, and therefore it does not represent the true device limit. Similar to the single-stage Na-TEC, the voltage is affected by this mass transfer limit at currents much higher than the short-circuit current. However, mass transfer has a stronger effect on the voltage in the dual-stage Na-TEC than in the single-stage Na-TEC (*i.e.*, $j_{lim,single} > j_{lim,dual}$, see Figure 2.1b). In the limit of very fast charge transfer kinetics

($B_1 \to \infty$, $B_2 \to \infty$), j_{sc} approaches j_{lim} and mass transfer effects in the second-stage dominate the performance of the dual-stage Na-TEC.

$$P_{a2,oc} = \Delta P_{slip}\left(T_{int}, \rho\left(T_{int}\right), \mu\left(T_{int}\right), \varphi_2, j_{lim}, G_2\right) + \frac{j_{lim}}{\varphi_2 F}\sqrt{2\pi \bar{R} M T_{int}} \qquad (2.29)$$

Unlike with the single-stage Na-TEC, there are two independent variables to consider with the dual-stage configuration because of the two stages. In a real device, the first-stage current density j_1 and the area ratio between the stages A_1/A_2 are the design variables. Unlike for the single-stage Na-TEC, there is not a simple analytical load matching condition for the dual-stage Na-TEC because the power density is a function of two current densities (j_1, j_2). Equation 2.30 is used to define the power density, which is normalized to the total (planar) electrolyte area ($A_1 + A_2$). The variable r_{load} represents the area-specific external load resistance (*e.g.*, $r_{load} = (A_1+A_2)R_{load}$) through which this power is dissipated. Figure 2.7a shows a contour plot of the power density in terms of the area ratio and first-stage current density. Figure 2.7 demonstrates that the point of maximum power and the point of maximum efficiency do not coincide, as is the case with all TRES.

$$\frac{IV}{A_1 + A_2} = V\left(\frac{1}{j_1} + \frac{1}{j_2}\right)^{-1} = r_{load}\left(\frac{1}{j_1} + \frac{1}{j_2}\right)^{-2} \qquad (2.30)$$

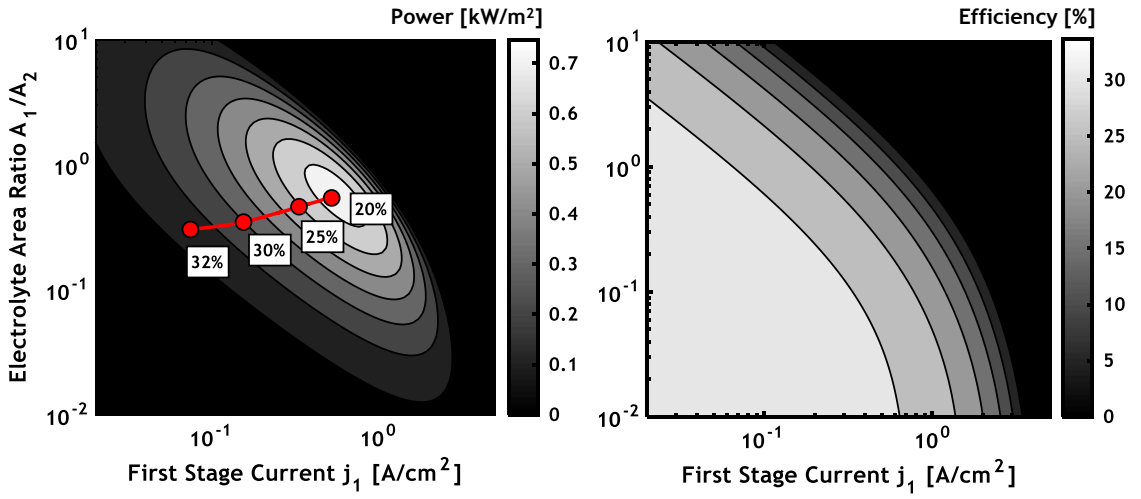

Figure 2.7 (a) Power density of a dual-stage Na-TEC (T_{evap} = 1150 K, T_{int} = 700 K, T_{cond} = 500 K) as a function of first-stage current density and the electrolyte area ratio. The red line indicates the point of maximum efficiency for each power contour. (B_1 = 110 A $K^{1/2}$ N^{-1}, B_2 = 600 A $K^{1/2}$ N^{-1}, G_1 = 10, G_2 = 10, $r_{Th,1}$ = 0.15 Ω cm^2, $r_{Th,2}$ = 0.15 Ω cm^2, η_{reg} = 100%, f = 0.1). (b) Efficiency of a dual-stage Na-TEC as a function of first-stage current density and the electrolyte area ratio.

2.4.5 Thermal Efficiency of a Dual-Stage Na-TEC

The dual-stage thermal efficiency must be modified to account for the regeneration and reheat steps (Equation 2.31). Here, the parasitic loss is normalized to the total (planar) electrolyte area (A_1 +A_2). A contour plot of the efficiency in terms of j_1 and A_1/A_2 is shown in Fig. 7b. The dual-stage Na-TEC operates more efficiently with a smaller area ratio and at smaller current densities, where the voltage drops are lowest. Figure 2.8 shows how the efficiency is affected by the voltage drop mechanisms at different power densities while using a fixed electrolyte area ratio. The efficiency and power in a dual-stage Na-TEC depend on the thirteen variables listed in Table 2.2. The values used for each variable are listed in the figure captions. These values are adapted from single-stage experimental data, assuming the use of a 500 μm thick β''-alumina electrolyte with a Rh_xW electrode (L_e = 1 μm, φ = 90%) for the first stage and a Mo electrode (L_e = 1 μm, φ = 90%) for the second stage.[11, 29, 70] The top line in Figure 2.8 indicates the open-circuit limit of the

efficiency. For a closed circuit, the maximum efficiency occurs when the kinetic polarization does not affect the overpotential (dashed black line, $B_1 \rightarrow \infty$, $B_2 \rightarrow \infty$ in Equation 2.24), which in general occurs at a lower current density than for the single-stage Na-TEC. This is because the overpotential loss is larger with the addition of a second stage. The mass transfer and kinetic polarizations are both larger in the dual-stage Na-TEC, each contributing roughly equally to the reduction in efficiency (black line). The Ohmic contributions (orange line) do not become significant until the system is operating closer to the maximum power. Similar to the single-stage Na-TEC, the parasitic loss is responsible for the largest drop in efficiency (gold line). An arbitrary and constant value for the parasitic loss fraction in Figure 2.8 is used to demonstrate the effect of this variable.

$$\eta = \frac{V(1-f)}{V + \frac{M}{F}\left(h_{fg}(T_{cond}) + \int_{T_{cond}}^{T_{int}} c_p(T)dT\right) + (1-\eta_{reg})\frac{M}{F}\int_{T_{cond}}^{T_{evap}} c_p(T)dT} \tag{2.31}$$

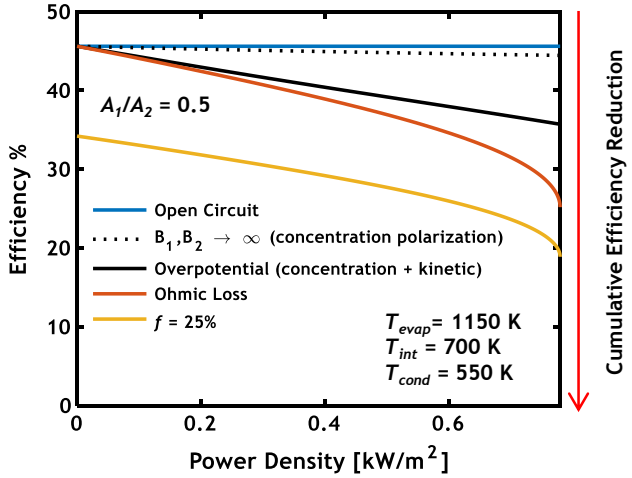

Figure 2.8 Efficiency vs. power density (normalized to the total electrolyte area A_1+A_2) of a dual-stage Na-TEC (T_{evap} = 1150 K, T_{int} = 700 K, T_{cond} = 550 K), where each curve shows the cumulative effect on the efficiency as each voltage drop mechanism is subtracted from the open-circuit voltage. (B_1 = 110 A K$^{1/2}$ N^{-1}, B_2 = 600 A K$^{1/2}$ N^{-1}, G_1 = 10, G_2 = 10, $r_{Th,1}$ = 0.15 Ω cm^2, $r_{Th,2}$ = 0.15 Ω cm^2, A_1/A_2 = 0.5, η_{reg} = 100 %).

In a real device, *f* decreases as current density increases just as it does for a single-stage device. For the dual-stage Na-TEC, the same thermal model that was used for the single-stage Na-TEC (Equation 2.20) is employed, but with three modifications (Equation 2.32). First, the radiation term now involves the second-stage cathode operating at T_{int}. Second, the total electrolyte area of the single- and dual-stage Na-TEC's are assumed to be equal, so the area of the radiating second-stage electrolyte is smaller than the radiating electrolyte area in the single-stage device; an area correction factor is therefore applied to the radiation term. Finally, the conduction term depends on an average hot-side temperature T_H. This temperature is defined by with average temperature based on the electrolyte areas (Equation 2.33). When the first-stage electrolyte area is greater than the second-stage ($A_1 >> A_2$), T_H approaches T_{evap}. Likewise, when $A_2 >> A_1$, T_H approaches T_{int}.

$$\dot{Q}''_{loss} = \left(\frac{1}{A_1/A_2 + 1} \right) \beta_1 \sigma \left(T_{int}^4 - T_{cond}^4 \right) + \beta_2 \left(T_H - T_{cond} \right) \tag{2.32}$$

$$T_H = \frac{T_{evap}}{1 + A_2/A_1} + \frac{T_{int}}{1 + A_1/A_2} \tag{2.33}$$

Table 2.2 Dual-Stage Na-TEC Parameters

Thermodynamic	T_{evap}	Evaporator Temperature [K]
	T_{int}	Intermediate Temperature [K]
	T_{cond}	Condenser Temperature [K]
Independent	j_1	1st Stage Current Density [A cm^{-2}]
	A_1/A_2	Electrolyte Area Ratio
Electrochemical	r_1	1st Stage Resistance [Ω cm^2]
	r_2	2nd Stage Resistance [Ω cm^2]
	G_1	1st Stage Morphology Factor

	G_2	2nd Stage Morphology Factor
	B_1	1st Stage Temp. Indep. Exchange Current [A $K^{1/2}$ N^{-1}]
	B_2	2nd Stage Temp. Indep. Exchange Current [A $K^{1/2}$ N^{-1}]
Heat Transfer	η_{reg}	Regeneration Efficiency [%]
	f	Parasitic Heat Loss Fraction [%]

2.5 Comparing the Performance of the Single- and Dual-Stage Na-TEC

2.5.1 Determining a Thermodynamic Basis of Comparison

A thermodynamic comparison between the single- and dual-stage Na-TEC can be performed in two different ways: (i) using a fixed hot-side temperature and a fixed cold-side temperature (Figure 2.9), and (ii) using a fixed a hot-side temperature and a fixed heat input (Figure 2.6b). When dealing with real prototypes, it is standard to compare devices using the later approach by fixing the total heat input and assuming both devices are in contact with the same hot-side thermal reservoir. These boundary conditions allow the dual-stage condenser temperature to go lower than its single-stage counterpart when reheating and regeneration from the first-stage isobaric cooling are included (Figure 2.9). This lower dual-stage condenser temperature is determined for a given intermediate temperature and a single-stage condenser temperature by fixing the total heat input. With this approach, the corresponding dual-stage condenser temperature must be recalculated whenever the operating power changes because the total heat input changes as well. Rather than performing this recalculation, the heat input in the limit of zero current can be used as it is the most conservative case. In this limit, it is only necessary to solve for the dual-stage condenser temperature (variable χ) as a function of the single-stage condenser temperature by equating the heat input for both systems (Equation 33).

$$V_{oc}+\frac{M}{F}\left(h_{fg}\left(T_c\right)+\int_{T_{cond}}^{T_{evap}} c_p(T)dT\right)= \\ V_{oc,1}+V_{oc,2}+\frac{M}{F}\left(h_{fg}\left(\chi\right)+\int_{\chi}^{T_{int}} c_p(T)dT\right)+\left(1-\eta_{reg}\right)\frac{M}{F}\int_{T_{int}}^{T_{evap}} c_p(T)dT \tag{2.34}$$

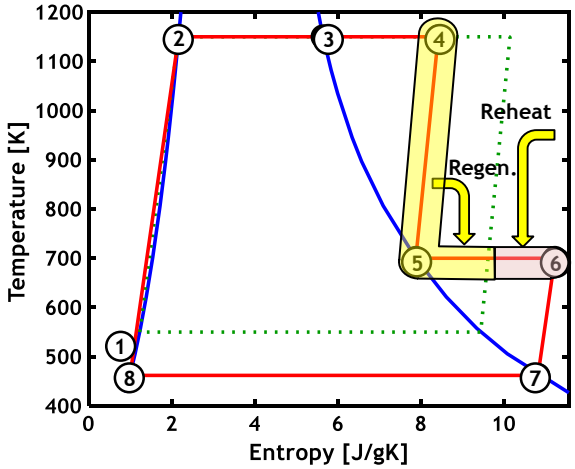

Figure 2.9 Temperature-Entropy (T-S) diagram of the ideal dual-stage Na-TEC thermodynamic cycle (red lines) overlaid on top of the sodium saturation curves (blue lines), where each number corresponds to a state of the system. A single-stage Na-TEC cycle (green dotted lines) with the same heat input as the dual-stage cycle is shown beneath. The yellow highlighted region shows the regeneration and reheat steps.

For an theoretical thermodynamic analysis in the absence of a prototype, however, approach (i) is more appropriate. Thus, to compare the thermodynamic operation of the single- and dual-stage Na-TEC, a scenario where both devices are in contact with the same thermal reservoirs is considered such that the evaporator and condenser temperatures are the same in each device (see Figure 2.6b). These boundary conditions are used for the analysis in Section 2.5.2. It is further assumed that the regeneration efficiency between the first- and second-stage is 100%. This assumption is valid when neglecting heat lost to the surroundings in the parasitic loss term (*i.e.*, a perfectly insulated system). This assumption is further justified by considering that only a small amount of heat will escape the

intermediate plenum with a reheat pathway into the second-stage electrolyte. Furthermore, electrode materials whose performance would otherwise degrade quickly at the elevated evaporator temperatures can be used in the lower temperature second-stage; where their superior performance at lower temperatures can be exploited. For this purpose, porous molybdenum is a good choice for the second-stage electrode ($B \approx 600$ A $K^{1/2}$ N^{-1}).[70]

2.5.2 Application Regime for the Single- and Dual-Stage Na-TEC

The efficiency of a reversible thermodynamic cycle is proportional to the area enclosed in the temperature-entropy (T-S) diagram. In the reversible limit, the dual-stage cycle is inferior to the single-stage cycle because part of the heat input occurs at an intermediate temperature, which reduces the total area of the dual-stage cycle in the T-S diagram (Figure 2.7b). Furthermore, the total voltage generated in the dual-stage Na-TEC is lower because it has significant overpotential contributions from three electrodes (the first-stage cathode, the second-stage anode, and the second-stage cathode) compared to a contribution from just one electrode (cathode) in the single stage Na-TEC. The addition of a second stage also increases the magnitude of the Ohmic resistance. The dual-stage Na-TEC only becomes competitive once the parasitic loss that is present in realistic devices is considered, which is the dominant factor affecting the system efficiency. In general, since the average operating temperature decreases with multiple stages, one can expect that the parasitic loss will be lower in the dual-stage device because it operates at a lower average temperature. According to prior experimental, the best performing single-stage prototypes have operated with a parasitic loss fraction of ≈45% at peak efficiency.[58, 78] Using this value for the parasitic loss fraction, a regime map (Figure 2.10) can be created to guide the selection of either the single- or dual-stage Na-TEC. All other variables are the same as those used in Figure 2.3 and Figure 2.8 for the single- and dual-stage Na-TEC, respectively. This map depicts which system is more desirable based on the power density and the dual-stage parasitic loss fraction. When the dual-stage Na-TEC operates with a parasitic loss

larger than 45% (f_{dual} > 45%), it is always more efficient to use a single-stage architecture. If the parasitic loss fraction is less than 45%, it is more efficient to operate with a dual-stage Na-TEC as long as the power density is below the regime boundary. The regime boundary is determined by fitting a polynomial to the intersection points of the efficiency vs. power density curves of the single- and dual-stage Na-TECs at varying magnitudes of f_{dual}. Another aspect shown in Figure 2.10 is that the maximum power density of the single-stage Na-TEC is higher than the maximum power density of the dual-stage Na-TEC. This is a consequence of using two electrolytes for the dual-stage, which inevitably increases the total electrochemical reaction area and thereby reduces the power density. From Figure 2.10, the single-stage Na-TEC must be used to achieve power densities > 0.744 kW m^{-2}.

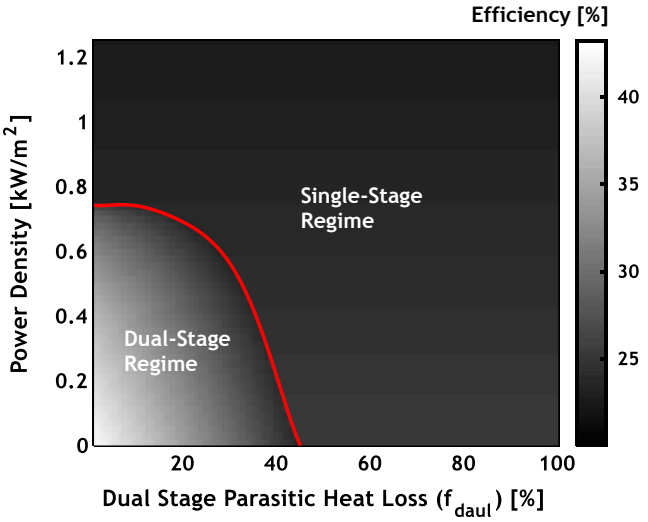

Figure 2.10 Regime map of the most efficient (single- or dual-stage) Na-TEC in terms of the power density and the dual-stage parasitic loss fraction. The red line indicates the regime boundary, assuming a single-stage parasitic heat loss f = 45%. The color map illustrates the efficiency and power density trade-off. For the single-stage, the variables used are: (T_{evap} = 1150 K, T_{cond} = 550 K, B = 120 A $K^{1/2}$ N^{-1}, G = 50, r_{Th} = 0.25 Ω cm^2, f = 0.45). For the dual-stage, the variables used are: (T_{evap} = 1150 K, T_{cond} = 550 K, T_{int} = 700 K, B_1 = 110 A $K^{1/2}$ N^{-1}, B_2 = 600 A $K^{1/2}$ N^{-1}, G_1 = 10, G_2 = 10, $r_{Th,1}$ = 0.15 Ω cm^2, $r_{Th,2}$ = 0.15 Ω cm^2, A_1/A_2 = 0.5, η_{reg} = 100 %).

Previous single-stage Na-TEC prototypes have struggled to achieve a high efficiency due to conduction loss to the condenser (through the device enclosure walls and

capillary wick) and radiation loss (via direct radiative energy exchange) between the cathode and the condenser.[48] For the dual-stage device, the average hot-side temperature in a dual-stage device is smaller, thereby reducing the total parasitic conduction loss. Furthermore, the second-stage will directly radiate to the condenser at T_{int} as opposed to T_{evap}, so the heat that bypasses the thermo-electrochemical process can be reduced without the need for additional radiation shields. Table 2.3 shows the potential gains in efficiency by transitioning to a dual-stage Na-TEC when employing the model introduced in Section 2.4.5. For the operating conditions of j_1 = 0.58 A cm^{-2} and A_1/A_2 = 0.74, the dual-stage Na-TEC is predicted to have an efficiency of almost 26.5%, which is 7.5% points above the highest efficiency single-stage device (≈ 19%). By optimizing the two independent variables (see Table 2.2), the maximum power is found to be 2.22 kW m^{-2}. It must be reemphasized that this model does not account for heat lost directly to the surroundings.

Table 2.3 Efficiency comparison between a single- and dual-stage Na-TEC (T_{evap} = 1150 K, T_{cond} = 550 K) for reversible cycles and after adding irreversibilities. For the dual-stage, the variables used are: (T_{int} = 1050 K, B_1 = 110 A K$^{1/2}$ N^{-1}, B_2 = 600 A K$^{1/2}$ N^{-1}, G_1 = 10, G_2 = 10, $r_{Th,1}$ = 0.15 Ω cm^2, $r_{Th,2}$ = 0.15 Ω cm^2, η_{reg} = 100 %).

	Single-Stage	**Dual-Stage**
Maximum Reversible Efficiency	46.5 %	45.2 %
With Irreversibilities (Electrochemical and Thermal Parasitic Loss)	≈ 19%	≈ 26.5%

Finally, the intermediate temperature that yields the maximum power and the maximum efficiency can be found for a general combination of operating variables. Figure 2.11a shows the efficiency and the maximum power density as a function of the

intermediate temperature. These efficiency calculations continue relying upon the simple heat transfer model (Equation 2.32). The maximum power density is a monotonically increasing function of the intermediate temperature. The overall maximum power density occurs in the limit where the dual-stage Na-TEC resembles a single stage Na-TEC (*i.e.*, T_{int} approaches T_{evap}). Thus, for high power applications it is necessary to increase the intermediate temperature as much as possible (*i.e.*, in the limit that the dual-stage acts as a single-stage Na-TEC). The maximum efficiency with respect to the intermediate temperature is a function of j_1 and A_1/A_2.[77] Figure 2.11a shows that the efficiency is maximized at T_{int} = 790 K for j_1 = 0.35 A cm^{-2} and A_1/A_2 = 0.5. In this example, the efficiency does not deviate by more than ± 2.5% points across all intermediate temperatures because it is a weak (flat) function of the intermediate temperature. For a fixed current density, the efficiency is maximized within a certain band of electrolyte area ratios (between A_1/A_2 = 0.2 and A_1/A_2 = 2.1 in Figure 2.11b). For A_1/A_2 > 0.7, the thermal efficiency generally increases with rising intermediate temperatures.

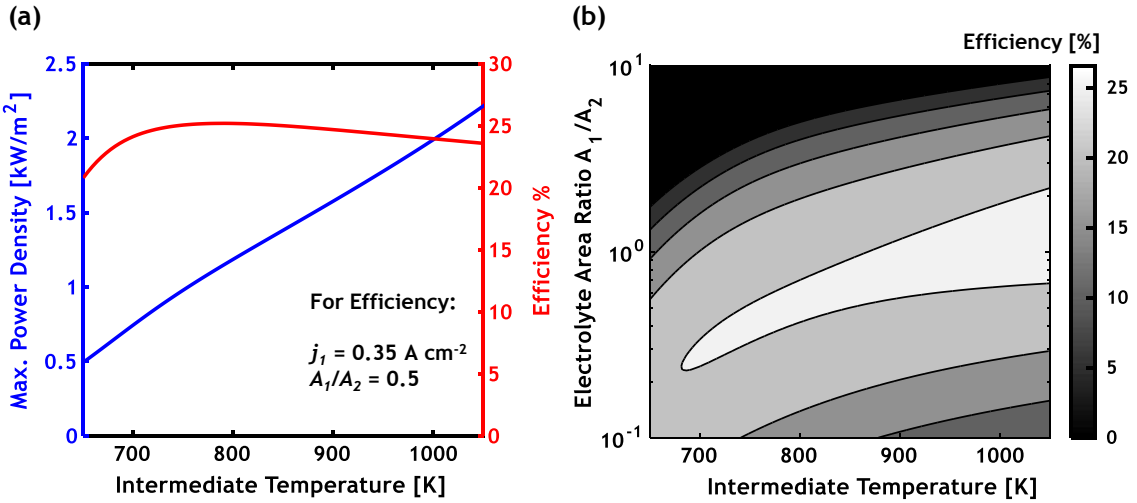

Figure 2.11 Maximum power and efficiency as a function of the intermediate temperature for T_{evap} = 1150 K and T_{cond} = 550 K and (B_1 = 110 A K$^{1/2}$ N^{-1}, B_2 = 600 A K$^{1/2}$ N^{-1}, G_1 = 10, G_2 = 10, $r_{Th,1}$ = 0.15 Ω cm^2, $r_{Th,2}$ = 0.15 Ω cm^2, A_1/A_2 = 0.5, j_1 = 0.35 A cm^{-2}, η_{reg} = 100 %). (b) Efficiency of a dual-stage Na-TEC as a function of the intermediate temperature and the electrolyte area ratio (T_{evap} = 1150 K, T_{cond} = 550 K, j_1 = 0.35 A cm^{-2}).

2.6 Summary

In this chapter, the dual-stage Na-TEC has been introduced as a more efficient alternative to the conventional single-stage Na-TEC. Expressions for the voltage, thermal efficiency, and maximum power density for a dual-stage Na-TEC are derived and used to probe the thermodynamic operating space for this technology. The power density of a dual-stage Na-TEC is limited by overpotential and Ohmic contributions from two stages, whereas the single-stage Na-TEC is only affected by a single electrochemical stage. Thus, the single-stage Na-TEC achieves a higher power density for the same total electrolyte area. The dual-stage Na-TEC, however, can operate with a higher thermal efficiency. Using a simple heat transfer model, it has been shown that the conduction and radiative parasitic heat losses through the device are reduced with a dual-stage configuration because the average temperature of the device is lower, so these heat transfer mechanisms occur across a smaller temperature difference. This manifests as a smaller parasitic heat loss fraction f (*i.e.,* fraction of heat input lost parasitically). Furthermore, the dual-stage device can support regeneration and reheating processes, which allow for better utilization of the supplied heat. Assuming high performance electrodes are used in a device (Rh_xW for the first stage and Mo for the second stage), an application regime map was created to guide the selection of a single- or dual-stage Na-TEC based on the power density and the parasitic loss fraction. In applications where a high power density is essential (*e.g.,* due to a low availability of β''-alumina), a single-stage device should be used. However, when a high thermal efficiency is required (*e.g.,* because of high fuel costs), then a dual-stage Na-TEC should be used due to its potential advantage in thermal management. Using a simple heat transfer model, it is predicted that the practical efficiency of a dual-stage Na-TEC can

approach 26.5%, which is 7.5% points larger than the highest efficiency single-stage Na-TEC, whose maximum practical efficiency is ≤ 19%, while the maximum power density approaches 2.22 kW m^{-2}.

Much of the content in this chapter was published in *Journal of Power Sources*, Vol. 371, A. Limia *et. al.*, "A dual-stage sodium thermal electrochemical converter (Na-TEC)", 217-224, Copyright Elsevier (2017)

CHAPTER 3. REDUCED-ORDER DUAL-STAGE NA-TEC MODEL

This chapter presents a detailed thermal analysis to estimate the thermal parasitic losses of a dual-stage Na-TEC design using a reduced-order finite-element model. Similar methods to those used to analyze other electrochemical systems are employed herein.[80-82] Section 3.1 describes the design of a quasi-axisymmetric dual-stage Na-TEC, including the materials selection for various sections. Several reduced-order simplifications for conduction and radiation heat transfer are discussed in Section 3.2. The computation of the power and thermal efficiency of this design is presented in Section 3.3. This section also includes a brief discussion on the cost of producing electricity with this dual-stage Na-TEC. Finally, Section 3.4 summarizes the key findings in this chapter, with the aim of answering the thesis question: *To what degree can a reduced-order model be used to effectively design a dual stage Na-TEC to operate at the maximum practical efficiency?*

3.1 Quasi-Axisymmetric Dual-Stage Na-TEC Design

A quasi-axisymmetric design for the dual-stage Na-TEC (Figure 3.1a) is presented, with a cylindrical heat source aligned to the interior face at r = 1.3 cm used to supply heat to the evaporator.[83] The outer and inner radii of the first- and second-stage annuli are constrained by the size of the planar β''-alumina electrolyte, which is commercially available in squares of 7.5 cm (Ceramatec Inc., 2017) with thickness t_β = 500 μm. The solid-electrolytes in each stage are segmented with spokes to form an annulus from the square β''-alumina pieces (Figure 3.1b). A 2D representation of this quasi-axisymmetric

design is depicted in Figure 3.2a. This geometry is divided into four zones to simplify the heat transfer analysis. The materials used for the housing must withstand high temperatures and a corrosive liquid sodium environment; therefore, the enclosure and evaporator can be made from vanadium, while the lower-temperature condenser can be made from stainless steel 316 (SS 316). Both of these materials have been identified previously as adequate candidates for a Na-TEC.[84]

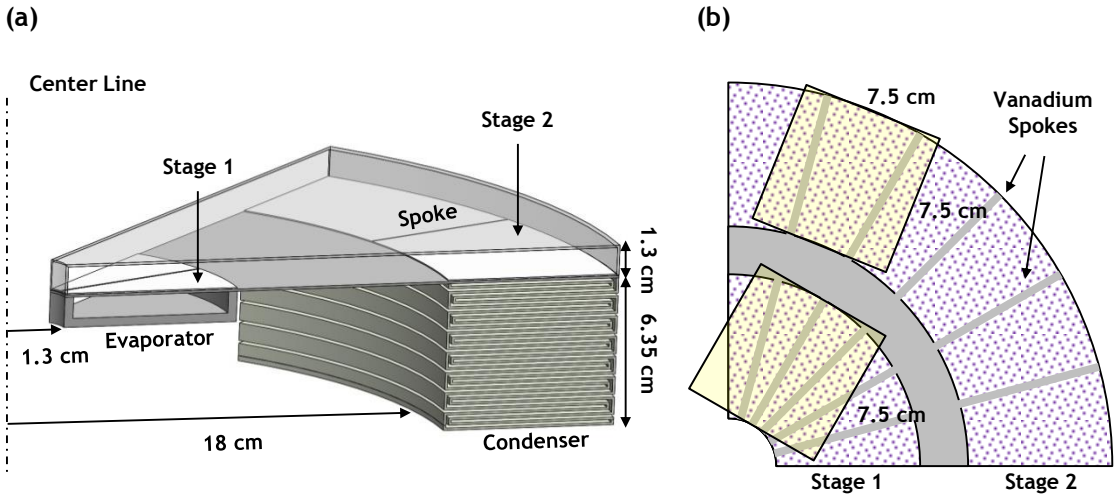

Figure 3.1 (a) 3D representation (1/8 piece) of the dual-stage module design. (b) The β''-alumina is a square 7.5 cm piece that is cut into segments to form the full solid-electrolyte annulus. The yellow, transparent, square overlays over each stage show how the segments can be machined out of the square stock piece. Vanadium spokes separate the in the β''-alumina segments in Stage 1 and Stage 2.

To set a baseline on the minimum thermal parasitic losses, the Na-TEC is assumed to be perfectly insulated, so only bypass heat contributes to the thermal parasitic loss (hereafter referred to as parasitic loss, see Chapter 2).[77] To determine the magnitude of

the parasitic loss, a reduced-order finite-element model (in COMSOL) is used in combination with the analytical dual-stage Na-TEC thermodynamic model developed previously.[77] This combined approach allows for linking of the average temperature at stages 1 and 2 (electrochemically active regions) to the power extraction (sinks $W_{e,1}$ and $W_{e,2}$). Contributions from conduction and radiation are considered separately within each zone, and adjacent zones are coupled via continuity of temperature and heat flow at each interface. The evaporator (Zone 1) and condenser (Zone 3) are connected with a liquid-return path (see Figure 3.5b) that supplies the evaporator with liquid sodium through a capillary mechanism.[11, 44] A separate analytical model is developed to calculate the parasitic loss through this liquid-return path. A thermal resistance circuit (Figure 3.2b) describes the strategy used for computing the parasitic loss from the evaporator to the condenser, similar to prior analyses used for electrochemical systems.[36, 85]

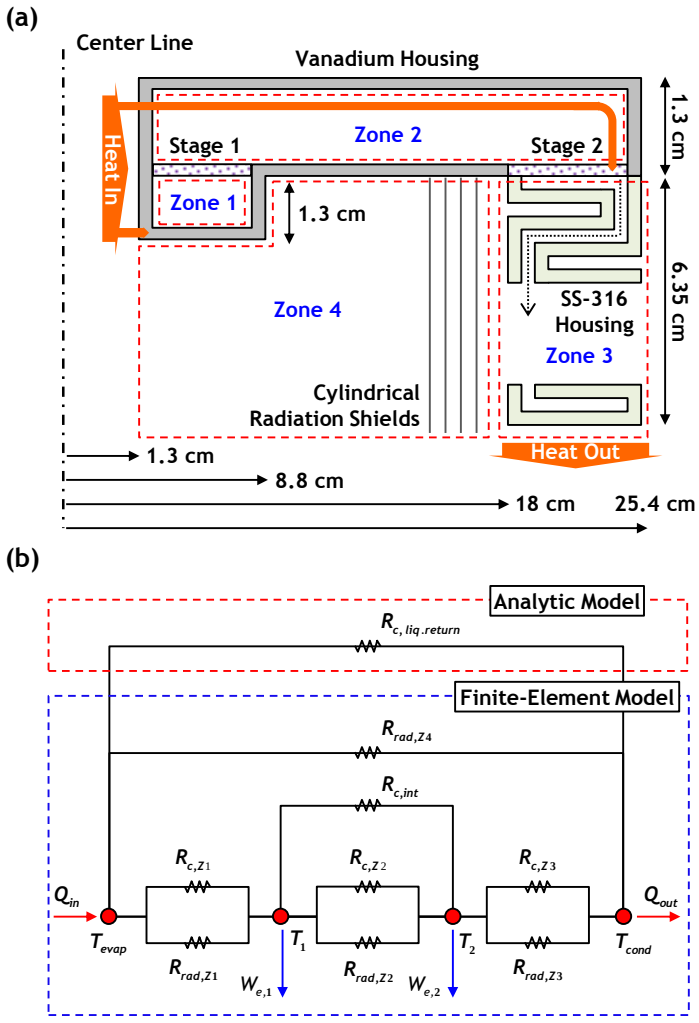

Figure 3.2 (a) Axisymmetric model of an individual dual-stage module. The corrugated structure in Zone 3 is made of SS 316, while the remainder of the housing is made of vanadium. Zones 1-3 comprise the interior of the device, while Zone 4 is exterior to the device. The heat input to the second-stage (reheat, see Figure 2.6) is not treated as a separate heat input in this model. (b) Equivalent thermal resistance circuit for steady-state operation (*i.e.*, no storage terms) used to calculate the parasitic bypass loss.

3.2 Reduced-Order Model Features

3.2.1 Conduction Heat Transfer through the Na-TEC Enclosure

The upper limit of performance can be determined by considering only the parasitic loss caused by conduction. Figure 3.2b shows the four temperature nodes to consider. Each

electrolyte is considered a single temperature node because the electrochemical conversion ideally occurs isothermally. The other two are: (*i*) the evaporator surface (r = 1.3 cm) from which heat enters and (*ii*) the condenser surface from which all heat is rejected (see Figure 3.2a). All other surfaces are adiabatic. The thermal resistance is $R_{th} = l_{tot}\, k^{-1} A_c^{-1}$, where l_{tot} is the physical length through which the heat travels between nodes. Conduction heat transfer is found simply by setting the temperature difference across the evaporator/condenser and dividing it by the combined thermal resistance from each segment.

The parasitic loss must be reduced to improve efficiency, so the thermal resistance between the second-stage electrolyte and the condenser (*i.e.,* Zone 3) should be increased. However, the cross-sectional area A_c cannot be made arbitrarily thin because the Zone 3 walls should be mechanically robust. Thus, a wall thickness of t = 1 mm is used throughout the structure except in the evaporator (Zone 1), where t = 3.8 mm to promote heat conduction. Furthermore, SS 316 is used in the condenser, with a thermal conductivity of $k_{316} \approx 20$ W/mK (estimated as the geometric-mean for the Zone 3 temperature range).[86] Therefore, to increase the thermal resistance, the only remaining option is to increase the heat transfer path l_{tot}. The height of Zone 3 is fixed at H = 6.3 cm to constrain the Na-TEC to an application-relevant size. However, the path length can be effectively increased by creating corrugated structures (Figure 3.3), which repeat within the condenser height. The height of each individual repeating unit is $h = H/N$, where N is the total number of repeating corrugated units within height H. The thickness of the vapor channel in the axial direction $t_{gap,v}$ and the thickness of the external gaps (refer to Figure 3.3) are equal, while the thickness in the radial direction is set to $t_{gap,h}$ = 1 mm. The thickness of the vapor gaps (refer

to Figure 3.3) are constrained to $t_{gap,v}$ > 1 mm (*i.e.*, gaps should not be thinner than the walls). This condition physically limits the number of repeating corrugated units that fit within a given height (*e.g.*, 7 units for H = 6.3 cm). The thermal resistance of the left corrugated wall is well approximated (<1% error) by accounting for the corners in the vertical direction (Equation 3.1), while the right corrugated wall thermal resistance is well approximated (<1% error) by ignoring the corners (Equation 3.2). The Zone 3 conduction thermal resistance is the parallel combination of these resistances, with outer and inner radii r_a = 18 cm and r_b = 25.4 cm.

$$R_{th,left} = \left(\frac{1}{\pi k_{316} t}\right)\left(\frac{h - t_{gap,v}}{(2r_a + t)} + ln\left(\left(r_b - 2t - t_{gap,h}\right) \Big/ \left(r_a + t\right)\right) + \frac{2t + t_{gap,v}}{\left(2\left(r_b - t - t_{gap,h}\right) - t\right)}\right) \quad (3.1)$$

$$R_{th,right} = \left(\frac{1}{\pi k_{316} t}\right)\left(\begin{array}{l} \dfrac{h - 2t - t_{gap,v}}{(2r_b - t)} + ln\left(\sqrt{r_b\left(r_b - t\right)} \Big/ \left(r_a + 2t + t_{gap,h}\right)\right) + \cdots \\ \dfrac{t_{gap,v}}{\left(2\left(r_a + t + t_{gap,h}\right) + t\right)} \end{array}\right) \quad (3.2)$$

To complete the conduction model, two additional aspects must be addressed. First, the spokes in the first- and second-stage electrolytes (Figure 3.1b) increase conduction between the two stages because they are made of vanadium ($k_V \approx$ 35 W/m/K), whereas the β''-alumina has a lower thermal conductivity ($k_\beta \approx$ 2.5 W/m/K) in the temperature range of the Na-TEC.[86, 87] An effective thermal conductivity for the electrolytes is used to consider the increased conduction caused by the spokes. Using Equation 3.3, k_{eff} is determined by finding the parallel combination of the thermal resistances of the N_{seg} electrolyte segments and the thermal resistance of the spokes with thickness t_{spk}, and then

equating this parallel combination to an effective thermal resistance. In Equation 3.3, the number of spokes equals the number of electrolyte segments $N_{spk} = N_{seg}$. This effective thermal conductivity replaces the β''-alumina thermal conductivity in the finite-element calculations. Similar approaches have been previously employed in thermal circuits used to study other electrochemical systems.[85] Second, the sodium phase change in the evaporator/condenser is considered by adding a volumetric heat source/sink (equivalent to the latent heat of vaporization) to a thin domain in the finite-element model that represents the phase change interface. Physically, the phase change process occurs isothermally at the saturation temperature. To approximate this isothermal condition, the thermal conductivity of the liquid sodium in these thin computational domains is made artificially high ($k \geq 10^4$ W/m/K). This modification approximates an isothermal surface for the phase change processes while having a negligible effect on the conduction results.

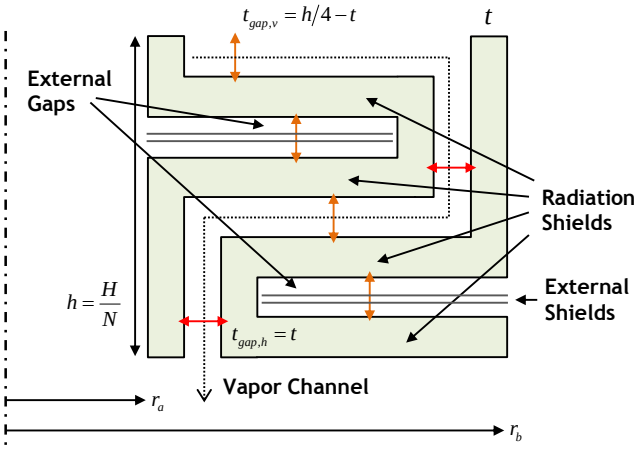

Figure 3.3 One repeating corrugated unit of height h used in Zone 3.

Figure 3.4 shows the thermal efficiency as a function of power when considering only conduction. These curves are generated by calculating the power and efficiency over a range of first-stage current densities j_1. At each current density, an initial guess for both

β''-alumina temperatures is used to calculate the power and efficiency using the analytical thermodynamic model for the dual-stage Na-TEC described in Chapter 2.[77] Next, the electric power calculated for each stage is applied to the nodes in the thermal resistance model as a thermal energy sink (Figure 3.2b), and the corresponding nodal temperatures are determined. This process is repeated iteratively until the solution converges for each current density. This analysis is used to predict the limiting performance of the dual-stage Na-TEC. For example, if an application requires 50 W with 20% efficiency, then Figure 3.4 suggests that the design must include at least one corrugated unit to reduce conduction parasitic losses.

$$\left(\frac{k_\beta t_\beta \left(2\pi - N_{seg} t_{spk} / r_b\right)}{ln\left(r_b / r_a\right)} + \frac{k_v N_{seg} t_\beta t_{spk}}{r_b - r_a} \right)^{-1} = \frac{ln\left(r_b / r_a\right)}{2\pi k_{eff} t_\beta} \tag{3.3}$$

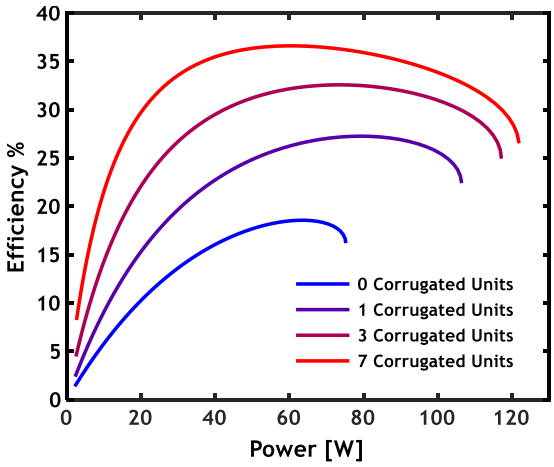

Figure 3.4 Efficiency vs. power of the dual-stage Na-TEC for different numbers of corrugated units in Zone 3, when considering only conduction through the structure.

3.2.2 Conduction Heat Transfer in the Liquid-Return Path

Conduction and advection occur along the liquid-return path from the evaporator to the condenser. Liquid sodium flows through a set (N_{tube}) of circular cross-section liquid-return tubes distributed symmetrically around the center line (Figure 3.5a). The tubes are placed directly along the exterior boundary in Zone 4 (Figure 3.5b) so that they will have a similar temperature to the walls. Radiation from the outer tube surface can then be reasonably neglected. Thus, only heat conduction and advection comprise the bypass loss through these tubes, which occurs in parallel along the tube walls (made of SS 316) and through the flowing liquid sodium (see Figure 3.6 inset). The thermal conductivity used for liquid sodium is k_{Na} = 62 W/m-K, calculated at the geometric mean of the evaporator and condenser temperatures.[88]

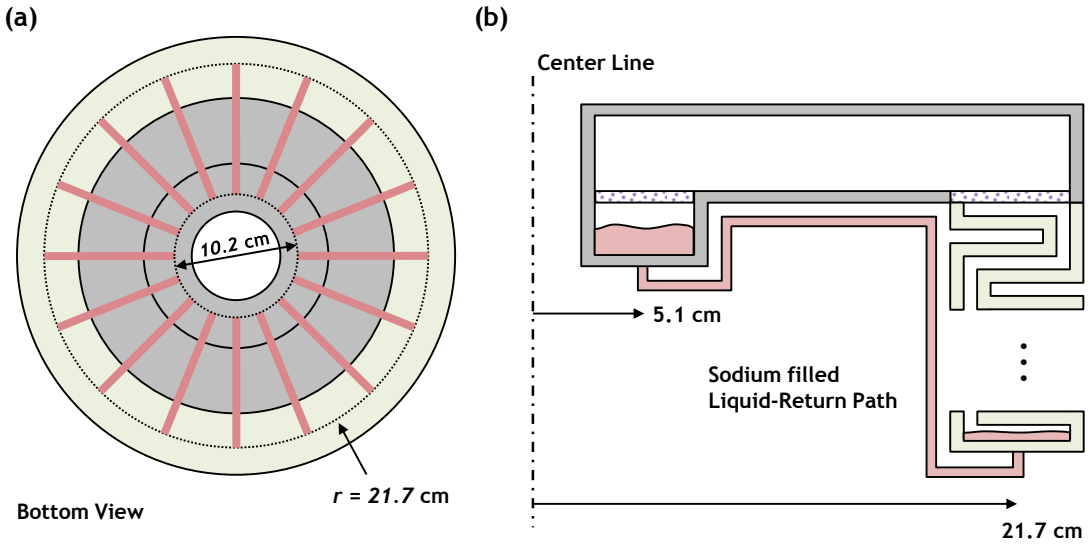

Figure 3.5 (a) Bottom view of the dual-stage Na-TEC design, with 16 radially symmetric liquid return paths. (b) Geometry of the liquid return tube following the Zone 4 exterior wall. The tube has six 90^o bends. Due to the proximity of the liquid return tube to the device walls, radiation at the outer surface is neglected.

The liquid sodium and the SS 316 tube are treated as separate domains in a general conduction model, with a further assumption of an adiabatic outer-tube surface (*i.e.*, negligible radiation and natural convection). A quasi one-dimensional assumption is employed (using mean radial temperatures at all axial locations) such that the physical problem reduces to two coupled differential equations with isothermal boundary conditions (corresponding to the evaporator/condenser). For internal convection between the two domains, fully-developed laminar flow is assumed with Nu = 4.36 for an approximately constant surface heat flux.[86] The effects of secondary flow along the tube bends (Figure 3.5b) are reasonably ignored due to low flowrates ($\dot{m} < \approx 10^{-7}$ kg/s per liquid-return tube), so the model length L is simply the total length of tubing. An analytical solution can be obtained when further reducing the problem to a single differential equation (Equation 3.4) by assuming the tube and sodium are in local thermal equilibrium, with an effective thermal conductivity that treats these two as parallel heat transfer paths. The Peclet number Pe (Equation 3.5) is directly proportional to the mass flowrate, which is itself proportional to the current density and inversely proportional to the number of tubes N_{tube}. Since sodium advection occurs in the opposite direction of conduction (see Figure 3.6 inset), when the advection term becomes negligible the parasitic conduction loss is maximized (that is, all heat is conducted to the condenser). Thus, as $Pe \rightarrow \infty$ the advection dominates the energy transport and there is essentially zero parasitic loss. When, $Pe \rightarrow 0$ however, the advection term becomes negligible and the parasitic loss is maximized (all heat travels to the condenser via thermal conduction). For typical sodium mass flowrates in the Na-TEC (on the order of $\dot{m} \approx 10^{-6}$ kg/s) the condition of $Pe \rightarrow 0$ is reasonably satisfied.

$$\frac{d^2T}{dx^2}+\left(\frac{Pe}{L}\right)\frac{dT}{dx}=0 \quad \begin{cases} T\left(x=0\right)=T_{evap} \\ T\left(x=L\right)=T_{cond} \end{cases} \tag{3.4}$$

$$Pe=\frac{\dot{m}c_pL}{k_{eff}A_c}=\left(j_1\frac{M}{N_{tube}F}\right)\frac{c_pL}{k_{eff}A_c} \tag{3.5}$$

$$q_{bypass}=-N_{tube}k_{eff}A_c\left.\frac{dT}{dx}\right|_{x=L}=N_{tube}k_{eff}A_c\frac{T_{evap}-T_{cond}}{L}\left(\frac{Pe\cdot e^{-Pe}}{1-e^{-Pe}}\right) \tag{3.6}$$

The parasitic conduction loss (Equation 3.6) is the total heat transferred at x = *L* (the condenser end of the tube). Larger sodium flowrates (*i.e.*, higher current densities) reduce the net heat transferred, but they simultaneously increase the pressure drop (Figure 3.6). These pressure drops consist of the gravitational pressure head, laminar flow viscous losses, and minor-losses associated with the tube geometry. These pressure drops along the liquid return path must be smaller than the difference between the Laplace pressure generated by a capillary wick pump and the evaporator pressure ($P_{loss} < P_L - P_{evap}$).[59] Since the liquid return path follows directly along the Zone 4 boundary (to minimize radiation parasitic loss), six 90^o tube bends are required to link the evaporator and the condenser (see Figure 3.5b) which generate minor-losses for the flowing sodium.[89] There is also an expansion and contraction pressure loss at the evaporator and condenser respectively, both of which contribute to the minor-losses. However, the gravitational pressure head (≈ 400 Pa) accounts for > 80% of the total pressure drop. Optimally, the operating current balances the tradeoff between conduction and the pressure losses. For 16 liquid return tubes (N_{tube} = 16), each with a wall thickness of 1.3 mm and outer diameter of 3.2 mm, the conduction loss is ≈ 3 W and the pressure drop is ≈ 440 Pa for j_1 = 0.6 A cm^{-2}

in Figure 3.6. It must be noted that the effect of the pressure drop on the pump work is not explicitly considered in the final efficiency calculations (see Section 3.3), because the pump work is much smaller than the power produced by the electrochemical process.

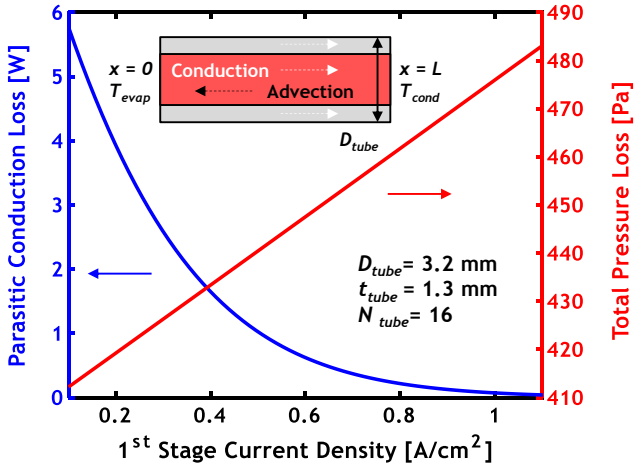

Figure 3.6 Total conduction parasitic loss (left axis) and pressure loss (right axis) along the liquid-return path as a function of first-stage current density. (Inset) Geometry of the liquid return path showing the opposite directions of sodium advection and thermal conduction. The inlet boundary condition is isothermal at T_{evap} while the outlet is isothermal at T_{cond}.

3.2.3 Radiation Heat Transfer in Zone 3

All the surfaces in this design are assumed to be gray and diffuse with temperature-independent emissivities. Also, the sodium vapor within each zone can be considered transparent to thermal radiation for temperatures below 4000 K.[90] Radiation exchange within Zone 1 and Zone 2 is negligible because the radiating surfaces have similar temperatures. Radiation in Zone 3 is the most important parasitic loss mechanism in the interior of the Na-TEC. The corrugated walls in Zone 3 make it challenging to calculate the radiation exchange using the finite-element model without increasing computational time (via reduction in element size). Instead, each corrugated wall can be treated as a flat,

infinitely long, linear radiation shield. The net Zone 3 radiation can then be modeled as the exchange between the second-stage electrolyte and the condenser bottom, separated by radiation shields. This assumption is valid when the view factor between each parallel face of the corrugated walls (see Appendix A) is close to unity such that radiation exchange with the side walls can be neglected, which is the case for $N \geq 3$ corrugated units (Figure A.1).[91] Assuming that the temperature difference across walls in Zone 3 is negligible in the axial direction (*i.e.*, thin walls), all four horizontal walls in the repeating corrugated unit (see Figure 3.3) can be treated as radiation shields. These are made of SS 316 with an approximate emissivity $\varepsilon_{316} = 0.6$.[86] The second-stage electrolyte surface is covered with a porous electrode that can be treated as an effective blackbody.[92] Finally, the condenser is covered with highly-reflective liquid sodium, but a conservative emissivity $\varepsilon_{cond} = 0.25$ is used to account for potential fouling of the liquid film by the corrosion products between sodium and stainless steel.[93, 94] For N corrugated units and a view factor of unity between each shield, Equation 3.7 describes the Zone 3 radiative resistance.

$$R_{rad,Z3} = \frac{1/\varepsilon_{cond} + (4N)(2/\varepsilon_{316} - 1)}{A_{c,2}\sigma\left(T_2^2 + T_{cond}^2\right)\left(T_2 + T_{cond}\right)} \tag{3.7}$$

The total Zone 3 thermal resistance can be increased by placing additional radiation shields in the external gaps (*i.e.* outside the vapor channel) of the corrugated unit shown in Figure 3.3. These external shields (*es*) can be made of vanadium with an emissivity $\varepsilon_{es} = \varepsilon_V = 0.21$.[95] These shields are treated as infinitely long because the view factor between each one is very close to one (Figure A.2).[91] If the same number of external shields N_{es}

are added to each external gap (two gaps per corrugated unit), the enhanced radiative thermal resistance is given by Equation 3.8.

$$R_{rad,Z3} = \frac{1/\varepsilon_{cond} + N\left(4\left(2/\varepsilon_{316} - 1\right) + 2N_{es}\left(2/\varepsilon_{es} - 1\right)\right)}{A_{c,2}\sigma\left(T_2^2 + T_{cond}^2\right)\left(T_2 + T_{cond}\right)} \tag{3.8}$$

Conduction and radiation occur in parallel within Zone 3, so the maximum thermal resistance is limited by the magnitude of the conduction resistance. Thus, a point of diminishing returns for heat transfer reduction in Zone 3 exists with the number of external shields. For example, with N_{es} = 10 the total thermal resistance is already > 80% of its maximum value, so adding more shields may become cost-prohibitive with minor enhancements of thermal resistance. For computational simplicity, the entire network of radiation shields in Zone 3 is replaced with an equivalent emissivity ε_{Z3} in the finite-element model (Figure 3.7a). The value ε_{Z3} is iteratively tuned until the equivalent radiative resistance converges to the value calculated using Equation 3.8. For N = 7 corrugated units and N_{es} = 3, the equivalent Zone 3 emissivity is ε_{Z3} = 0.0037.

3.2.4 Radiation Heat Transfer in Zone 4

Radiative exchange between the evaporator and condenser through the exterior surfaces in Zone 4 constitutes the second main source of radiative parasitic bypass loss. The dual-stage Na-TEC modules (Figure 3.1a) are stacked in pairs, mirroring one another through a plane parallel to the condenser. Several reduced-order simplifications are incorporated in Zone 4. First, all the heat input occurs at the inner radius of the device, comprising Zone 1 (the evaporator) and part of Zone 2. An insulating cylindrical shell with

the same radius of 1.3 cm (see Figure 3.2a) is used in Zone 4 to represent the physical boundary of a central heater. This cylindrical shell acts as a re-radiating surface normal to the interior Zone 4 domain, and it is insulated in the antiparallel direction (Figure 3.7b). Next, a radiation symmetry boundary, made coplanar with the condenser bottom, is used to halve the computational domain and account for this module stacking. Furthermore, the bottom of the condenser must be in contact with a heat exchanger in a prototype device for heat rejection. However, for reduction of order this surface is considered to be isothermal and non-radiating. All Zone 4 radiation is contained within the device volume. Thus, the total bypass loss from the finite-element model is determined simply by calculating the heat output at the bottom of the condenser and subtracting from it the heat rejection from sodium condensation.

A set of concentric cylindrical shields (*cs*) of height $H = 6.2$ cm (made of vanadium) is added to Zone 4 to reduce parasitic loss (Figure 3.2a). Two bounding cylindrical shields, with radii r_a and r_b, are placed near Zone 3. A total of N_{cs} cylindrical shields, each with emissivity $\varepsilon_{cs} = \varepsilon_V = 0.21$, are evenly spaced between these two bounding shields, where each i^{th} shield has radius $r_{i,cs} = i(r_b - r_a)/N_{cs} + r_a$. To decrease the computational time added by the inclusion of these cylinders, the entire network of shields is reduced to just the two bounding shields with an equivalent emissivity ε_{Z4} on their interior concentric faces (Figure 3.7b). The view factor between each concentric face is close to unity (Figure B.1), so each individual shield interacts weakly with the bottom exterior surface of Zone 2 thereby justifying this reduced-order approach.[91]

$$\left(2/\varepsilon_{es}-1\right)\sum_{i=1}^{N_{cs}}\left(r_a/r_{i,cs}\right)^2=\left(1+\left(r_a/r_b\right)^2\right)\left(1/\varepsilon_{Z4}-1/\varepsilon_{cs}\right) \tag{3.9}$$

The equivalent emissivity ε_{Z4} is determined by equating the radiative thermal resistance of the network of shields with the resistance of the two bounding shields with emissivity ε_{Z4} on their interior faces. Setting the view factor between each shield in the network to unity, Equation 3.9 is used to calculate ε_{Z4}. For N_{cs} = 10 cylindrical shields placed between two bounding shields at r_a = 17.3 cm and r_b = 17.8 cm, the equivalent emissivity is ε_{Z4} = 0.021. Radiation in Zone 4 cannot be fully eliminated with the cylindrical shields because there is additional radiative exchange between the evaporator and the bottom of Zone 2 (see Figure 3.7b). This additional radiation path increases the enclosure temperature and leads to an increase in conduction to the second-stage electrolyte.

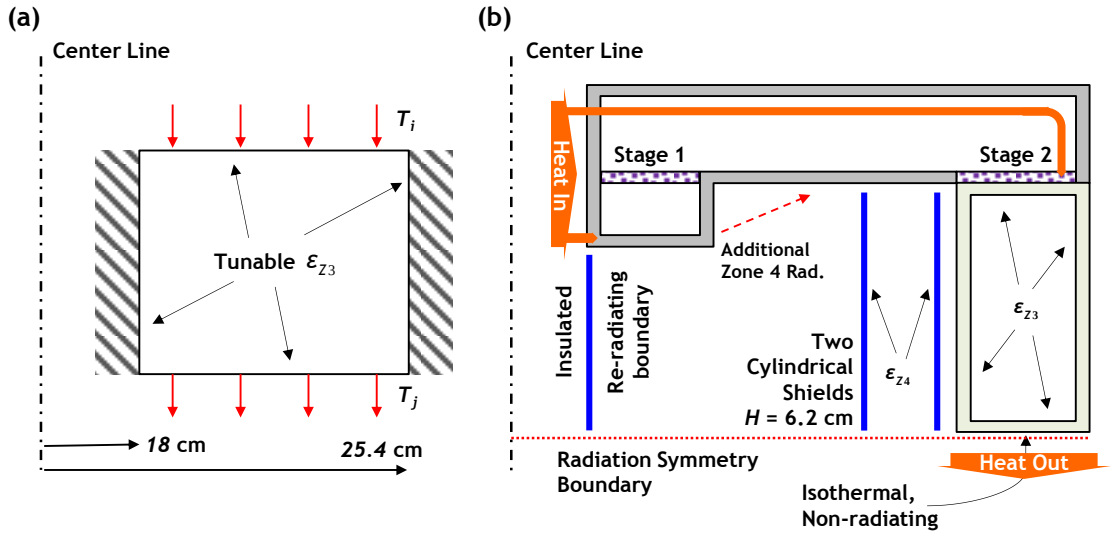

Figure 3.7 (a) Geometry used to determine the equivalent emissivity ε_{Z3} used in Zone 3. This image shows Zone 3 isolated from the structure with the corrugated walls removed, the side walls made adiabatic, and constant temperatures are applied to the top and bottom (T_i and T_j). The radiative resistance of this geometry is calculated in COMSOL, and the value of ε_{Z3} is tuned until this resistance converges to the value calculated with Equation

3.8. (b) Schematic showing the reduced-order simplifications used in Zone 3 and Zone 4 to treat radiation heat transfer. The radiation symmetry boundary is coplanar with the bottom of the condenser, so that no radiation from Zone 4 escapes to the environment and all heat output is measured at the condenser bottom.

3.3 Computing the Performance of the Dual-Stage Na-TEC Design

3.3.1 Iterative Procedure for Efficiency and Power Calculations

After implementing the reduced-order features discussed in Section 3.2, the procedure in Figure 3.8a is used to determine the expected power and efficiency for this design. In the finite-element model, initial guesses for the power in each stage (volumetric sinks in each electrolyte) are used as inputs. The outputs from the finite-element model are the volumetrically averaged temperatures of each electrolyte and the parasitic heat loss from the bottom of the condenser. These results are used as an input to the thermodynamic model to find new values for the power in each stage. This process is iterated until < 1% error for the power in each stage is achieved. This entire procedure is then repeated for each current density. It takes about 6 iterations for results to converge for j_1 = 0.1 A cm^{-2}, and about 25 iterations for results to converge for j_1 = 1.1 A cm^{-2}.

This iterative procedure was undertaken using COMSOL Multiphysics 5.3 with LiveLink for Matlab R2016a. The 2D axisymmetric reduced-order model (Figure 3.9) is built directly in COMSOL. The boundary conditions include: isothermal surfaces on the heat input face and heat output face (see Figure 3.7b); diffuse surfaces for radiation on all interior faces (16 total) and all exterior faces in Zone 4 (12 total); a symmetry plane for surface-to-surface radiation (see Figure 3.7b); volumetric power sinks for the first- and second-stage electrodes; volumetric sink/source in a thin domain in the evaporator and condenser respectively to account for phase change (refer to Section 3.2.1); and adiabatic

surfaces for the remaining exterior walls (topmost and leftmost vanadium walls and leftmost stainless steel wall). The dependent variables in this finite-element model are the temperature and surface radiosity. A free triangular mesh is built using the automatic tessellation feature in COMSOL, and mesh independence (< 1% difference in results) is established with maximum and minimum element sizes of 16.2 mm and 72.4 μm respectively. There are a total of 2028 triangular elements when the mesh is completed for this geometry, and a single simulation converges in approximately 2 minutes using a standard PARDISO solver. Once a result is obtained from this finite-element model, the iteration procedure is undertaken until the calculated power converges (< 1% error). This entire process (Figure 3.8a) is repeated for the range of first-stage current densities $0.1 \leq j_1 \leq 1.1$ A cm^{-2}. It takes approximately 8 hours to generate Figure 3.8b and Figure 3.8c using this procedure. All computations are performed in a workstation with an Intel Core i5-4570 3.2GHz processor with 8 GB RAM. It must be noted that the liquid return paths are not strictly axisymmetric, so they are not included in this finite-element model (see Figure 3.2b, Figure 3.9). Rather, the contribution to bypass heat loss from the liquid return paths is calculated analytically (see Section 3.2.2) and subsequently added to the results of this model.

An analysis of a full 3D model for the dual-stage Na-TEC would be prohibitively computationally expensive. It takes $\mathcal{O} \sim 10$ h for a single iteration of the finite-element model for a 3D geometry, and then it takes several iterations for results to converge for each value of j_1. Thus, a full 3D model simulation to compute the power curve of this dual-stage Na-TEC would require several days to complete. The reduced-order model significantly reduces the computational time while still accounting for all the relevant

physical phenomena. It is the favored technique to employ in the early stages of design for a dual-stage Na-TEC to guide the selection of materials, determine the total system size, and narrow down the operating space, all while consuming significantly fewer computational resources.

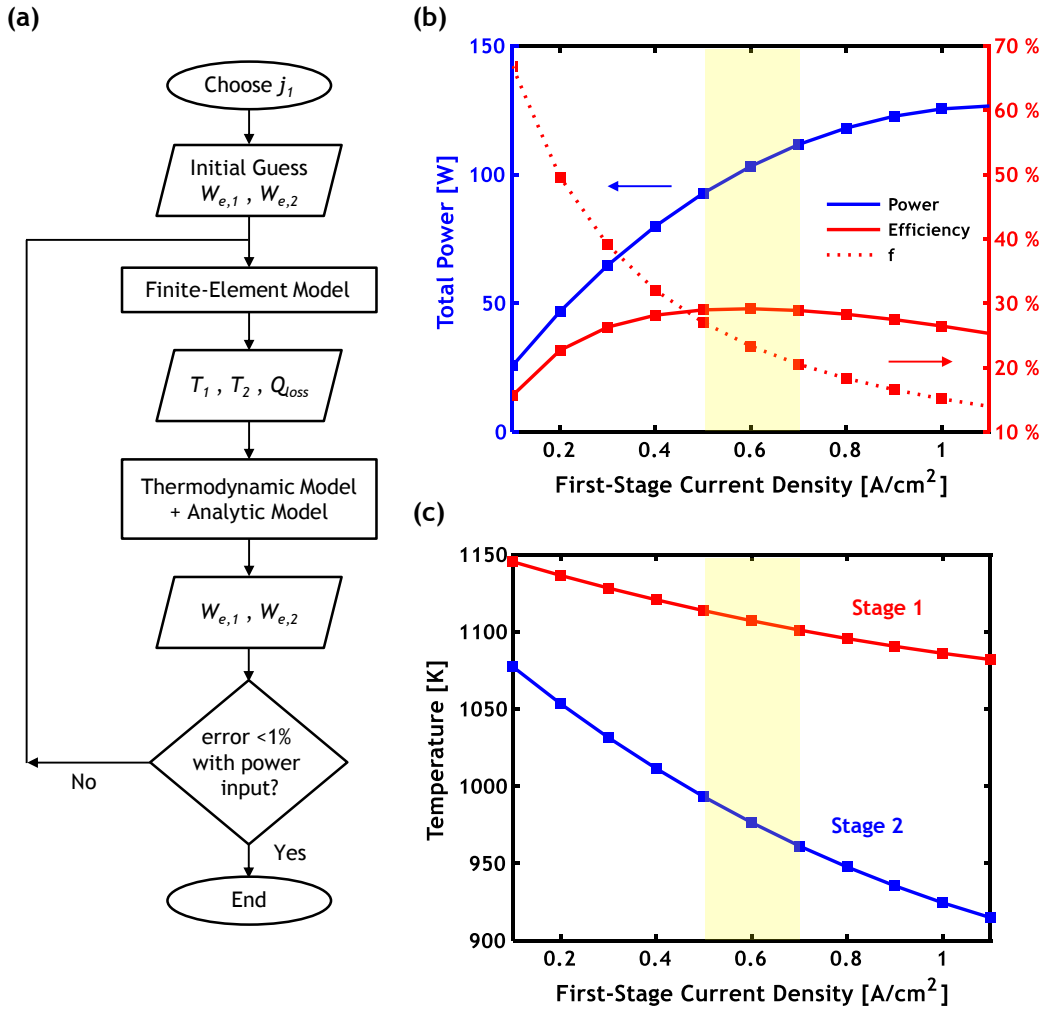

Figure 3.8 (a) Iterative procedure used to find the efficiency and power of the dual-stage Na-TEC. (b) Power produced in Stage 1 and Stage 2, thermal efficiency, and parasitic heat loss fraction f as a function of first-stage current density. (c) Volumetric average temperature of each stage as a function of first-stage current density. Suggested operation for optimal efficiency is between 0.5 A cm^{-2} < j_1 < 0.7 A cm^{-2}.

For a design with the properties listed in Table 3.1, using the thermodynamic variables listed in the caption of Figure 2.11, the efficiency and power as a function of the first-stage current density are shown in Figure 3.8b. Here, the total parasitic loss incorporates conduction loss through the liquid-return path from Figure 3.6. For this design, the maximum efficiency is ≈ 29% for 0.5 A cm^{-2} < j_1 < 0.7 A cm^{-2}, whereas the maximum power is ≈ 125 W at j_1 = 1.1 A cm^{-2}.[83] As is the case with all thermally regenerative electrochemical systems, the locations of maximum efficiency and maximum power do not coincide with one another. Most of the power (> 94%) is generated in the second stage of the device. This occurs because the first-stage open-circuit voltage is proportional to the logarithm of the pressure ratio between Zone 1 and Zone 2 (through the Nernst equation, Equation 2.1), and the Zone 2 pressure is equivalent to the saturation pressure at T_2.[77] Thus, for the range of current densities up to maximum power (*i.e.*, the load following region), the second-stage temperature is high enough that the second-stage voltage is much larger than the first-stage voltage. The parasitic heat loss fraction f is the ratio of parasitic loss to total heat input (see Section 2.2). Figure 3.8b shows that this parameter monotonically decreases with current density in the load following region, and at maximum efficiency, f ≈ 25%. Figure 3.8c shows how the volumetric average temperature in each β''-alumina electrolyte changes with current density. The difference between the two temperatures in the load following region increases as the current density, and hence power, increases. A 2D temperature distribution of this axisymmetric design is shown in Figure 3.9. Finally, it should be noted that the pressure drops ΣP_{loss} through various components in the device are not considered in this reduced-order model, including the sodium vapor pressure drop though the corrugated structure and the pressure drop along

the liquid return-path (see Section 3.2.2). Accounting for the pressure drop from all the design components will be the subject of future work (see Section 6.2).

Table 3.1 Design variables used for Figure 3.8b and Figure 3.8a

Design Variables	**Notes**
$k_{eff,1}$ = 5.8 W/m-K	t_β = 500 μm, t_{spk} = 1.5 mm, N_{seg} = 16
$k_{eff,2}$ = 3.1 W/m-K	t_β = 500 μm, t_{spk} = 1.5 mm, N_{seg} = 16
N = 7	Zone 3 corrugated units
$\varepsilon_{Z3} = 0.0037$	N = 7, N_{es} = 3, ε_{es} = 0.21, ε_{cond} = 0.25, ε_{316} = 0.6
$\varepsilon_{Z4} = 0.021$	N_{cs} = 10, ε_{cs} = 0.21 , r_a = 17.3 cm, r_b = 17.8 cm
N_{tube} = 16	Number of liquid-return paths

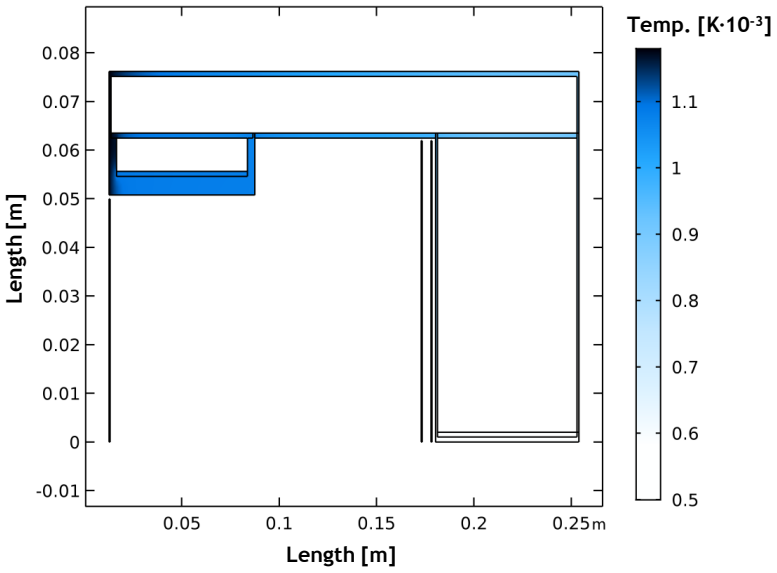

Figure 3.9 2D temperature distribution of the axisymmetric reduced-order model in COMSOL using the design variables listed in Table 3.1.

3.3.2 Cost Analysis for the Dual-Stage Na-TEC Design

The cost per unit power of this dual-stage Na-TEC design can be estimated, using previously developed methodologies, by defining the power-block (*i.e.,* Na-TEC) cost factor $K_{PB} = C_{\$}/W_e$, where $C_{\$}$ is the total cost of the Na-TEC in USD.[96] There are two contributions to the total cost of the device, the total volumetric costs C_V and areal costs C_A ($C_{\$} = C_V + C_A$). The volumetric costs account for the cost of the housing materials (vanadium and SS 316), the volumetric manufacturing cost (*i.e.,* machining labor based on a unit volume of product), and other costs that scale with the mass of sodium used in the device.[97] The areal costs account for the cost of the square β''-alumina pieces, the materials used to create the electrodes (two anodes, two cathodes), the areal manufacturing cost (*e.g.,* manufacturing of evaporation/condensation spreading structures), the heat exchanger (*i.e.,* all dry cooling equipment necessary to cover the external condenser surface area), and other costs that may scale with the area of the device.[97]

The most expensive component of the total volumetric costs C_V is the price for the vanadium and SS 316 housing materials, which is estimated from 2018 average commodity prices.[98] This cost lies between \$56 and \$104 using the average prices for the two housing materials and a reasonable ± 25% variation. For the cost of sodium, a conservative estimate of \$0.5 to \$11 is used by assuming that the evaporator volume (Zone 1) and the total internal volume (Zones 1-3) are filled with sodium, respectively. The price of the β''-alumina electrolyte has historically dominated the material component to the areal costs C_A of the Na-TEC.[99] A price of \$30/m^2 (Ceramatec Inc., 2017) can be assumed for the square planar pieces of β''-alumina used in this design (see Figure 3.1b). For uniformity in cost calculations, the electrodes in both stages are assumed to be made of molybdenum and

the cost (neglecting preparation expenses) is determined using the average molybdenum commodity price for 10 μm sputtered electrodes.[98] The heat exchanger is comprised of a set of 81 mm diameter pin fins attached to the condenser, which allow for natural convection, with a nominal cost of about \$40/m^2.[100] Finally, all remaining manufacturing costs are addressed using a mark-up factor: 25% of the combined housing and sodium costs for the volumetric manufacturing; and 30% of the combined β''-alumina, molybdenum electrode, and heat exchanger costs for the areal manufacturing. A Monte Carlo analysis was performed to estimate an average K_{PB} = \$1.01/W for this dual-stage Na-TEC.[101] This compares well to a previous detailed study of the capital costs for a single-stage Na-TEC (*i.e.,* AMTEC), which reports an estimate of \$0.35/W < K_{PB} < \$0.6/W.[99] Cost analyses for various applications using a Na-TEC power block have also been previously considered, including liquid metal nuclear reactors [102], solar powered space systems with integrated thermal storage [103], and grid-level concentrated solar power [101].

3.4 Summary

In this chapter, the heat transfer within a quasi-axisymmetric dual-stage Na-TEC design has been analyzed with a reduced-order thermal model. Several simplifying assumptions have been made to decrease the computational time, making the model amenable for rapid design iterations while maintaining acceptable accuracy. Heat conduction is calculated using effective thermal conductivities, while internal radiation from the β''-alumina electrolyte to the condenser is considered using a network of linear radiation shields. In the exterior of the device, direct radiative exchange between the evaporator and condenser is limited by a network of cylindrical radiation shields. The

thermal analysis is simplified by taking advantage of symmetry and using an equivalent emissivity between these bounding cylindrical shields. To estimate the parasitic loss through the liquid-return path linking the evaporator and condenser, an analytical model coupling conduction and advection is developed. Using an iterative approach in COMSOL that incorporates these reduced-order features, the maximum efficiency for this design was found to be ≈ 29%, which requires operation between 0.5 A cm^{-2} < j_1 < 0.7 A cm^{-2}. The maximum power was found to be ≈ 125 W when operating at j_1 = 1.1 A cm^{-2}. A brief cost analysis shows that electricity can be produced at a cost of $1.01/W with this dual-stage Na-TEC design. This reduced-order modeling approach can be used to analyze the thermal performance in the early stages of design for a dual-stage Na-TEC, guide the selection of materials, and determine the total system size, all while consuming minimal computational time.

Much of the content in this chapter was published in *Applied Thermal Engineering*, Vol. 145, A. Limia *et. al.*, "Thermal modeling and efficiency of a dual-stage sodium heat engine", 603-609, Copyright Elsevier (2018)

CHAPTER 4. LIQUID SODIUM BREAKTHROUGH PRESSURE EXPERIMENT

When designing capillary structures for pumping, it is necessary to know the maximum pressure head that can be generated. For a liquid suspended in vapor, the maximum pressure difference across the interface is described by the Laplace equation $P_L = 2K_{12}\sigma_{lv}$, where the curvature K_{12} is defined by orthogonal radii of curvature.[104] When a third phase is present (*i.e.* a solid surface), the Laplace pressure is a function of the surface tension σ_{lv}, the characteristic pore diameter d_p, and the contact angle θ_{ca} between the liquid and the solid. The Young-Dupree equation $\sigma_{lv} \cos \theta_{ca} = \sigma_{sv} - \sigma_{ls}$ relates the contact angle of a sessile drop on a flat solid surface (neglecting gravitational forces) to the force balance of the surface energies along the triple-phase interface.[105] When $\theta_{ca} < 90°$, the surface is wetting (*i.e.* high energy surface), and when $\theta_{ca} > 90°$ the surface is non-wetting (*i.e.* low energy surface). A liquid will not penetrate a non-wetting capillary because the solid-surface adhesion forces will repel the liquid.[65] To measure the breakthrough pressure required to penetrate a non-wetting capillary, two different approaches are usually taken: (1) displacing a wetting fluid inside a saturated porous structure with a gas and detecting the emerging bubbles, or (2) injecting a non-wetting fluid directly into an evacuated porous structure and measuring the penetration.[106] The latter measurement technique has been successfully attempted with mercury by detecting breakthrough once the pressurized mercury starts flowing and short-circuits a copper wire downstream.[107] Numerous techniques are available to measure the flow of a liquid metal, the most common being a permanent magnet flowmeter, which takes advantage of magnetic induction.[108, 109]

However, many of these techniques are inaccurate at very low speeds, and are unnecessarily complex when the simple electric activation of wires works adequately for flowing metals. In this chapter, an experiment designed to measure the temperature dependent breakthrough pressure of liquid sodium on a stainless steel porous sample is discussed. The experiment (following approach #2 from above) involves the incremental pressurization of sodium until it penetrates through the porous sample. With the velocity data from this experiment, the permeability of the stainless steel porous structure can also be calculated. Section 4.1 describes the design and procedure of this breakthrough pressure experiment. The measured breakthrough pressure and permeability measurements from various experimental runs are analyzed Section 4.2 and Section 4.3 respectively. Finally, Section 4.4 summarizes the key findings in this chapter, with the aim of answering the thesis question: *What temperature-dependent interfacial pressures can be generated between a stainless-steel porous structure and liquid sodium?*

4.1 Breakthrough Pressure Experiment Design and Procedure

4.1.1 Design and Assembly of the Breakthrough Pressure Experiment

Candidate materials for the breakthrough experiment must be non-wetting to liquid sodium at the experimental temperatures. A comprehensive study of the temperature-dependent contact angle of sessile liquid sodium drops on various metallic surfaces was undertaken in 1955.[110] Sodium flowed through an orifice to produce approximately 1 cm diameter drops on polished, degassed surfaces in an argon environment, and the contact angle was optically measured. For stainless steels, low-carbon compositions were shown to be most readily wetted. The temperature-dependent contact angle of sodium on stainless

steel 18-8 (SS 18-8, carbon composition < 0.08%) is shown in Figure 4.1a. Liquid sodium is non-wetting to SS 18-8 up to a temperature of 410 °C, beyond which θ_{ca} is less than 90° and the sodium transitions to a wetting regime. This contact angle data can be fitted to an *arctan* function with two horizontal asymptotes (see Figure 4.1a) using least-squares regression. In the non-wetting regime, this regression curve fits the data very well ($R^2 > 0.98$) and predicts a contact angle of $\theta_{ca} = 160°$ near the sodium melting point (97 °C). This regression curve also fits the limited wetting regime data well. However, at much higher temperatures it predicts a slowly decreasing contact angle down to $\theta_{ca} = 50°$ near the boiling point of sodium (880 °C). In contrast, previous measurements for sodium on SS 304 show almost complete spreading ($\theta_{ca} < 5°$) at temperatures above 550 °C.[111] This difference in sodium contact angle measurements in the wetting regime can be explained by the condition of the surface oxide layer, whose dissolution significantly reduces the contact angle above a critical temperature.[90] Experiments on oxide-free stainless steels have demonstrated wetting at much lower temperatures, underscoring the significance of the oxide film on the contact angle behavior.[110, 112] A commercially available SS 316L porous material from GKN Sinter Metals, with an effective pore diameter 0.1 μm < d_p < 4.14 μm and a porosity φ = 25%, is used for the breakthrough pressure experiments. Contact angle data for SS 316L could not be found in literature, so the contact angle data for SS 18-8 is used as a proxy; the wetting properties of SS 316L are assumed to be similar to those of SS 18-8 due to its low carbon composition (< 0.03%) and its adequate resistance to sodium corrosion above the wetting transition temperature.[113]

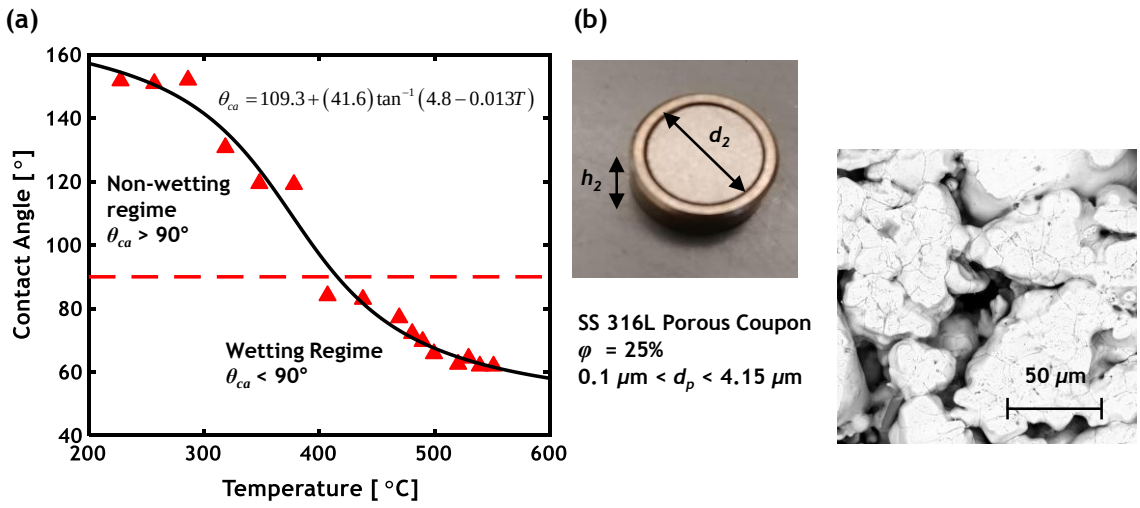

Figure 4.1 (a) Contact angle of liquid sodium on SS 18-8, adapted from ref. [110]. An *arctan* function is fitted to the data using least-squares regression. (b) SEM image of the experimental coupon.

To create an experimental coupon (Figure 4.1b), the SS 316L porous samples are first cut into thin cylinders using electric discharge machining (EDM). These machined SS 316L samples are then press-fit into SS 316 tubes with smaller inner diameters. To accomplish this, the SS 316 tubes are thermally expanded at 425 °C to provide space for the machined samples to fit. The SS 316L samples are then immediately hammered into position while the cylinder is still hot. A thick (0.5 mm) aluminum sheet is used as a buffer between the hammer and the SS 316L coupon to prevent damage to the porous surface; no residue aluminum was observed. Since the coefficient of thermal expansion (CTE) between the SS 316 tube and the SS 316L porous sample is practically equivalent, a tight fit persists throughout the experiment as temperature rises. The experimental coupon is then mounted between two SS 316 flanges through which the sodium will flow during the experiment (Figure 4.2a). These flanges are placed inside a small muffle furnace with thermocouple

and electrical feedthroughs for data gathering (Figure 4.2b). A separate SS 316 tube welded to the bottom flange is connected to a larger tube outside the furnace (see Figure 4.2b) where sodium is inserted, melted, and allowed to flow up to the experimental coupon. This welded tube acts as a liquid feedthrough while the flanges are inside the furnace. The large tube is also connected to a regulated argon tank for pressurization during the experiment. As sodium flows up to the experimental coupon, a solid-liquid-vapor interface is formed on the porous surface that impedes the further flow of sodium (*i.e.,* it is non-wetting). In the top flange, SS 316 electrodes are placed along the flow path to detect sodium breakthrough and measure the flow speed. These electrodes are attached to the top flange using Omegabond 600 high-temperature cement, which is replaced every 3-5 runs due to mechanical degradation. They are electrically isolated from the flange and are only exposed to the flow path (see Figure 4.2a). These electrodes are connected in parallel to a 3V battery so that an electric circuit is established when flowing sodium comes into contact with them. The entire experiment is assembled inside an argon glovebox to limit the oxidation of sodium.

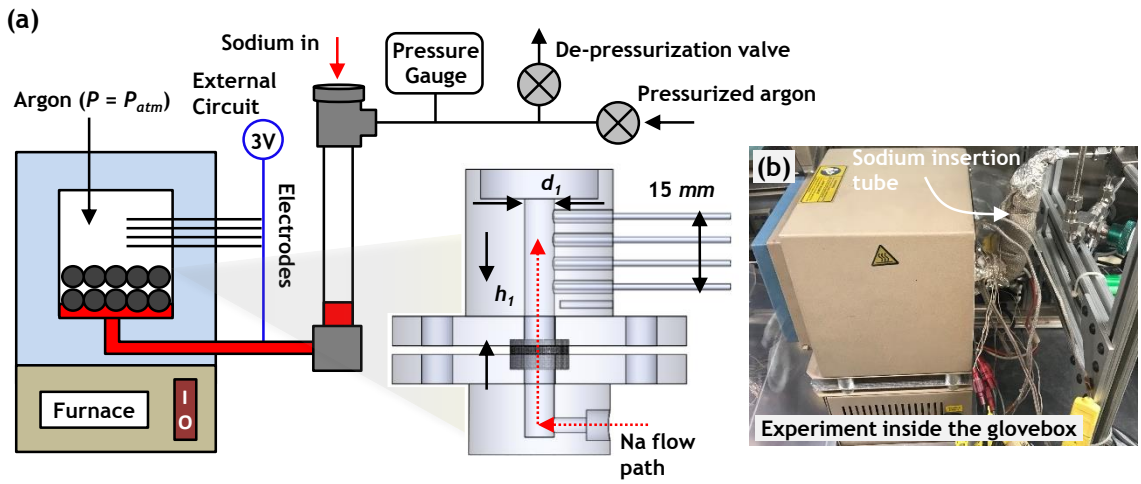

Figure 4.2 (a) Schematic of the experimental assembly. The flanges that compress the experimental coupon are enlarged. (b) Picture of the experimental assembly inside an argon glovebox. The large tube where sodium is inserted is shown feeding into a muffle furnace.

4.1.2 Breakthrough Pressure Experiment Procedure

Once the assembly is complete, the experimental procedure comprises five steps:

1. Inside the argon glovebox, high purity solid sodium cubes (Sigma Aldrich 99.9%) are dried of mineral oil and stripped of their native oxide layers (Na_2O, NaOH) by gently cutting their six faces with a knife until they are lustrous.[114] 1.65 *g* of sodium are added to the large tubing outside the furnace (see Figure 4.2b).
2. The large outside tube is heated (> 97 °C) to melt the sodium. The molten sodium forms a liquid plug by filling up the entire tube volume up to the inlet of the experimental coupon (see Figure 4.2a). Sodium is non-wetting to the SS 316L porous sample at low temperatures, so the flow is impeded at the inlet and a solid-liquid-vapor interface (in argon) is established. The temperature of the furnace is then increased to the desired value, while the temperatures of both flanges are

individually monitored with thermocouples, one above the experimental coupon and one below it.

3. Once the temperatures have reached steady-state, the argon pressure opposite the liquid plug is incrementally increased using a regulator. Small ΔP_{inc} = 5 kPa pressure increments are used so that quasi-static equilibrium is approximately maintained while pressure is increasing. A specific wait time t_{wait} is enforced between each pressure increment.
4. At a certain pressure (while the experimenter waits to initiate the next pressure increment), the solid-liquid-vapor interfacial force cannot maintain equilibrium and sodium will flow through the porous structure. This is the breakthrough pressure. Flow is established when the sodium contacts the cemented electrodes in the top flange and activates a 3V signal. Additionally, the flow speed is determined by dividing the distance between successive electrodes by the difference in their activation times.
5. Once all electrodes have been activated, the experiment is passively cooled down to room temperature and subsequently disassembled. Solid sodium is then scraped off all the experiment components. Afterwards, each component is rinsed in a pool of methanol to remove the remaining traces of sodium via chemical reaction, producing sodium methoxide and hydrogen gas ($2Na + 2CH_3OH \rightarrow 2CH_3ONa + H_2$). The remaining CH_3ONa is then carefully rinsed off. Another experiment is now ready to commence using a new experimental coupon.

The wait time between pressure increments t_{wait} is composed of two contributions (Figure 4.3), the amount of time it takes for the liquid sodium to fully penetrate through

the porous sample in the axial direction, and the time it takes the sodium to reach the first electrode after traversing through the porous sample. The former term depends on the minimum pressure difference allowed after breakthrough occurs (equivalent to ΔP_{inc}), and it is based on the Washburn equation for flow in capillaries while neglecting inertia.[115] The latter term is defined as a function of the linear distance between the porous sample outlet and the bottom of the first electrode, and the different diameters within the flow path. These dimensions are defined in Figure 4.1b and Figure 4.2a. This wait time equation assumes fully developed flow and negligible hydrodynamic minor-losses across the flanges. It also assumes that the porous sample is completely saturated with liquid sodium after breakthrough occurs (*i.e.,* uniform flow in the porous sample cross-section area). Within the experimental coupon, the velocity corresponding to the porous sample is the Darcy velocity u_D (*i.e.,* volume averaged velocity). The required wait time is calculated from an experiment *a posteriori*, so typically the largest wait time from a previous run is conservatively applied to the next run. As discussed in Appendix C, the required wait time, determined after the experiment, is used to find the uncertainty in the breakthrough pressure measurement.

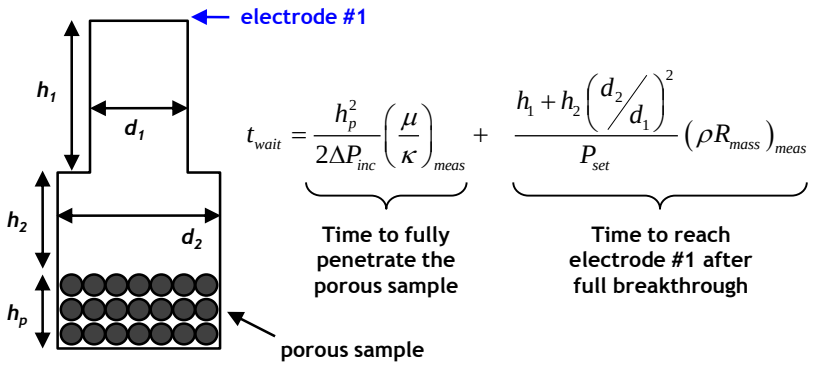

Figure 4.3 Schematic of the internal flow path between the porous sample inlet and electrode #1. The equation used to determine the wait time comprises two terms: the time it takes for sodium to fully penetrate the porous sample, and the time it takes to reach electrode #1 after flowing past the porous sample.

4.2 Breakthrough Pressure Results

4.2.1 Thermodynamic Model for Breakthrough Pressure

The breakthrough pressure for an arbitrary geometry is found by equating the change in surface energy to the work performed by the applied pressure in perturbing the interface (Equation 4.1).[116] At the location of the smallest cross-section flow area, an infinitesimal displacement of the interface produces a negligible change in the liquid-vapor interfacial area A_{lv}. Therefore, the differential elements defined in Equation 4.1 are applicable. Substituting the Young-Dupree equation (Equation 4.2), a general breakthrough pressure equation (Equation 4.3) is obtained as a function of the surface tension, the liquid-vapor L_{lv} and liquid-solid L_{ls} interface perimeter lengths, the contact angle, and the projected area of the interface A_p (bounded by the perimeter $L_{lv} + L_{ls}$).

$$P_L dV = \sigma_{lv} dA_{lv} + \sigma_{ls} dA_{ls} + \sigma_{sv} dA_{sv} \begin{cases} dV_0 = A_p \delta s \\ dA_{lv} = L_{lv} \delta s \\ dA_{ls} = -dA_{ls} = L_{ls} \delta s \end{cases} \tag{4.1}$$

$$\sigma_{sv} = \sigma_{sv} + \sigma_{sv} cos\theta_{ca} \tag{4.2}$$

$$P_L = \sigma_{lv} \left(\frac{L_{lv} - L_{ls} cos\theta_{ca}}{A_p} \right) = \sigma_{lv} \left(\frac{L_p}{A_p} \right) \tag{4.3}$$

Equation 4.3 assumes that the mean curvature of the interfacial area A_{lv} is constant when the interface is fixed, signifying that the Laplace pressure P_L is uniform over this area.[117] This is a valid assumption when gravitational effects are negligible (*i.e.*, small *Bo*). Two optimization steps are required to find the breakthrough pressure for a certain geometry. First, within a single pore the location of maximum pressure in the axial direction is determined, which corresponds to the smallest cross-section flow area (*i.e.*, largest interface curvature). At this axial location, the ratio of the parameter L_p to the projected interface area A_p is minimized (*i.e.*, the minimum of Equation 4.3).[118] These successive limits correspond to the lowest pressure needed for breakthrough at the location of highest interfacial curvature within a single pore.

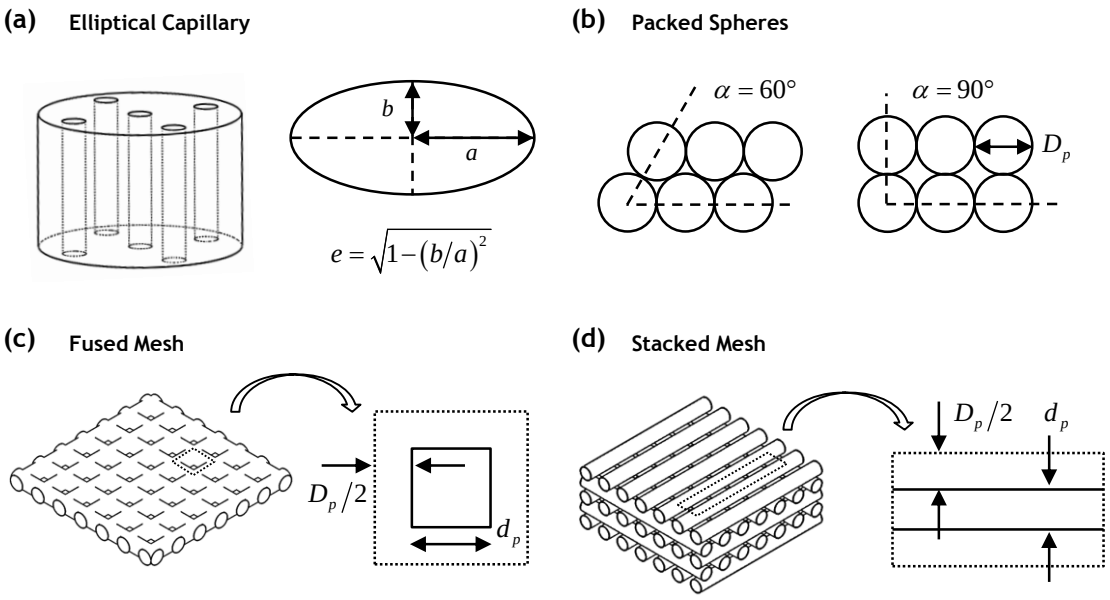

Figure 4.4 Schematics of the various geometric models used for the breakthrough pressure analysis: (a) elliptical capillary tubes, (b) packed spheres, (c) fused mesh, (d) stacked mesh. The pore and solid diameters for the packed spheres, the fused mesh, and the stacked mesh are defined.

Using Equation 4.3, the breakthrough pressures for various geometries (Figure 4.4), representing porous structures, are derived in order to compare against the experimental data. Breakthrough is assumed to be limited by the largest pores, so d_p = 4.14 μm is used for all breakthrough pressure calculations. The simplest geometry to consider is a set of straight capillary tubes, where each tube can be represented as an elliptical cylinder with major axis *a* and minor axis *b* (Figure 4.4a). For an elliptical capillary, the entire interface perimeter is in contact with the solid, so L_{lv} = 0 and the breakthrough pressure is given by Equation 4.4.

$$P_L = -\sigma_{lv} cos\theta_{ca} \frac{(a+b)}{ab} \sum_{n=0}^{\infty} \binom{0.5}{n} \left(\frac{a-b}{a+b}\right)^{2n} \tag{4.4}$$

The minor axis of the ellipse is set to $b = d_p/2$ to coincide with the porous sample. The breakthrough pressure for a circular cylinder (Equation 4.5) is a special case of the elliptical cylinder with an eccentricity $e = 0$. In the limit of $e \rightarrow 1$, the breakthrough pressure is given by Equation 4.6. If the capillary is instead idealized as a very long rectangular fissure of width d_p (that is, $2b$), the breakthrough pressure is approximated by Equation 4.7.[116] The ratio L_{ls}/A_p of an ellipse in the limit of $e \rightarrow 1$ is a factor of $4/\pi$ larger than the ratio for a long, thin rectangular fissure of width $2b$; this is the factor of difference between Equation 4.6 and Equation 4.7.

$$P_L = \frac{-4\sigma_{lv} cos\,\theta_{ca}}{d_p} \tag{4.5}$$

$$P_L = \frac{-2\sigma_{lv} cos\,\theta_{ca}}{d_p}\left(\frac{4}{\pi}\right) \tag{4.6}$$

$$P_L = \frac{-2\sigma_{lv} cos\,\theta_{ca}}{d_p} \tag{4.7}$$

Aside from straight capillaries, several 3D geometries are also considered. Two packed sphere models (Figure 4.4b) are examined: rectangular packed spheres ($\alpha = 90°$, $\varphi = 48\%$) and hexagonal packed spheres ($\alpha = 60°$, $\varphi = 26\%$). Two models for porous samples consisting of solid cylinders are also examined: the fused mesh (Figure 4.4c) and the stacked mesh (Figure 4.4d), both with the nominal porous sample porosity $\varphi = 25\%$. For packed spheres with $90° \leq \alpha < 60°$, Equation 4.8 and Equation 4.9 describe the interface located at the axial center of the sphere (corresponding to the hemisphere), which is the minimum axial cross-section area.[118] The solid diameter D_p of these packed spheres can

be related to the pore diameter d_p and the porosity through $D_p = 3d_p(1-\varphi)/(2\varphi)$.[119] When the packing angle α is fixed and the contact angle is known, the breakthrough pressure is found by minimizing L_p/A_p (*i.e.*, the minimization of Equation 4.3) with the angle ψ (see Figure 4.5). Note that since the normal vector to the surface of a sphere continually changes with angle ψ, the cross-sectional flow area in Figure 4.5 cannot be filled completely with liquid unless $\theta_{ca} \leq 90°$ (*i.e.*, this porous structure cannot be 100% saturated with a non-wetting liquid).

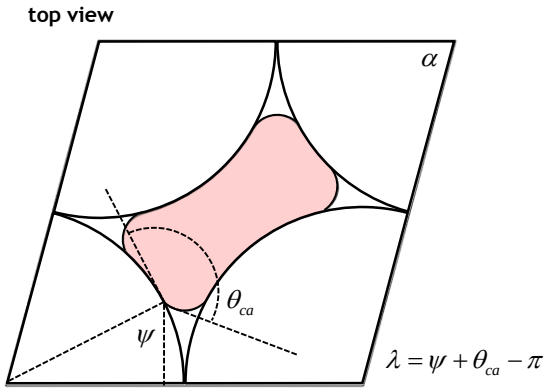

Figure 4.5 Minimum liquid cross-sectional area (red color) at the center of packed spheres with packing angle α (image depicts the sphere hemispheres). Adapted from ref. [118]

$$L_p = 4D_p\left(\lambda\left(\frac{1-sin\psi}{sin\lambda}\right)-cos\theta_{ca}\left(\psi-\pi/4\right)\right) \tag{4.8}$$

$$A_p = D_p^2\left(\begin{array}{c} sin\alpha+\pi/4-cot\psi-cot\lambda\left(1-sin\psi\right)^2+ \\ cot\lambda\left(1-sin\psi\right)^2-\psi+\lambda\left(\frac{1-sin\psi}{sin\lambda}\right)^2 \end{array}\right) \tag{4.9}$$

For the special case of packed spheres with $\alpha = 60°$ (hexagonal packing), Equation 4.10 and Equation 4.11 apply instead.[118]

$$L_p = 6D_p\left(\lambda\left(\frac{1-sin\psi}{sin\lambda}\right)-cos\theta_{ca}\left(\psi-\pi/3\right)\right) \tag{4.10}$$

$$A_p = \frac{3}{2}D_p^2\left(\begin{array}{c}\sqrt{3}/3+\pi/3-cot\psi-cot\lambda\left(1-sin\psi\right)^2+\\ cot\lambda\left(1-sin\psi\right)^2-\psi+\lambda\left(\frac{1-sin\psi}{sin\lambda}\right)^2\end{array}\right) \tag{4.11}$$

For the fused mesh, the minimum flow cross-section area is a square at the cylinder midpoint, corresponding to a semicylinder (see Figure 4.4c). The hydraulic diameter of this square is equivalent to its width, which is set equal to the pore diameter $L = d_p$. The solid diameter of these cylinders is found by solving $(1 - \varphi)(d_p+D_p)^2D_p = 2(d_p+D_p)(\pi D_p^2/4) - 2D_p^3/3$, which relates the porosity to the solid/vapor volumes in the unit cell. For $\varphi = 25\%$, this equation yields $D_p = 8.2\ \mu$m for the solid diameter of the fused mesh cylinders. For a general cross-section area represented by a parallelogram (Figure 4.6), Equation 4.12, Equation 4.13, and Equation 4.14 describe the interface. This cross-section parallelogram corresponds to the fused mesh model when $\alpha = \alpha_o = 90°$. Note that unlike the packed sphere geometry, the normal vector at the sides of this parallelogram is fixed. Thus, there is a minimum liquid contact angle below which the corners of the parallelogram flow area in Figure 4.6 will be filled completely with liquid: $\theta_{ca} \leq (\pi + \alpha)/2$ for the acute corner and $\theta_{ca} \leq (2\pi - \alpha)/2$ for the obtuse corner.

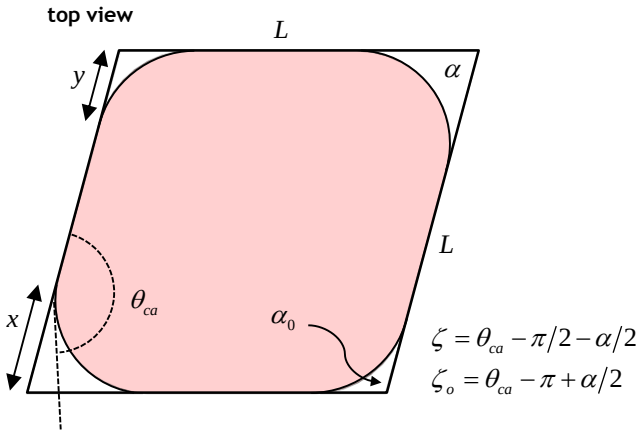

Figure 4.6 A general flow cross-section area represented by a parallelogram. The red area represents the liquid cross section.

$$L_{lv} = 4\left((\zeta x)\frac{sin\left(\alpha/2\right)}{sin^2\beta} + (\zeta_o y)\frac{sin\left(\alpha_o/2\right)}{sin^2\beta_o} \right) \tag{4.12}$$

$$L_p = L_{lv} - 4(l - x - y)cos\theta_{ca} \tag{4.13}$$

$$A_p = L^2 sin\alpha + x^2\left(\frac{sin^2\left(\alpha/2\right)}{sin^2\zeta}\left(2\zeta - sin\left(2\zeta\right)\right) - sin\alpha \right) + y^2\left(\frac{sin^2\left(\alpha_o/2\right)}{sin^2\zeta_o}\left(2\zeta_o - sin\left(2\zeta_o\right)\right) - sin\alpha_o \right) \tag{4.14}$$

For the stacked mesh, the minimum flow area is a rectangle at the cylinder midpoint, corresponding to a semicylinder (see Figure 4.4d). The distance between parallel cylinders is set equal to d_p, and the solid diameter is found by solving $D_p = (1/\varphi - 1)\, dp$. For φ = 25%, this equation yields D_p = 12.4 μm for the solid diameter of the stacked mesh

cylinders. The cross-section area for the stacked mesh is idealized as a long rectangular fissure, so the breakthrough pressure is determined using Equation 4.7.

4.2.2 Analysis of Breakthrough Pressure Data

The breakthrough pressure as a function of temperature is plotted in Figure 4.7, and the data are tabulated in Table C1. As expected, the breakthrough pressure is larger at lower temperatures where the contact angle and liquid-vapor surface tension are highest, and it monotonically decreases at higher temperatures. The highest temperature experiment was conducted at 407 ± 4 °C with a breakthrough pressure of 3.3 ± 2 kPa. Extrapolation is needed to estimate the wetting transition temperature because this experiment is not designed to work in the wetting regime. Following the method discussed in Appendix C, this temperature is estimated to be 411.6 ± 5.3 °C. Several sources of uncertainty for these measurements are described in Appendix C. Most importantly, this experiment is very sensitive to the wait time t_{wait} discussed in Section 4.1.2. If t_{wait} between pressure increments is too small, the measured breakthrough pressure will be artificially larger. Although great care was taken to use a conservative t_{wait} during each experiment, the data error bars attest to the experimental sensitivity to this parameter. The data in Figure 4.7 also show a significant variation in the breakthrough pressure at nearly isothermal conditions. For example, around 270 °C the measured breakthrough pressure varies by 40 kPa (excluding the error bars). The factors that lead to this variability are discussed later in this section.

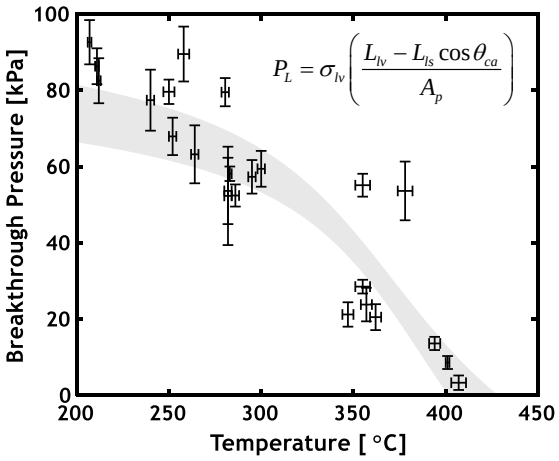

Figure 4.7 Breakthrough pressure data as a function of temperature. The gray band represents the 95% confidence interval for this data using a least-squares regression based on the breakthrough pressure equation in the inset (Equation 4.3).

The experimental data can be compared to breakthrough pressure models of the simple geometries introduced in Section 4.2.1. Using the temperature dependent surface tension of sodium [120] and the regression curve for the contact angle (see Figure 4.1a), the breakthrough pressure curves for these various geometries are plotted in Figure 4.8a (3D models) and Figure 4.8b (capillary models). It was initially assumed that the hexagonally packed sphere geometry would best predict the breakthrough pressure, since its porosity is comparable to the nominal value of 25% for the porous sample. However, it actually overpredicts the data more than the other 3D models in Figure 4.8a. The rectangular packed sphere model captures the data much better, especially at higher temperatures, but its geometric porosity of 48% differs significantly from the nominal value of 25%. Among the 3D models, the stacked mesh best predicts the data but it is the least physically compatible with the actual pore structure (see Figure 4.1b). For the capillary model, as e → 1 (*i.e.*, a high eccentricity ellipse resembles a long rectangle) the data are more accurately predicted. This coincides with the stacked mesh model, whose

cross-section area is precisely a rectangle (the breakthrough pressures differ by a factor of $4/\pi$, see Section 4.2.1). However, up to the highest values of eccentricity that can reasonably describe some of the pores in the sample (liberally taken as $e \leq 0.95$ based on Figure 4.1b), the capillary model agrees poorly with the measured data. Indeed, none of these geometric models fully capture the data throughout the entire temperature range. Furthermore, the geometries that most resemble the porous sample physical structure (*i.e.*, rectangular packed spheres, fused mesh, and low eccentricity capillary tubes) significantly overpredict the breakthrough pressure. These discrepancies notwithstanding, all the curves estimate the wetting transition temperature to be 415 ± 1 °C, which coincides well with the experimental extrapolation (411.6 ± 5.3 °C). This justifies the use of the regression curve for SS 18-8 (Figure 4.1a) to estimate the contact angle of sodium on SS 316L, at least at moderate temperatures up to the wetting transition.

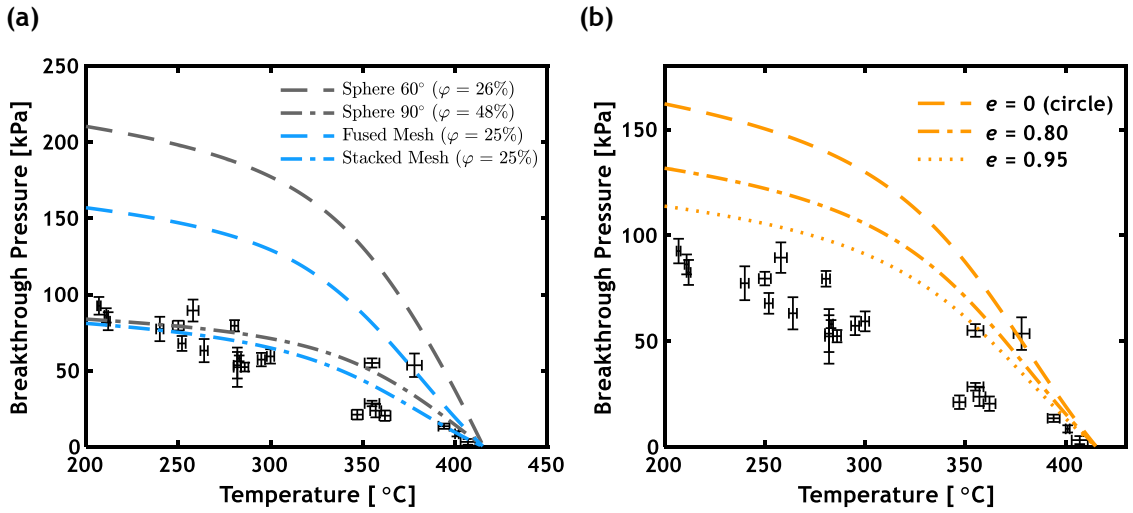

Figure 4.8 (a) Four lines corresponding to the breakthrough pressure for 3D models (packed spheres with $\alpha = 90°$, packed spheres with $\alpha = 60°$, fused mesh, stacked mesh) are plotted with the breakthrough pressure data. (b) Three lines corresponding to the breakthrough pressure for a capillary model (elliptical cylinder with three different eccentricities) are plotted with the breakthrough pressure data.

Many factors influence the low magnitude of the breakthrough pressure data, and the variability in nearly isothermal measurements. The thermal press fit (see Section 4.1.1) may insufficiently compresses the porous sample within the SS 316 tube, leaving larger pores at the boundary between the two. The tolerance for the EDM process used to cut the porous samples, and the hammering process by which the experimental coupons are assembled both lead to variability amongst experiments, especially since the experimental coupon is replaced for every run. There could also be a slight CTE mismatch between the SS 316 tube and the porous sample which increases the effective pore diameter at the boundary. If there are larger pores at the boundary, sodium would flow at lower measured breakthrough pressures compared to the geometric models discussed previously, and there would be a substantial variability observed in the data. After the wait time parameter, this was identified as the most influential factor on the measured breakthrough data.

The physical condition of the porous sample surface is also very important. Adsorbed gas species (oxygen, hydrogen, nitrogen) on the surface will artificially shift the spreading of sodium to higher temperatures, which manifests in a large contact angle hysteresis of sodium upon cooling hot surfaces.[110] This wetting irreversibility suggests that desorption of gases from the surface enhances the effective solid-liquid interfacial contact. Furthermore, adsorbed gases and dissolved impurities in the liquid sodium (*e.g.*, surfactants) also affect the liquid-vapor surface tension, which then modifies the contact angle.[121] As discussed in Section 4.1.1, the surface oxide condition has the largest impact on the contact angle. To normalize the porous surface condition, all coupons were sonicated in water, isopropyl alcohol, and acetone to remove impurities (like machining oils) prior to mounting them on the flanges. However, the samples were not degassed at

high temperature prior to loading the experiment with sodium. Consequently, although major surface impurities were removed, adsorbed gas species may have been present on the surface at varying concentrations across different runs. Corrosion by liquid sodium may also affect the breakthrough pressure. For stainless steels, the corrosion caused by liquid sodium is influenced by several interrelated factors. Among these, the corrosion products formed by oxygen impurities are particularly damaging.[113] Oxides of nickel, iron, and chromium on the stainless steel surface can be reduced by sodium to form Na_2O, thereby affecting the passivity of the stainless steel. These alloying elements are also highly soluble in liquid sodium, promoting dissolution corrosion at very high temperatures.[122] In another corrosion mechanism, carbon transfer amongst dissimilar materials or in non-isothermal components may form carbide precipitates.[123] These corrosion processes compromise the surface oxide layer and skew the breakthrough pressure results, but they are mild at the moderate temperatures (< 420 °C) in these experiments. Finally, the oxidation of the SS 316 and SS 316L components due to the non-negligible, albeit small, concentrations of O_2 (< 100 ppm) and H_2O (< 20 ppm) in the glovebox may also contribute to the data variability, especially after repeated runs with the same assembly components (the experimental coupon is new for every run).

4.3 Permeability Results

This experiment can also be used to measure the permeability of the porous sample. For momentum conservation, the one-dimensional Darcy law (Equation 4.15) applies to viscous flow with a small velocity (*i.e.*, $Re_{\sqrt{\kappa}} < 1$) in an isotropic porous material, with a characteristic length $L >> \sqrt{\kappa}$.[124] The permeability κ is inversely proportional to the axial

pressure gradient and proportional to both the temperature-dependent fluid viscosity μ and the unidirectional Darcy velocity u_D. The absolute fluid velocity is related to the Darcy velocity via the Dupuit-Forchheimer relationship $u_D = \varphi u$.[125] The sodium flow velocity is determined by dividing the distance between successive activated electrodes by the difference in their activation times. The Darcy velocity within the experimental coupon is then approximated by applying continuity between the experimental coupon and the top flange. The velocity data are tabulated in Table C1, and the calculation of the velocity uncertainty is discussed in Appendix C.

$$u_D = -\frac{\kappa}{\mu}\left(\frac{\partial P}{\partial x}\right) \tag{4.15}$$

In the assembly, the inlet/outlet diameters of the SS 316L porous sample are different because the experimental coupon is placed on a counterbore in the bottom flange (see Figure 4.2a), which makes the inlet diameter < d_2 (outlet diameter = d_2, see Figure 4.3). To account for this difference in inlet/outlet diameters, a "spreading" mass transfer resistance is used to estimate the permeability. This is analogous to methods used to determine the spreading thermal resistance in cylindrical semiconductor devices.[126] In lieu of an analytical solution, a COMSOL model is used to find the spreading resistance to viscous flow in an axisymmetric cylinder that represents the porous sample (Figure 4.9a). Dirichlet boundary conditions are applied to the inlet and outlet faces: the inlet pressure is equal to the breakthrough pressure while the outlet has an applied pressure of zero. Neumann boundary conditions of zero pressure gradient are applied to the remaining faces. For simplicity, the porous coupon is assumed to be completely saturated with liquid sodium. An iteration scheme using the *regula falsi* technique is employed to modify an initial

estimate of κ until the outlet velocity at $x = L$ converges with the experimentally measured velocity u_{meas} (error < 0.1%). The permeability data are tabulated in Table C1, and the calculation of the permeability uncertainty is discussed in Appendix C.

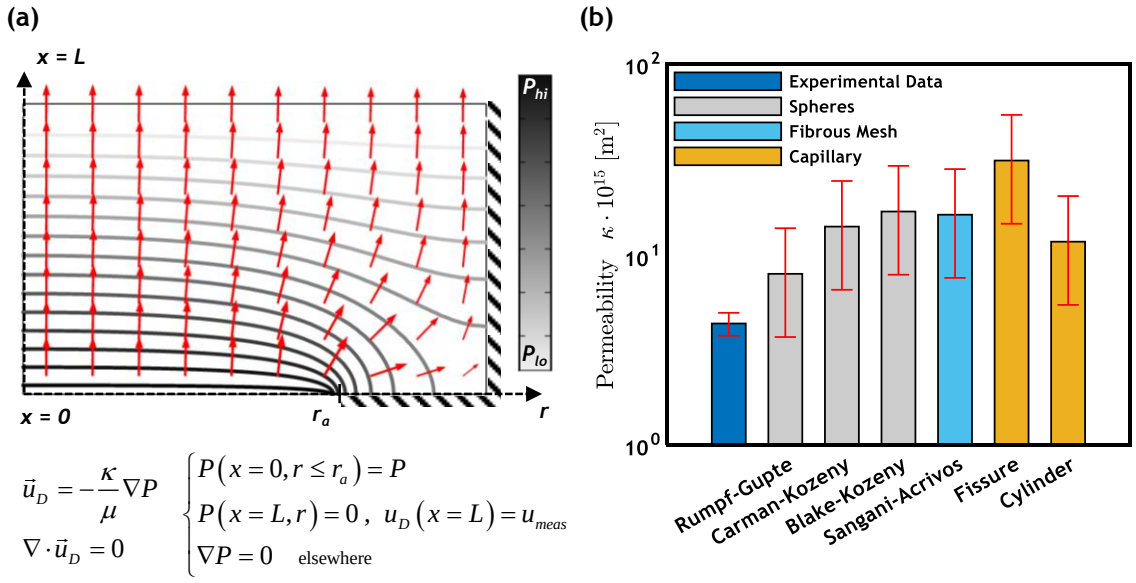

Figure 4.9 (a) COMSOL model used to find the spreading mass transfer resistance for viscous flow in an axisymmetric cylinder. The red arrows represent the logarithm of the velocity vector. (b) Bar graph of the measured permeability compared to models for three types of geometries (sphere, cylindrical fibrous mesh, and capillary).

The average permeability over all the experimental runs is $(4.6 \pm 1.3)\cdot 10^{-15}$ m^2. This small magnitude for permeability confirms that $Re_\kappa << 1$ and validates the use of Darcy's law for momentum conservation. In Figure 4.9b, this measurement is compared to the permeabilities predicted with various models. The functions of these permeability models in terms of porosity and pore/solid diameter are tabulated in Table 4.1. While the breakthrough pressure is assumed to be limited by the largest pores, the permeability magnitude is affected by the entire distribution of pore sizes. A value of d_p = 2.1 μm is therefore used to calculate the permeability with these models, which is the arithmetic

mean of the porous sample diameter limits. These models are classified according to the physical geometry they represent (*i.e.,* spheres, cylindrical fibers, or capillaries); these classifications are analogous to the geometries considered in the breakthrough pressure analysis. For a porous structure consisting of packed spheres, the Rumpf-Gupte model is an empirical equation which makes no assumption about the underlying pore structure.[127] In contrast, the Carman-Kozeny model considers internal laminar flow through a packed bed of spheres using an equivalent hydraulic diameter. The Blake-Kozeny model is also derived using a hydraulic diameter, but an empirical constant is used to modify the Fanning friction factor.[125] The permeability of fibrous beds, consisting of thin circular cylinders, can be represented by the mechanistic Sangani-Acrivos model.[128] This geometry coincides well with the stacked mesh and fused mesh models described in Section 4.2.1. Finally, capillary permeability models for rectangular fissures and straight circular cylinders are included. These are derived by considering Poiseuille flow within the capillaries, and they are modified into pseudo-3D models by multiplying them by a factor of 1/3.[129] This factor can be considered a form of tortuosity for the capillaries. The error calculation for all these permeability models is discussed in Appendix C.

Table 4.1 Permeability as a function of porosity and pore/solid diameter for various permeability models described in Section 4.3.

Model	**Permeability Function**
Rumpf-Gupte [127]	$\kappa = D_p^2 \frac{\varphi^{5.5}}{5.6}$
Carman-Kozeny [129]	$\kappa = D_p^2 \frac{\varphi^3}{180(1-\varphi)^2}$

Blake-Kozeny [125]	$\kappa = D_p^2 \frac{\varphi^3}{150(1-\varphi)^2}$
Sangani-Acrivos [128]	$\kappa = D_p^2 \frac{-ln(1-\varphi)-1.49+2(1-\varphi)-0.5(1-\varphi)^2}{24(1-\varphi)}$
Capillary Fissure [129]	$\kappa = d_p^2 \frac{\varphi}{12}\left(\frac{1}{3}\right)$
Capillary Cylinder [129]	$\kappa = d_p^2 \frac{\varphi}{32}\left(\frac{1}{3}\right)$

The measured permeability is smaller than the predictions from the various permeability models by a factor of 2-7. The measured result only falls within the error of the Rumpf-Gupte model, which empirically represents a structure consisting of spheres. An explanation for this relatively low value of permeability is not immediately clear, and it may be caused by several interrelated reasons. As discussed in Section 4.2.2, a loose thermal press fit or a CTE mismatch may allow for sodium to preferentially flow along the edge of the porous sample instead of uniformly throughout. A lower flow resistance leads to a higher permeability estimate, so it is possible that the true porous sample permeability is even lower than reported here. However, this mechanism does not explain why the measured value is already lower than the model predictions. Corrosion of the SS 316L porous sample does not have a straightforward effect on the permeability. While dissolution leads to mass transfer from the solid and an expansion of the flow path [130], it may also suspend corrosion products in the liquid sodium, increasing the effective viscosity. Furthermore, the assumption of a fully saturated porous coupon is not accurate because the smallest capillaries in the porous sample will not necessarily be penetrated by

the liquid sodium at the measured breakthrough pressure. These unfilled pores cause a reduction in the effective cross-section flow area, thereby modifying the measured permeability. Finally, there is uncertainty with the permeability models themselves. The arithmetic mean of the pore diameter was used for this analysis, but the geometric mean could be used instead for a better physical representation; the exact pore size distribution is unknown. Indeed, by using the geometric mean (d_p = 0.64 μm) for the permeability model predictions, the experimental value falls within the error for all the models considered here except the Rumpf-Gupte model, which then underpredicts the permeability. Information about the pore size distribution is needed to determine which of these pore diameter averages best represents the porous sample. Ultimately, the precise effect of all these phenomena on this permeability measurement is unknown and different experiments are needed to characterize their relative significance.

4.4 Summary

This chapter discusses the design and operation of an experiment built to measure the temperature-dependent breakthrough pressure of liquid sodium on a non-wetting (θ_{ca} > 90°) porous sample (0.1 μm < d_p < 4.14 μm, φ = 25%), and the permeability of this porous sample. The highest interfacial pressure recorded is 92.6 ± 5.8 kPa at a temperature of 207 ± 1 °C. The interfacial pressure monotonically decreases with temperature up to the wetting transition temperature, following a general breakthrough pressure function. The data was compared to models for several geometries (both 3D and capillary structures). Most of these models overestimate the measured breakthrough data. Among the 3D models considered, the data align well with the stacked mesh model and the rectangular packed spheres model. However, the latter model's porosity (φ = 48%) does not coincide with the

properties of the porous sample used for these experiments (φ = 25%), while the former model's geometry does not represent the actual structure observed under SEM. The breakthrough pressure model for straight capillaries also overestimates the measurements, but approaches the data as the eccentricity of the elliptical perimeter approaches unity. This agrees with the predictions from the stacked mesh 3D model, whose cross-section resembles a high eccentricity ellipse. Several reasons can explain the relatively low magnitude of the measured breakthrough pressure. Most importantly, the experiment is extremely sensitive to the wait time used between pressure increments, and to the mechanical defects in the construction of the experimental coupon. These effects manifest in large error bars for the data, and a significant variation in pressure (up to 40 kPa) at nearly isothermal conditions. Lower measured breakthrough pressures can also be caused by contact angle hysteresis, disruption of the surface oxide film, and corrosion. The models estimate the wetting transition temperature (where liquid sodium enters a wetting regime with $\theta_{ca} < 90°$) at 415 ± 1 °C. Despite the poor correspondence between these models and the data, this result coincides very well with a linear extrapolation for the wetting transition temperature to 411.6 ± 5.3 °C. Finally, the measured permeability of the porous sample was $(4.6 \pm 1.3)\cdot 10^{-15}\ m^2$. This measurement was compared to the values from permeability models for geometries analogous to those used for the breakthrough pressure analysis. It was shown that the Rumpf-Gupte model for packed spheres gave the closest estimate to the data, while all the other models overestimate the permeability. The same physical conditions that affect the breakthrough pressure can also lead to a lower permeability. The data from this experiment are used to guide the design and operation of the capillary pumping experiment described in Chapter 5.

CHAPTER 5. CAPILLARY PUMPING THROUGH CONDENSATION WITHIN A NON-WETTING POROUS STRUCTURE

This chapter discusses a unique, low-temperature, liquid sodium capillary pump for the Na-TEC. This pump operates by allowing low-pressure sodium vapor to condense within a non-wetting ($\theta_{ca} > 90^{o}$) porous structure; the liquid adjacent to this condensation interface is at a higher pressure than the vapor due to the interface curvature. A net force acts upon the liquid sodium at the solid-liquid-vapor interface, effectively "pushing" it towards the higher pressure bulk liquid region. This is in contrast to traditional wicks, where the liquid is "pulled" against a pressure gradient by the solid surface adhesion force.[65] Section 5.1 describes the design of an experiment used to demonstrate the feasibility of this pumping mechanism. To predict the performance of this pumping experiment (*i.e.*, mass flowrate and pressure head), a conjugate heat transfer model is developed in Section 5.2 which considers the coupled momentum and thermal transport processes within the non-wetting porous structure as sodium vapor is condensed. After the operating conditions for this experiment are established, the procedure is discussed in Section 5.3. In Section 5.4, the results of two experiments are discussed in detail, both of which demonstrate evidence of liquid sodium pumping. Finally, Section 5.5 summarizes the findings in this chapter, with the aim of answering the thesis question: *To what degree (pressure head and discharge rate) can passive liquid-sodium pumping be maintained through the condensation of sodium vapor within a non-wetting porous structure?*

5.1 Capillary Pumping Experiment Design

Figure 5.1a shows the basic schematic of the experiment, which is housed inside an argon glovebox to prevent sodium oxidation. There are three distinct regions within the experimental assembly: the evaporator plenum ($-L_{ev} < x < 0$), the experimental coupon ($0 < x < L_{ex}$), and the upper plenum ($x > L_{ex}$). The experimental coupon (Figure 5.1b) consists of a porous insert ($0 < x < L_{ex} - L_{pc}$), a porous coupon ($L_{ex} - L_{pc} < x < L_{ex}$), and a SS 316 tube that surrounds both of these. A commercially available SS 316L porous structure from GKN Sinter Metals ($0.1\ \mu\text{m} < d_p < 4.14\ \mu\text{m}$, $\varphi = 25\%$) is used as the porous coupon because it is non-wetting ($\theta_{ca} > 90°$) to liquid sodium up to a wetting transition temperature of 412 °C (see Section 4.1.1). Liquid sodium is heated in the evaporator plenum at T_{evap}, and the total pressure of the binary mixture of sodium vapor and argon in this plenum is regulated at P_{atm} through the evaporator relief valve. Liquid sodium is added to the upper plenum in order to form an initial condensation interface at $x = L_{ex}$. Since the sodium is non-wetting to the porous coupon, it will remain in the upper flange unless the breakthrough pressure for the interface is exceeded. To maintain a pressure difference against which to pump, the upper plenum is pressurized above the atmosphere ($P > P_{atm}$) and passively managed with a commercially available pressure regulator. As sodium condenses at the interface, the liquid is pushed against this imposed pressure gradient by the solid-liquid-vapor interfacial force (see Figure 5.1a inset), and pumping is achieved. As discussed in Chapter 4, for a liquid-vapor system, the net pressure difference across the interface is described by the Laplace equation $P_L = 2\sigma_{lv}K_{12}$.[104] In the presence of a solid surface, the Laplace pressure is a function of the surface tension σ_{lv}, the characteristic pore diameter d_p, and the contact angle θ_{ca} between the liquid and the solid. The Laplace pressure supplies the driving force

for the capillary pumping. This capillary pumping method is fundamentally a thermally driven process, so the temperature distribution in this experiment must be precisely controlled. The evaporator plenum must be superheated above T_{evap}, including the inlet to the experimental coupon at $x = 0$ where $T_{in} > T_{evap}$, because sodium should only condense at the imposed condensation interface at $x = L_{ex}$. The condensation interface at $x = L_{ex}$ (the outlet of the experimental coupon) must be kept at $T_{out} < 412$ °C, otherwise the sodium will transition into the wetting regime ($\theta_{ca} < 90°$) and the interface will be destabilized, thereby preventing sodium pumping. In the upper plenum ($x > L_{ex}$), the remaining structure must be heated above the melting point of sodium to prevent clogging.

Two practical experimental conditions must be addressed. First, the interface is not established via direct condensation, but rather it is artificially created by adding an initial supply of liquid sodium to the upper plenum. In a real capillary pump, this interface is established during the initial transient heating step as hot sodium condenses within the porous structure. However, the experiment is greatly simplified by forming this interface artificially. Second, there is no sodium recirculation; once the sodium is exhausted in the evaporator, the experiment cannot continue. This implies that the experiment is always operating transiently, given that the evaporator interface at $x = -L_{ev}$ will become more negative as the experiment proceeds. This transient operation also affects the static sodium pressure head in the upper plenum, which continuously increases as sodium is being pumped from the evaporator. However, the mass flowrate is very slow (see Section 5.2.4), so the experimental is operating in a quasi-steady regime.

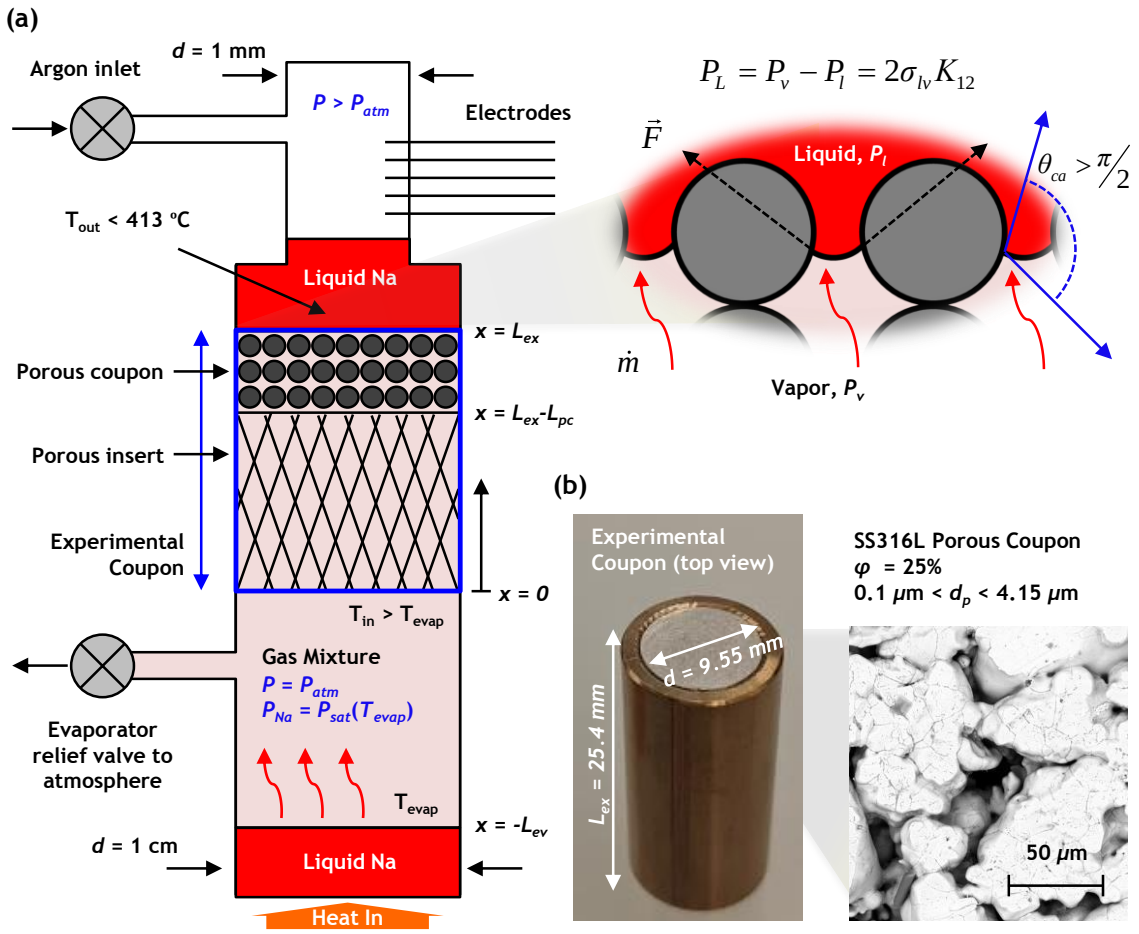

Figure 5.1 (a) Schematic of the capillary pumping experiment. The three major zones are: the evaporator plenum ($-L_{ex} < x < 0$), the experimental coupon ($0 < x < L_{ex}$) and the upper plenum ($x > L_{ex}$). The evaporator plenum consists of a sodium vapor-argon mixture regulated at the atmosphere pressure. The experimental coupon consists of a porous insert and a porous coupon. Liquid sodium is added directly to the upper plenum, which is pressurized above the atmosphere. (inset) The liquid sodium is non-wetting to the porous coupon, so the contact angle is $\theta_{ca} > 90^{o}$. (b) Top view of the experimental coupon, where the SS 316L porous coupon is visible

Figure 5.2 shows a CAD model of this experiment setup. Two SS 316 flanges are used to compress the experimental coupon. The evaporator plenum is directly machined with the bottom flange from a single SS 316 stock piece, and the upper plenum is likewise connected to the top flange. Cartridge heaters are inserted radially into the bottom flange to superheat the evaporator plenum and the experimental coupon. Separate heater blocks

are attached to the evaporator and the relief valve to maintain this superheated condition. Sodium is added directly into the evaporator plenum up to a level shown in Figure 5.2, which is adjacent to a thermocouple for an accurate measurement of T_{evap}. Sodium is also directly added to the top flange where it will be melted to form the condensation interface. As sodium is pumped, the mass flowrate in the upper plenum is measured using an electrode prism with SS 316 electrodes cemented along the flow path of the liquid sodium. An Omegabond 600 high-temperature cement is used to mount the electrodes onto the prism, which is replaced every 3-5 experiments due to mechanical degradation. These electrodes are electrically isolated from the flange, and they are only exposed to the flow path. Thus, as liquid sodium flows it will make contact with sequential electrodes and complete an electrical circuit; all five electrodes are connected in parallel to a 3V battery for this purpose. This method was also used to detect the flowrate of liquid sodium for the breakthrough pressure experiment discussed in Chapter 4. The experimentation time is inversely proportional to the flow velocity in the upper plenum; the flow velocity is approximated by dividing the distance between successive electrodes by the difference in their activation times. Due to the low flowrates in this experiment, the flow diameter in the electrode prism should be small to promote a manageable experimentation time of $t_{tot} \sim \mathcal{O}(10\ h)$.

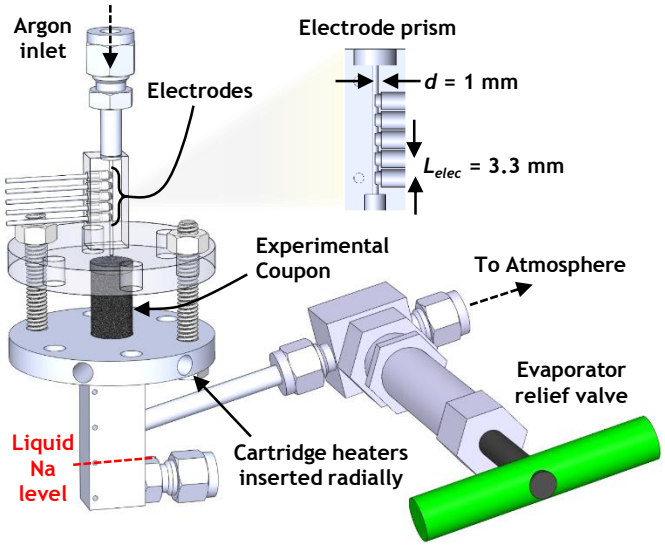

Figure 5.2 CAD model of the capillary pumping experiment. The evaporator and the relief valve heater blocks are not depicted.

5.2 Conjugate Transport Model for Sodium Vapor

5.2.1 Conservation of Momentum

The most accurate expression of the conservation of momentum for flow in porous media is actively debated.[124] Hsu and Cheng developed an equation in 1990 that accounts for inertial and viscous effects in an isotropic porous medium, and also includes the higher order Forchheimer and Brinkmann terms.[131] The Forchheimer term accounts for the quadratic form drag caused by solid elements in the porous structure which obstruct the flow, while the Brinkmann term allows for the application of a no-slip boundary condition, which is specifically needed when considering porosity variation near the walls.[124] The inertial term is obtained by analogy to Navier-Stokes, but it is controversial because it cannot mathematically account for non-linear drag and it is inconsistent with the boundary condition for Darcy's law.[132] A more general expression for momentum conservation (Equation 5.1) also considers a gravitational body force, using the Boussinesq

approximation for the temperature dependent compressibility.[133] Here, the Darcy velocity u_D is related to the absolute velocity u via the Dupuit-Forchheimer relationship $u_D = \varphi u$.[125] In this experiment, flow occurs in a small Reynold's number regime, and the pressure gradient scales with the viscous forces (*i.e.*, Darcy term). Thus, the appropriate scaling law is $P_0/L \sim u_{D,0}(\mu/\kappa)$. Equation 5.2 represents the proper scaling for the terms in the steady-state momentum conservation equation when each term is normalized by the scaled viscous component. For small flow velocities (*i.e.*, $Re_{\sqrt{\kappa}} << 1$), the Forchheimer term is neglected. When the characteristic length is $L >> \sqrt{\kappa}$, the Brinkmann and inertial terms are also neglected.[124] In the scaled component of the natural convection, $Gr_{\sqrt{\kappa}}$ is the modified Grashof number (Equation 5.3), and when $Gr_{\sqrt{\kappa}} << Re_{\sqrt{\kappa}}$, this term can also be neglected.[134]. Thus, the pressure gradient and viscous terms are of leading-order, and the classic Darcy law (Equation 5.4) is recovered for the relevant conditions in this experiment. This equation applies to gas flow in both the porous coupon and the porous insert.

$$\underbrace{\frac{1}{\varphi}\frac{\partial \vec{u}_D}{\partial t}+\frac{1}{\varphi^2}\left(\vec{u}_D\cdot\nabla\right)\vec{u}_D}_{\text{Inertial}} = \frac{-\nabla P}{\rho} - \underbrace{\frac{\mu}{\rho\kappa}\vec{u}_D}_{\text{Darcy}} - \underbrace{\frac{c_f}{\sqrt{\kappa}}\left|\vec{u}_D\right|\vec{u}_D}_{\text{Forchheimer}} + \underbrace{\frac{\mu_{eff}}{\varphi\rho}\nabla^2\vec{u}_D}_{\text{Brinkmann}} - \underbrace{\beta\left(T-T_\infty\right)\vec{g}}_{\text{Boussinesq}} \tag{5.1}$$

$$\begin{cases} \dfrac{1}{\varphi^2}\left(\vec{u}_D\cdot\nabla\right)\vec{u}_D \Big/ \left(u_{D,0}\mu/\rho\kappa\right) \sim \dfrac{1}{\varphi^2}\dfrac{Re_{\sqrt{\kappa}}}{Re_L} \\ \dfrac{c_f}{\sqrt{\kappa}}\left|\vec{u}_D\right|\vec{u}_D \Big/ \left(u_{D,0}\mu/\rho\kappa\right) \sim c_f Re_{\sqrt{\kappa}} \\ \dfrac{\mu_{eff}}{\varphi\rho}\nabla^2\vec{u}_D \Big/ \left(u_{D,0}\mu/\rho\kappa\right) \sim \dfrac{1}{\varphi}\left(\dfrac{\mu_{eff}}{\mu}\right)\dfrac{\kappa}{L^2} \\ \beta\left(T-T_\infty\right)\vec{g} \Big/ \left(u_{D,0}\mu/\rho\kappa\right) \sim \dfrac{Gr_{\sqrt{\kappa}}}{Re_{\sqrt{\kappa}}} \end{cases} \tag{5.2}$$

$$Re_{\sqrt{\kappa}} = \frac{\rho u_{D,0}\sqrt{\kappa}}{\mu}, Gr_{\sqrt{\kappa}} = \frac{\beta\left(T_0-T_\infty\right)\rho^2\kappa^{3/2}}{\mu^2} \tag{5.3}$$

$$\vec{u}_D = -\frac{\kappa}{\mu}\nabla P \tag{5.4}$$

5.2.2 Conservation of Mass

The conservation of mass can be expressed as a function of the velocity u_D in the porous structure. The advective-diffusive model is used for the conservation of mass (Equation 5.5) where both advection and binary diffusion are relevant.[135] Using Fick's law, the diffusion of sodium vapor in argon is proportional to an effective diffusivity D_{eff} and the gradient of the mass fraction ω_i. The sodium vapor, whose partial pressure P_i is close to saturation, can be treated as an ideal gas for the relevant experiment temperature range because its compressibility factor is close to one (< 6% deviation from unity for 500 K < T_{evap} < 900 K), and its pressure is significantly lower than the critical pressure (25.64 MPa for sodium).[120] Thus, the sodium-argon gas mixture is treated as an ideal gas and the mass fraction can be expressed as the ratio of the partial pressure to the total pressure $\omega_i = P_i / P_{atm}$, where the total pressure is regulated at P_{atm} in the evaporator plenum. The

maximum partial pressure of sodium vapor is at the evaporation interface ($x = -L_{ev}$), where $P_{Na} = P_{sat}(T_{evap})$ is determined using an empirical Antoine equation (Equation 5.6).[72]

$$\varphi \frac{\partial \rho_i}{\partial t} + \nabla \cdot \left[\rho_i \left(-\frac{\kappa}{\mu} \nabla P \right) - \rho D_{eff} \nabla \omega_i \right] = 0 \tag{5.5}$$

$$log\, P_{sat} = 4.521 - \frac{5220}{T_{sat}} + log(101325) \quad [\mathrm{Pa}] \tag{5.6}$$

The solubility of argon gas in liquid sodium follows Henry's law up to moderate pressures [136], otherwise it is impermeable in liquid sodium (*i.e.*, non-condensable). Therefore, the total gas mixture velocity is only a function of the sodium vapor velocity if the liquid sodium at the evaporator and condensation interfaces is assumed to be saturated with argon. Since the sodium vapor pressure at T_{evap} is relatively small, the dilute gas approximation $\omega_i << 1$ can be employed to neglect advection.[86] Thus, Equation 5.5 reduces to Fick's law for binary diffusion. If the presence of the relief valve is ignored for now, Equation 5.7 describes the unidirectional diffusion of sodium vapor in the evaporator and the experimental coupon. There are three transport zones for the sodium vapor: the evaporator interface to the experimental coupon inlet ($-L_{ev} < x < 0$), the porous insert ($0 < x < L_{ex} - L_{pc}$), and the SS 316L porous coupon ($L_{ex} - L_{pc} < x < L_{ex}$). The overall boundary conditions (Equation (5.8) are the sodium saturation pressure at the evaporator ($x = -L_{ev}$) and Kelvin's equation at the condensation interface ($x = L_{ex}$); the latter describes the change in vapor pressure due a curved interface (see Figure 5.1a inset).[137] Mass continuity is applied at each zone interface.

$$\dot{m} = AD_{eff}\rho_{avg}\frac{d}{dx}\left(\frac{P_{sat}\left(T_x\right)}{P_{atm}}\right) \tag{5.7}$$

$$\text{BC:}\begin{cases} P_{x=-L_{ev}} = P_{sat}\left(T_{evap}\right) \\ P_{x=L_{ex}} = P_{sat}\left(T_{out}\right)exp\left(\dfrac{P_L}{\rho_{x=L}T_{out}\left(\bar{R}/M\right)}\right) \end{cases} \tag{5.8}$$

Some aspects of this model must be addressed. First, the presence of the evaporator relief valve (and the tube connecting it to the assembly) modifies the diffusion in the evaporator plenum by reducing the mass transfer resistance. To account for this effect, the diffusion length in the evaporator L_{ev} is conservatively reduced by 6.35 mm, which corresponds to the diameter of the tube linking the valve to the evaporator plenum. Second, the gas in the evaporator is not incompressible because the density and the effective diffusivity are temperature dependent. However, by calculating these properties at the geometric average temperature in each zone, Equation 5.7 can be made temperature-independent (< 1.6% error). Finally, although the sodium vapor is superheated, its density is approximated with the saturation value for a given temperature.

The transport properties of a rarefied gas depend on the Knudsen number *Kn*. In a porous material, the pores can be treated as straight cylindrical tubes with pore diameters d_p for simplicity. In a sufficiently long cylinder ($L/d_p >> 1$), the mass flowrate is given by the Dushman formula when the gas exists in the free-molecular flow regime ($Kn > 10$) [73]. This transport is described with a Knudsen diffusivity D_{Kn} (Equation 5.9). For ordinary molecular diffusion ($Kn << 1$) , an empirical equation is used for the temperature-dependent binary diffusivity D_O between the sodium vapor and argon (Equation

5.10).[138] In the transition flow regime ($0.1 < Kn < 10$), the frequency of gas molecule collisions is on the same order as collisions with the cylinder walls.[139] Therefore, Knudsen diffusion occurs in series with ordinary diffusion, and the total binary diffusivity D_{ij} is the inverse of the reciprocal sum of both (Equation 5.11, often called the Bosanquet relation).[140] In a porous structure, the effective diffusivity is expressed by Equation 5.12, where τ is the porous structure tortuosity. Researchers have proposed several models for τ that depend on the porosity magnitude, the solid geometry of the porous structure, and the connectivity of the pores.[141, 142] The most widely used expression is the Bruggeman tortuosity model $\tau = \varphi^{-1/2}$, which works well for a packed sphere geometry.[143] This expression is used as a conservative estimate for the tortuosity of the porous coupon in this experiment.

$$D_{Kn} = \frac{4}{3} d_p \sqrt{\frac{\bar{R}T}{2\pi M}} \tag{5.9}$$

$$D_O = \left(5.09 \bullet 10^{-10}\right) T^{1.85} \quad \left[\mathrm{m^2/s}\right] \tag{5.10}$$

$$D_{ij} = \left(D_{Kn}^{-1} + D_O^{-1}\right)^{-1} \tag{5.11}$$

$$D_{eff} = \frac{\varphi}{\tau} D_{ij} \tag{5.12}$$

The total mass flowrate of sodium vapor is calculated with Equation 5.13 for $-L_{ev} < x < L_{ex}$ using the geometric average temperature within each of the three zones to calculate the thermophysical properties. In the evaporator plenum ($-L_{ev} < x < 0$), there is no porous structure so D_{eff} is replaced by D_{ij}. Equation 5.13 is a function of T_{evap}, T_{cond}, and

the pressure P_L at the condensation interface. The two temperatures are independent input variables, but a second equation describing the viscous transport of liquid sodium in the upper plenum is needed to solve for P_L. However, the argument of the exponential term in Equation 5.8 is typically very small, so the pressure at $x = L_{ex}$ is simply $P_{sat}(T_{out})$. Therefore, in Equation 5.13 the variable P_L is ignored and the equation is fully determined. P_L can instead be calculated by measuring the mass flowrate in an experiment and applying the extended Bernoulli equation for incompressible viscous flow, which accounts for the various pressure heads in the upper plenum.[144] To find the maximum interfacial pressure that can be generated (*i.e.,* maximum pressure head of the capillary pump), the breakthrough experiment discussed in Chapter 4 must be conducted. The sodium contact angle for this pumping experiment is also affected by the mechanism discussed in Section 4.2.2 (adsorbed gases, surface oxide condition, *etc.*). The experiment described herein is similar to a heat pipe in that sodium vapor is transported by evaporation and condensation in different zones. However, whereas the transport in a heat pipe is limited by various effects (*i.e.,* viscous and gravitational forces, choked flow, entrained liquid, or critical boiling)[145], the transport in this experiment is strictly governed by vapor diffusion.

$$\dot{m} = \left(\frac{L_{ev} - 6.35\text{mm}}{A_{ev} D_{ij,ev}} \left(\rho_{sat,ev} + P_{atm} \Big/ R_{Ar} \sqrt{T_{evap} T_{x=0}} \right) + \right.$$
$$\frac{L_{ex} - L_{pc}}{A_{pc} D_{eff,pi}} \left(\rho_{sat,pi} + P_{atm} \Big/ R_{Ar} \sqrt{T_{x=0} T_{x=L_{ex}-L_{pc}}} \right) + \qquad (5.13)$$
$$\left. \frac{L_{pc}}{A_{pc} D_{eff,p}} \left(\rho_{sat,pc} + P_{atm} \Big/ R_{Ar} \sqrt{T_{x=L_{ex}-L_{pc}} T_{out}} \right) \right) \left(\frac{P_{x=L_{ex}} - P_{x=-L_{ev}}}{P_{atm}} \right)$$

5.2.3 Conservation of Energy

A quasi-dimensional control volume with local thermal equilibrium (LTE) between the solid porous structure and the gas is used to define the volume averaged energy conservation equation. LTE exists when the temperature difference between the solid and gas phases is much smaller than the difference over the system dimension *L*.[146] Several criteria have been proposed for the validity of the LTE assumption, so the expression defined by Kim and Jang (Equation 5.14) is used for a general system in which convection heat transfer might not be negligible.[147] For *Nu*, the experimental correlation developed by Wakao *et. al.* (Equation 5.15) is employed.[148]

$$\left(\rho c_p\right)_f \left(\frac{k_f \varphi}{k_s\left(1-\varphi\right)}\right)^2 Re_{d_p}\left(\frac{d_p}{L}\right)\frac{\varphi}{Nu} << 1 \tag{5.14}$$

$$Nu = 2 + \left(1.1\right) Pr_f^{1/3}\, Re_{d_p}^{0.6} \tag{5.15}$$

When LTE is satisfied, the conservation of energy is given by Equation 5.16, which neglects energy source terms.[149] The viscous dissipation is defined by $\Phi = -\vec{u}_D \cdot \nabla P$, which is the average rate of work done by the pressure.[124] Equation 5.17 represents the proper scaling for each term in the steady-state energy conservation equation when they are normalized by the scaled thermal diffusion component, and when the pressure gradient is expressed by the Darcy law (Equation 5.4). For small flow velocities (*i.e.*, $Re_{\sqrt{\kappa}} << 1$), the Peclet number $Pe \rightarrow 0$ and advection can be neglected. Using the Brinkmann number defined in Equation 5.18, the viscous dissipation is negligible when $Br << \kappa/L^2$.[150] Thus, the thermal diffusion term is of the leading-order, and it describes conduction heat transfer

in a quiescent medium with an effective thermal conductivity k_{eff}. The thermal conductivity of the sodium-argon mixture k_g is approximated using a binary mixture model for monatomic gases.[151] For simplicity, heat conduction is assumed to occur in parallel between the gas mixture and the solid, so k_{eff} is expressed as a weighted sum of the gas and solid thermal conductivities (Equation 5.19).[59] For the SS 316L porous coupon, $k_{eff} \approx 15$ W/m/K. At the condensation interface, there are two additional thermal resistances that must be addressed: the interfacial thermal resistance between the saturated sodium vapor and the liquid described by the Schrage equation, and the depression of the normal equilibrium interface temperature caused by its curvature.[121] Since the flowrate is small, the condensation process is far from the kinetic limit for heat flux so these thermal resistances are negligible compared to thermal conduction in the experiment. Thus, the temperature of the condensation interface T_{out} corresponds to the saturation temperature of the local sodium partial pressure. Likewise, the temperature at the evaporator interface is T_{evap}.

$$\underbrace{\left(\rho c_p\right)_{eff}\frac{\partial T}{\partial t}+\left(\rho c_p\right)_f \vec{u}_D\cdot\nabla T}_{\text{Advection}} = \underbrace{k_{eff}\nabla^2 T}_{\text{Diffusion}} - \underbrace{\vec{u}_D\cdot\nabla P}_{\substack{\text{Viscous}\\ \text{Dissipation}}} \tag{5.16}$$

$$\begin{cases} \left(\rho c_p\right)_f \vec{u}_D\cdot\nabla T \Big/ \left(k_{eff}T_0/L^2\right) \sim Pe \\ \vec{u}_D\cdot\nabla P \Big/ \left(k_{eff}T_0/L^2\right) \sim Br\left(\dfrac{\kappa}{L^2}\right)^{-1} \end{cases} \tag{5.17}$$

$$Pe=\frac{\left(\rho c_p\right)_f u_0\sqrt{\kappa}}{k_{eff}},\ Br=\frac{u_0^2\mu}{k_{eff}T_0} \tag{5.18}$$

$$k_{eff} = (1-\varphi)k_s + \varphi k_{gas} \tag{5.19}$$

The steady-state temperature distribution for this experiment is estimated with a quasi-axisymmetric 3D COMSOL model (Figure 5.3a). A ¼ model with symmetry boundaries is used to reduce computational time. For this model, it is assumed that the condensation front is steady (*i.e.*, immobile from $x = L_{ex}$ position), the capillary pressure at $x = L_{ex}$ is uniform (*i.e.*, isotropic, homogeneous pores), and the two-phase zone is infinitesimal; these assumptions have been explicitly and implicitly applied in various condensation models.[61, 152-154] An effective thermal conductivity is used for both the porous insert and the porous coupon, while $k_g \approx 0.015$ W/m/K is used in the evaporator plenum. To approximate the experiment conditions with this finite-element model, the following boundary conditions were enforced: heat input only occurs from the cartridge heaters in the bottom flange and the from the evaporator heater block (see Figure 5.3a); a surface boundary heat source, proportional to h_{fg}, is used to account for heat released by the condensing sodium at $x = L_{ex}$; the bottom flange and the experimental coupon surfaces are assumed to be adiabatic; external radiation from the SS 316 assembly occurs with an emissivity of $\varepsilon_{316} = 0.6$ [86]; and finally the convection coefficients at the bottom of the evaporator, the top flange, and the top surface (representing the boundary with the remaining assembly tubing not shown) were all tuned to match the temperatures observed during preliminary experimental attempts. This COMSOL model does not include the evaporator plenum relief valve. Adding this valve to the finite-element mesh is an unnecessary complication for determining the temperature distribution because its effect is reasonably captured by tuning the convection coefficients in COMSOL to match the

experimental temperature data. Figure 5.3b shows the temperature profile along the center of the geometry and along the boundary between the internal fluid and the enclosure. Knowing the temperature distribution inside the experimental coupon is critical for this experiment. As discussed in Section 5.2.4, an accurate estimate of the temperature slope within the porous coupon (adjacent to the condensation interface) is particularly important for preventing undesired sodium condensation.

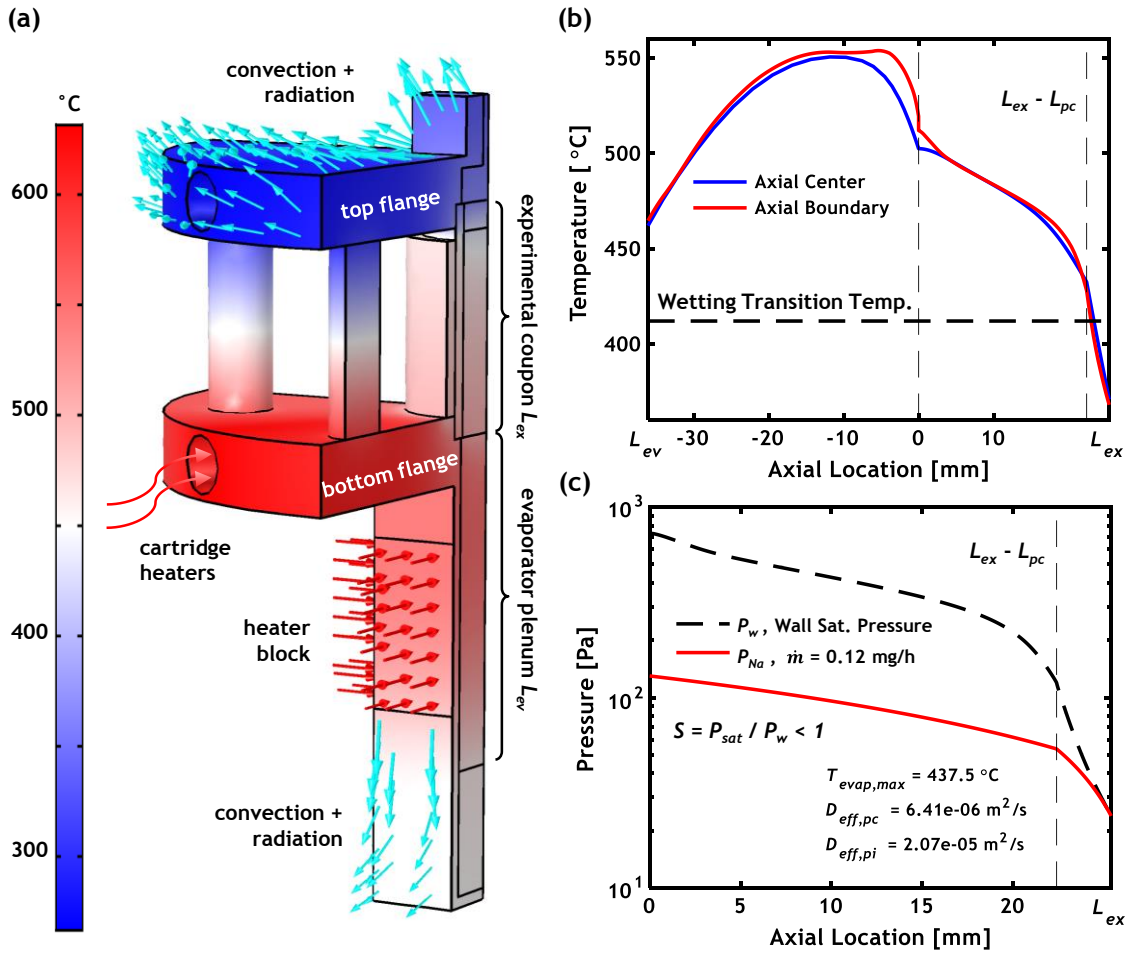

Figure 5.3 (a) COMSOL model with a ¼ geometry and symmetry boundaries used to estimate the temperature distribution. The heat input occurs through cartridge heaters in the bottom flange and at the evaporator plenum, represented by red arrows. Heat escapes at the bottom of the evaporator and from the top flange, represented by cyan arrows. The rest of the exterior is assumed to be adiabatic. (b) Temperature distribution along the center and the boundary between the internal fluid and the enclosure. The wetting transition

temperature is represented by a horizontal dashed line at 412 °C. (c) Saturation pressure of sodium corresponding to the boundary wall temperature from (b), and the sodium partial pressure as a function of the axial distance. The sodium pressure is lower than the wall saturation pressure, except at $x = L_{ex}$ where condensation takes place and $S = 1$.

5.2.4 Maximum Allowable Mass Flowrate

As discussed in Section 5.1, the entire evaporator region must be superheated so that sodium condensation only occurs at the imposed interface at $x = L_{ex}$. To prevent condensation, particularly within the porous coupon, the supersaturation of sodium vapor $S = P_{Na}/P_w$ should be below the kinetic limit for heterogeneous nucleation of liquid droplets.[121] Here, $P_w = P_{sat}(T_w)$ is the saturation pressure of sodium at the solid wall temperature. A more conservative condition is imposed in this experiment, where the supersaturation sodium vapor is $S < 1$ in the experimental coupon except at the condensation interface where $S = 1$.[155] This supersaturation condition limits the maximum mass flowrate $\dot{m}_{max}$ that can be sustained in the experiment before the porous structure begins to flood with condensing sodium. Specifically, the transport within the porous coupon (adjacent to the condensation interface) determines the magnitude of $\dot{m}_{max}$. The mass flowrate is proportional to the pressure gradient in the porous coupon (Equation 5.7). To impose $S < 1$ at $x < L_{ex}$, the pressure gradient is set equal to the slope of P_w at the condensation interface, which is related to the slope of the wall temperature ($\Delta T_w/\Delta x \rightarrow \Delta P_w/\Delta x$ at $x = L_{ex}$). The slope of the wall temperature is determined with the COMSOL model (Figure 5.3b), and the associated saturation pressure gradient is then found using Equation 5.6. $\dot{m}_{max}$ is then determined by applying this pressure gradient into Equation 5.7. In Figure 5.3c, the pressure profile of P_{Na} at the maximum mass flowrate within the experimental coupon is compared to the saturation pressure of sodium at the wall

temperature. Once $\dot{m}_{max}$ is known, the maximum allowable evaporator temperature T_{evap} in the experiment can be determined using Equation 5.13 for a given T_{out}.

An effective method of increasing $\dot{m}_{max}$ is to use a highly conducting porous insert so that most of the temperature drop occurs within the porous coupon. Figure 5.4a shows how the wall temperature slope at $x = L_{ex}$ increases as the thermal conductivity of the porous insert inside the experimental coupon increases. Note that the maximum mass flowrate is limited by the smallest of either the center or the boundary temperature slopes. Copper, with a nominal thermal conductivity of 400 W/m/K, is an excellent candidate for the porous insert. A copper cylinder of length $L_{ex} - L_{pc}$ is machined with 7 axial thru-holes to create a porous insert with a small porosity of $\varphi \approx 20\%$ (Figure 5.5a); low porosity structures maximize the effective thermal conductivity (Equation 5.19). Due to the straight cylindrical flow paths in this copper cylinder, its tortuosity is effectively $\tau = 1$. For the surrounding tube of the experimental coupon, a less conductive material limits thermal conduction along the sides of the porous structure, thereby increasing the temperature slope next to the condensation interface. Thus, an SS 316 tube ($k \approx 20$ W/m/K) is preferable to a copper tube. To further increase the temperature slope, a copper sleeve is placed around the experimental coupon. This forces most of the temperature drop to occur along the porous coupon by increasing thermal conduction only up to $x = L_{ex} - L_{pc}$. Figure 5.4b shows the significant effect that adding a copper sleeve has on the temperature profile of the porous coupon.

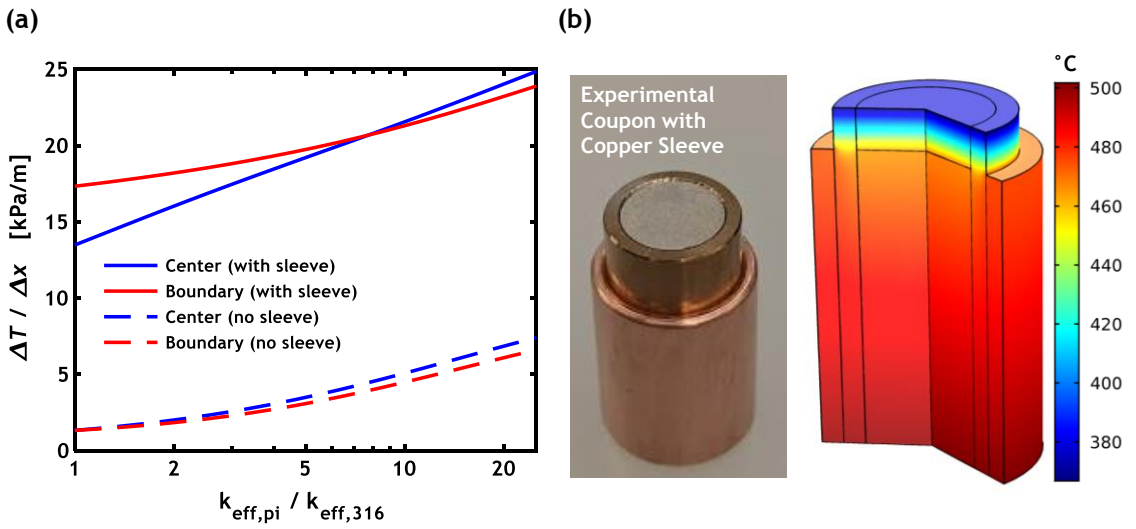

Figure 5.4 (a) Temperature slope at $x = L_{ex}$ as a function of the effective thermal conductivity of the porous insert. (b) The experimental coupon with a copper sleeve, and a COMSOL model of its temperature distribution. With a copper sleeve, the majority of the temperature drop occurs in the porous coupon adjacent to the condensation interface.

5.3 Capillary Pumping Experiment Procedure

The SS 316L porous coupon is cut into a cylinder (9.60 mm diameter, L_{pc} = 3 mm) using electric discharge machining (EDM), and the porous insert is machined from a copper rod (9.60 mm diameter, $L_{ex} - L_{pc}$ = 22.4 mm). The machined SS 316L porous coupon is then press-fit into a SS 316 tube (12.7 mm outer diameter, 9.55 mm inner diameter) by thermally expanding the tube at 425 ^{o}C and then immediately hammering the porous coupon into position while the tube is hot (see Section 4.1.1). Once the porous coupon is in position, the porous insert is pressed into the opposite side of the SS 316 tube (Figure 5.5a). The coefficient of thermal expansion (CTE) for copper is larger than for SS 316, so the contact between the porous insert and the tube will be enhanced as the system is heated. A graphite heater block surrounded by sturdy calcium silicate insulation is attached to the evaporator plenum (Figure 5.5b), and cartridge heaters are directly inserted

into this block (Figure 5.5c). A graphite heater block is also added to the evaporator relief valve to prevent sodium condensation. All components are then brought inside an argon glovebox, and sodium is added into the evaporator plenum (0.25-0.75 *g*) and the upper plenum (0.28-0.3 *g*). The sodium consists of high purity solid cubes (Sigma Aldrich 99.9%) which are dried of mineral oil and stripped of their native oxide layers until they are lustrous (see Section 4.1.2) After sodium insertion, the experimental coupon is compressed between the two flanges, and these are mounted inside the glovebox (Figure 5.5d), with cartridge heaters added radially into the bottom flange. The three sets of cartridge heaters (evaporator plenum, relief valve, and bottom flange) are individually managed with dedicated voltage controllers. To measure temperature, 16 sheathed thermocouples are inserted in strategic locations throughout the assembly, including the evaporation interface, the experimental coupon inlet/outlet, the top and bottom of the electrode prism, and the inlet to the evaporator relief valve. Finally, the entire assembly is covered with alumina foam insulation (Figure 5.5e). In particular, the region between the two flanges is thoroughly insulated to approximate an adiabatic surface for the experimental coupon.

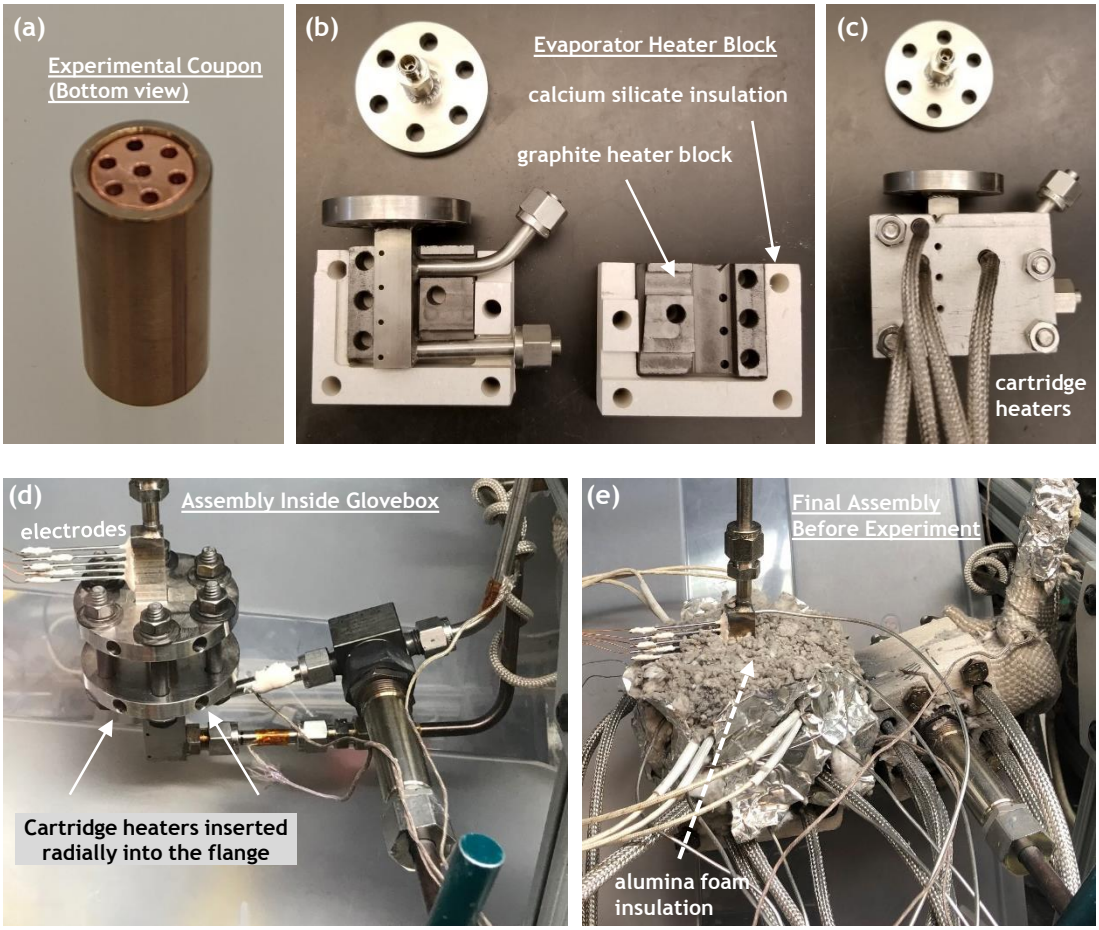

Figure 5.5 (a) Bottom view of the experimental coupon, showing the copper cylinder porous insert ($\varphi \approx 20\%$) with 7 axial thru-holes ($d = 1.59$ mm). (b) Evaporator heater block placed on the bottom flange. (c) Cartridge heaters inserted into the evaporator heater block. (d) Experiment assembly mounted inside the argon glovebox. (e) Fully insulated assembly prior to the start of an experiment.

It is critical to keep all the surfaces in the evaporator plenum superheated. Therefore, at the start of the experiment the evaporator relief valve is heated to 50 °C. This valve extends out from the evaporator and is more susceptible to detrimental sodium condensation, so it is heated first and maintained at the highest temperature throughout the experiment. This valve is opened until the temperature reaches ≈ 200 °C, after which it is closed and only swiftly re-opened every 15 °C increase to maintain the evaporator plenum pressure at P_{atm}. Next, the lower flange is slowly heated (1-2 °C/min) until T_{out} reaches the

desired value below the wetting transition temperature of ≈ 412 °C. Typically, the experiment operated between 350 °C < T_{out} < 370 °C. During this transient heating step T_{out} eventually exceeds T_{evap}, usually when the temperatures are 100-150 °C. When T_{out} > T_{evap} the diffusion mass transfer is reversed, occurring from the upper plenum to the evaporator instead. Over several runs, this temperature reversal has proven to be the most effective technique for preventing premature condensation within the experimental coupon. Once T_{out} reaches the desired value, the evaporator heaters are activated and T_{evap} is increased until it surpasses T_{out} and reaches the desired experimental value. The maximum allowable value of T_{evap} for a given T_{out} is governed by the maximum mass flowrate discussed in Section 5.2.4. During the evaporator heating, the outlet temperature is bound to also increase due to the influx of new heat. Therefore, it is necessary to manually stabilize T_{out} by removing insulation from the top flange. Once all the temperatures have stabilized, the experiment is in thermal steady-state and the mass flowrate is fixed (assuming quasi-steady transport). At this point, the experiment is left passively running for at least $2 \cdot t_{wait}$ to observe capillary pumping of the liquid sodium, where t_{wait} is the time between the activation of successive electrodes. The ratio of t_{wait} to the total experiment duration t_{tot} (Equation 5.20) is determined *a posteriori* by dividing the distance between successive electrodes L_{elec} by the hypothetical distance traveled by the liquid sodium during the experiment. The latter is calculated by integrating the volumetric flowrate of sodium at each temperature over the course of the experiment. It must be noted that during the transient heating step, the bottom electrodes (usually #1-2) may be activated. As discussed in Section 5.4.3, this is caused by the thermal expansion of liquid sodium.

$$t_{wait}/t_{tot} = L_{elec} \Bigg/ \left(\frac{1}{A_c} \int_0^{t_{tot}} \left(\frac{\dot{m}}{\rho_l} \right)_{up} dt \right) \tag{5.20}$$

5.4 Capillary Pumping Experiment Results

5.4.1 Capillary Pumping Experiment with a Thermally Conducting Porous Insert

The results of an experiment using the copper porous insert with a copper sleeve are plotted in Figure 5.6. This experimental run took about 4.5 hours to reach thermal steady-state. As shown in Figure 5.6a, during the transient heating step there was a single 1.5-hour period where $T_{out} > T_{evap}$ and the mass flowrate was in the reverse direction (*i.e.*, negative). The temperatures were flipped to the proper orientation around 3.5 hours into the experiment, and the mass flowrate was then increased to approach the $\dot{m}_{max}$ estimated with the conjugate transport model introduced in Section 5.2. Due to the small flowrates, the experiment operates in a quasi-steady regime during this transient heating step. This experiment operated for t_{tot} = 190 hours, and in that time all five electrodes where activated (Figure 5.6b), indicating that electrical contact was established between the battery (3V) and the liquid sodium flowing through the electrode prism. The signal for electrode #2 is erratic, first increasing to about 1.5V, then decreasing to practically zero, and finally increasing sharply to 3V. These types of signals were common throughout several experiments because the cement used to mount the electrodes onto the prism deteriorates over time. This leads to partial discharge as a localized dielectric breakdown occurs in the larger cracks and voids due to deterioration. The resulting shunt currents through the cement generate the unusual voltage signals. However, the flow measurement is binary; either electrical contact exists at 3V, or it does not. Thus, an electrode is only considered

to be activated once its voltage reaches the maximum steady-state value. Oxygen impurities in the glovebox (see Section 4.2.2) will oxidize the liquid sodium in the upper flange during the experiment, which alters the liquid sodium electrical conductivity. However, this reduction in electrical conductivity does not ultimately affect the contact between the sodium and the electrodes, and it does not account for the noise in the voltage signals. The maximum voltage decreases slightly (< 0.2V) throughout the experiment. This is caused by the discharging of the 3V battery, and it is normal for long duration experimental runs.

Figure 5.6c shows the upper plenum pressure as a function of time. The upper plenum was not pressurized with argon during this run. Rather, the static pressure of sodium provided the pressure difference between while the evaporator was maintained at P_{atm}. The circular markers in Figure 5.6c represent the static pressure of the liquid sodium column in the upper flange based on the electrode positions, and the dashed line is a linear regression curve. The measured mass flowrate is 0.089 ± 0.032 mg/h for a pressure difference as high as 205.1 Pa ± 1 Pa. This mass flowrate is calculated using the geometric average sodium density between the temperature of the top of the electrode prism and T_{out}. The total mass flowrate uncertainty is conservatively determined by considering the uncertainty in the heights and diameters within the flow path (± 0.13 mm based on machining tolerances), the uncertainty of the activation time (± 1 h), and the uncertainty in the density (± 3 kg/m^3). The effect of thermal expansion is also accounted for (see Section 5.4.3). The maximum/minimum band for the mass flowrate was calculated, and the uncertainty follows the recommendation in the NIST Technical Note 1297 for data uniformly distributed within a band that practically represents 100% of the possible values.[156] The gauge pressure uncertainty is based on the values for the height and

density used in the previous calculation. Figure 5.6d plots T_{evap}, T_{in}, and T_{out} throughout the duration of this experiment. The difference in T_{out} between the activation times of electrodes #1-2, #2-3, and #3-4 are 0.1 °C, 1.7 °C, and −1 °C respectively. The activation of electrode #5 was possibly triggered by a sodium leak (see Section 5.4.3), so it is not considered in the analysis.

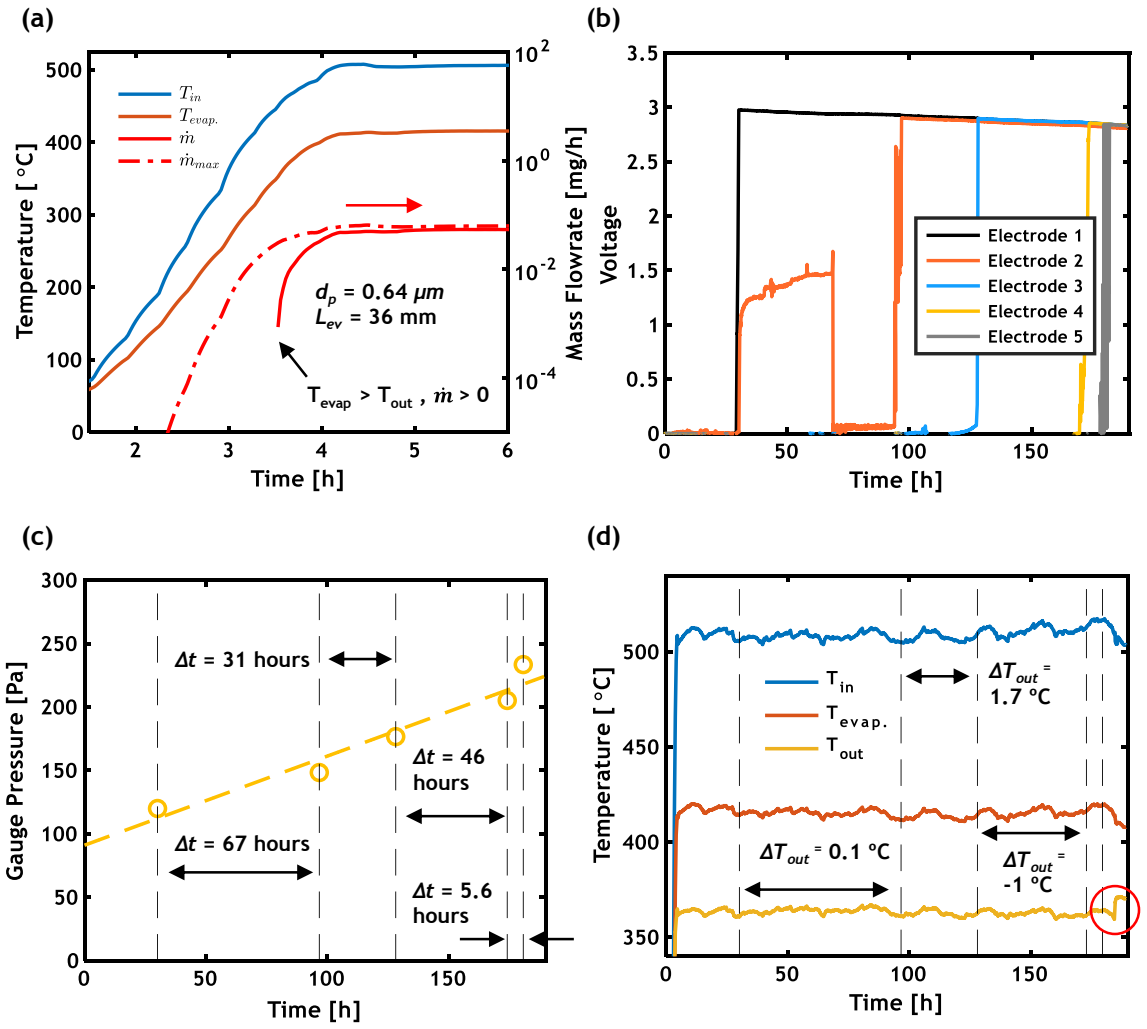

Figure 5.6 (a) Temperature and estimated mass flowrate during the transient heating step of the experiment. Values of d_p = 0.64 μm for the porous coupon and L_{ev} = 36 mm for the evaporator diffusion length are used to find $\dot{m}_{max}$. (b) Activation of each electrode as a function of time. (c) Gauge pressure (between the upper and evaporator plenums) as a function of time. The gauge pressure in this experiment was generated by the static pressure head of liquid sodium, which continuously increased as the sodium was pumped. The

vertical lines correspond to the activation times of each electrode. (d) T_{in}, T_{evap}, and T_{out} as a function of the experiment time. The difference in T_{out} between the activation of successive electrodes is recorded. The red circle shows a sudden rise in T_{out}, during which it is suspected that sodium began to leak from the electrode cement. Since the exact time of this leak is unknown, data from electrode #5 is discounted.

5.4.2 Capillary Pumping Experiment with a Thermally Insulating Porous Insert

A different limiting behavior is expected if the porous insert is an insulating material instead of a thermally conducting one. In this scenario, most of the temperature drop occurs in the porous insert, so the maximum mass flowrate is significantly limited if $S < 1$ is imposed within the porous coupon. However, the experiment can be modified by allowing for the possibility of the condensation interface to form inside the porous coupon ($S > 1$) rather than strictly at $x = L_{ex}$. If the condensation interface shifts downward into the porous coupon, the maximum mass flowrate is now limited by slope of P_w at $x = L_{ex} - L_{pc}$ rather that at $x = L_{ex}$. This new operation mode can theoretically increase the mass flowrate as long as sodium continues to preferentially condense at the original interface ($x = L_{ex}$), rather than within the porous coupon where pumping would be delayed. This condition is maintained when the supersaturation inside the porous coupon is below the kinetic limit for the heterogeneous nucleation of liquid droplets.[121] Therefore when using a thermally insulating porous insert, diffusion ideally occurs between the evaporator and the original condensation interface, but the maximum mass flowrate is limited by the slope of P_w at $x = L_{ex} - L_{pc}$ rather than at $x = L_{ex}$. However, the condensation interface may now form within the porous coupon where $S \approx 2\text{-}4$.

A few experiments were carried with a thermally insulating porous insert using vitreous carbon (φ = 97%, τ = 3) from ERG Aerospace Corp. with an effective thermal

conductivity of k_{eff} = 0.16 W/m/K (k_s = 5 W/m/K for bulk vitreous carbon). Figure 5.7 shows the results of one of these successful runs. This experimental run took about 7 hours to reach thermal steady state. As shown in Figure 5.7a, during the transient heating step there were three separate periods, totaling ≈ 3 hours, where $T_{out} > T_{evap}$ and the mass flowrate was in the reverse direction (*i.e.*, negative). The temperatures were flipped to the proper orientation around 4.6 hours into the experiment. Two $\dot{m}_{max}$ limits are plotted in Figure 5.7a, one for the conductive porous insert model which assumes that $\dot{m}_{max}$ is determined by the slope of P_w at $x = L_{ex}$, and one for an insulating porous insert with $\dot{m}_{max}$ determined at $x = L_{ex} - L_{pc}$ as described in the preceding paragraph. Both of these limits are estimated with the conjugate transport model introduced in Section 5.2. This alternative experiment is designed to significantly exceed the conductive $\dot{m}_{max}$ limit for this porous insert, and instead allow the mass flowrate to approach the insulating $\dot{m}_{max}$ limit. This experiment lasted for t_{tot} = 142 hours, and in that time four of the five electrodes where activated (Figure 5.7b) indicating that electrical contact was established with the liquid sodium flowing through the electrode prism. The voltage signals were especially noisy during this run. As described in Section 5.4.1, this is caused by the deterioration of the Omegabond 600 cement due to many heating/cooling cycles over several experiments. Nevertheless, because this method of flow measurement is binary, the electrodes were only considered fully activated when the voltage signal reached the maximum value. In Figure 5.7b, the decrease in this maximum voltage due to the discharging of the battery is evident (maximum of 2.1 V, ≈ 0.5 V drop during the experiment).

The upper plenum was pressurized with argon during this experimental run, and Figure 5.7c shows the pressure as a function of time, measured with an MKS 631D

Baratron pressure transducer. The activation of electrode #1 occurred during the transient heating of the experiment and was triggered by thermal expansion. Thus, only the differences in T_{out} between the activation times of electrodes #2-3 and #3-4 are considered in this analysis, which are −1 °C and 1.6 °C respectively (see Figure 5.7d). The measured mass flowrate is 0.21 ± 0.17 mg/h for a pressure difference between 0.2 kPa < P < 7.25 kPa. The mass flowrate is calculated the same way discussed in Section 5.4.1. The uncertainty in the upper plenum pressure is due to the intrinsic instrument error and noise, the variation in glovebox pressure over time, and the possible presence of a clog in the argon pressurization line discovered weeks after this experiment. This potential clog sets a lower limit to the gauge pressure equivalent to the liquid column static pressure. These sources of errors are added/subtracted to establish a maximum/minimum band, and the pressure uncertainty follows the recommendation in the NIST Technical Note 1297 for data uniformly distributed within a band that practically represents 100% of the possible values.[156]

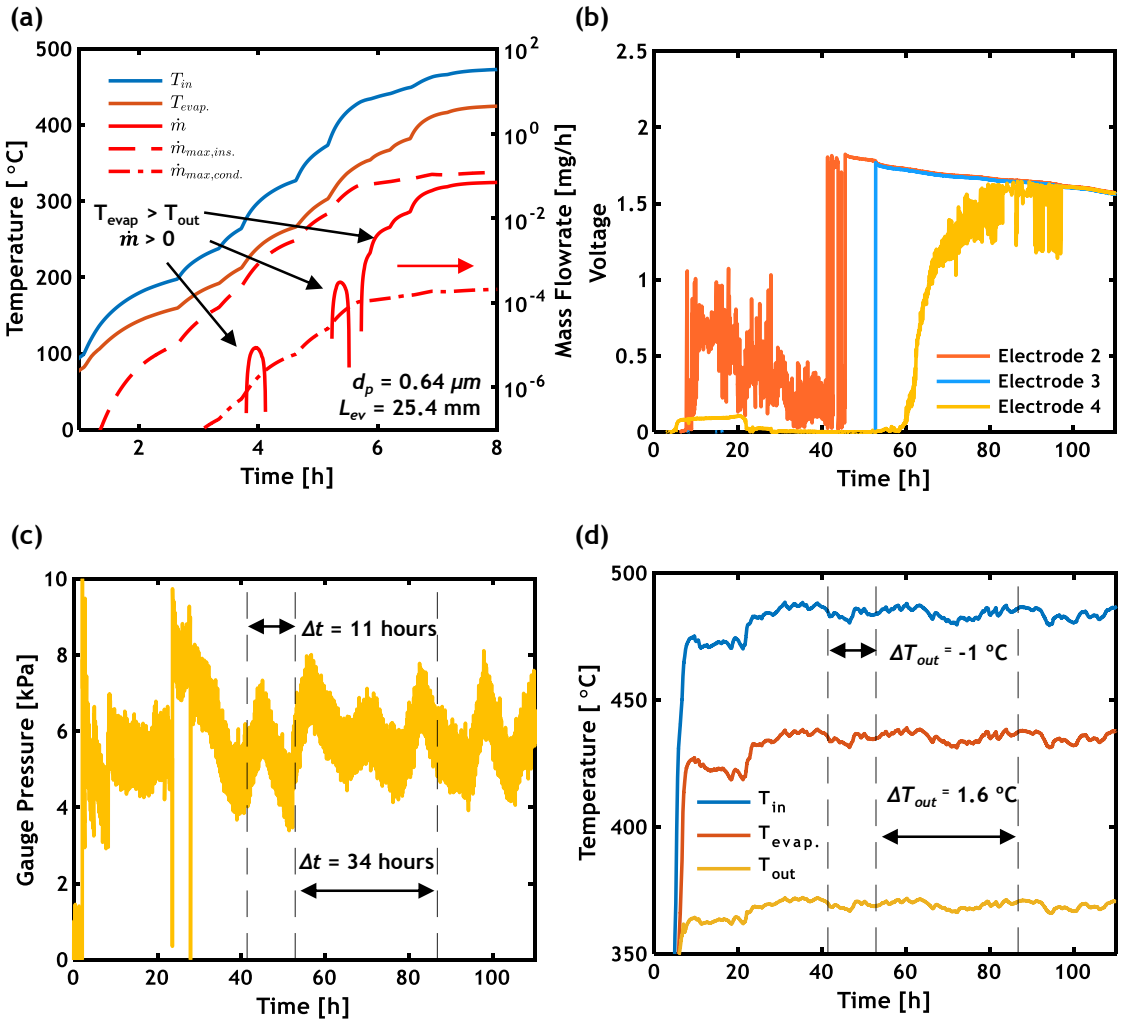

Figure 5.7 (a) Temperature and estimated mass flowrate during the transient heating step of the experiment. Values of d_p = 0.64 μm for the porous coupon and L_{ev} = 25.4 mm for the evaporator diffusion length are used to find $\dot{m}_{max}$ for conductive and insulating porous inserts. (b) Activation of each electrode as a function of time. Electrode #1 was activated due to thermal expansion during the transient heating, so the signal is removed to improve clarity. Electrode #5 was not activated, presumably due to an internal electric connectivity issue. (c) Gauge pressure (between the upper and evaporator plenums) as a function of time. The vertical lines correspond to the activation times of each electrode. (d) T_{in}, T_{evap}, and T_{out} as a function of time. The difference in T_{out} between the activation of successive electrodes is recorded.

5.4.3 Analysis of Experimental Results

It is necessary to consider if another phenomenon can explain the activation of the electrodes in these two experiments. First, the thermal expansion of liquid sodium in the upper plenum is analyzed. An initial mass of sodium is added in the upper plenum to create the condensation interface. As the experiment is heated, this sodium will melt and fill the internal flow volume in the upper plenum (Figure 5.8a) as its density decreases with temperature. Due to this thermal expansion, the lower electrodes are often activated while the assembly is still ramping up to steady-state temperature. Therefore, the activation of electrodes cannot be immediately assumed to be caused by sodium pumping. The internal volume in the upper plenum up to electrode #1 is V_1 = 337 mm^3, and the difference in volume between successive electrodes is $\Delta V \geq 2.47$ mm^3. For thermal expansion to fully account for the activation between electrodes $n \rightarrow m$ (where $1 \leq n < m \leq 5$), a reduction in density $\rho_n \rightarrow \rho_m$ is needed for the corresponding change in volume $(m - n)\Delta V$ to manifest. Equation 5.21 is used to calculate the density ratio ρ_n / ρ_m required for thermal expansion to yield this change in volume. Figure 5.8b shows the change in temperature required for sodium to thermally expand by volume $(m - 1)\Delta V$ and activate electrode m when starting from $n = 1$. The lower limit for each band is a conservative uncertainty where V_1 is assumed to be 5% larger, the density is assumed to be 0.3% larger (based on the property functional uncertainty), and the smallest possible value for ΔV is applied. For both experiments, the temperature differences between electrode activations are an order of magnitude smaller than what is predicted by the lower limits in Figure 5.8b. Therefore, according to this conservative thermodynamic model, thermal expansion does not fully account for the liquid movement in these experiments.

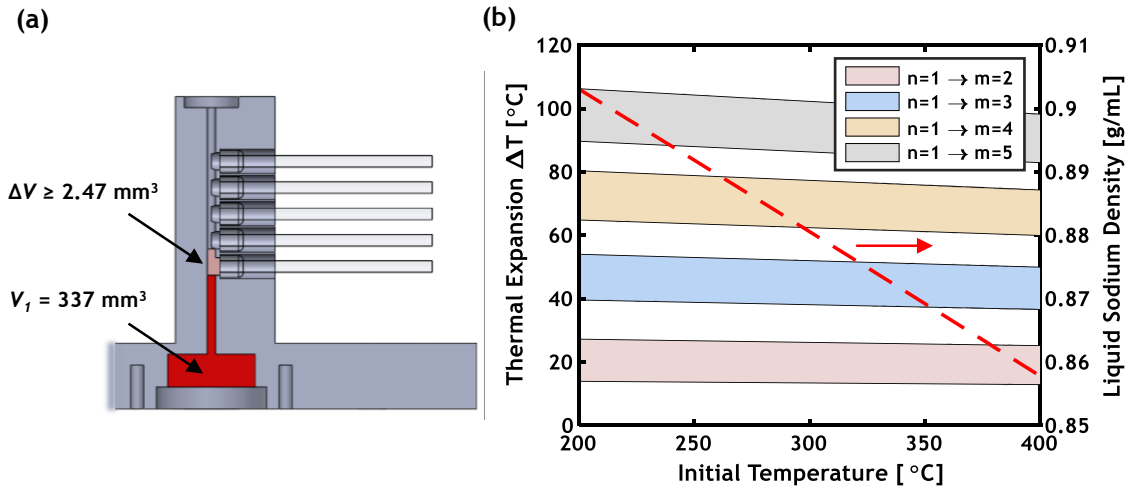

Figure 5.8 (a) Interior of the upper plenum depicting the volume up to electrode #1 (V_1) and the difference in volume between successive electrodes (ΔV). (b) Temperature difference required for liquid sodium to thermally expand by a volume of (m-1)ΔV as a function of the initial temperature. The lower limit for each band conservatively assumes that V_1 is 5% larger and the liquid density is 0.3% larger.

$$\left(V_1+\left(n-1\right)\Delta V\right)\left(\rho_n/\rho_m-1\right)\le\left(m-n\right)\Delta V \tag{5.21}$$

The transport could also result from a larger pressure in the evaporator plenum due to temperature fluctuations during steady-state, occurring after the evaporator relief valve remains closed. Generally, the pressure increase due to these fluctuations is smaller than the argon pressure in the upper plenum, but for the experiment discussed in Section 5.4.1 only the liquid static pressure head provided the gauge pressure. If the pressure in the evaporator plenum is assumed to increase based on the evaporator plenum temperature fluctuations (≈ 5 °C), the mass flowrate would be 5-6 orders of magnitude larger than what was measured. The voltage signals would result from viscous transport of the liquid slug in the upper plenum, rather than diffusive transport of the sodium vapor. Furthermore, at these temperatures the fittings in the assembly tend to leak, further stabilizing the

evaporator pressure with the atmosphere. Thus, this mechanism is unlikely to have contributed to the sodium transport. Finally, since an electrical potential (3V) is applied between the sodium and the electrodes to detect flow, the possibility that electrowetting accounts for the movement of sodium was also considered. The wetting properties of a fluid can be modified through electrowetting as the interfacial tension changes due to an induced electric potential. This effect manifests when charge builds up in a capacitor, typically in an electric double layer between a metal and an electrolyte or across a dielectric.[157] Following the Young-Lippman equation, electrowetting is only significant when the dielectric layer is very thin. In this experiment, electrowetting can only be substantive as the sodium approaches the electrodes in the upper flange. However, once the electrical circuit is established, charge can no longer be stored and the electrowetting (if it was present at all) would be reversed immediately.[158] Thus, electrowetting cannot explain the movement of sodium in these experiments. Without an alternative explanation for the activated voltage signals, these experimental results show promise towards demonstrating the feasibility of this capillary pumping mechanism. However, more experimental data at higher pressures are needed before a definitive conclusion is established.

More than 20 experimental runs were attempted with both conducting and insulating porous inserts, and several issues were observed that merit further discussion. Most notably, replication of successful experimental results (*i.e.*, activation of successive electrodes over a time frame consistent with diffusive mass transport) proved challenging, even though experimental conditions were identical. The major cause of unsuccessful runs is sodium condensation somewhere within the experimental assembly outside of the

prescribed liquid sodium interface, thereby hindering the ability for sodium to be pumped. Clumps of sodium were found in the porous inserts after post-processing several experimental coupons (Figure 5.9a). In many unsuccessful runs, sodium was also observed in the tube connecting the evaporator plenum to the relief valve, which indicates inadequate heating. The reasons for this undesired condensation are numerous: not enough superheating of the evaporator plenum, the experimental coupon, nor the evaporator relief valve; thermocouples were not properly inserted, leading to inaccurate temperature measurements; or the mass flowrate exceeded the maximum allowable limit. The deterioration of the Omegabond 600 cement used to mount the electrodes is also a concern. In a couple of runs, there was a visible leak of sodium through this cement. Even in the successful run discussed in Section 5.4.1, sodium leaked from the cement around hour 185, causing a sudden rise in the temperature (see Figure 5.6d). In yet another run, a high temperature cobalt-based solder used to connect the relief valve to the evaporator started to leak. This prompted a design change to using a weld connection instead of the solder. Another interesting observation during post-observation is that the sodium in the upper plenum is often "missing" (Figure 5.9b), even after successful runs (such as the one discussed in Section 5.4.1). The exact reason for this missing sodium remains unclear. For some runs, the overpressure in the upper flange may have surpassed the breakthrough pressure of the porous coupon (due to a high T_{out}), thereby allowing sodium to flow down into the evaporator. In other runs this is not plausible given the activation of the electrodes, and their subsequent deactivation during cooldown. It is proposed that the breakthrough pressure in these cases may have been surpassed during cooldown, after the experiment

was concluded. The exact reason for this observed phenomenon will be studied in future experiments.

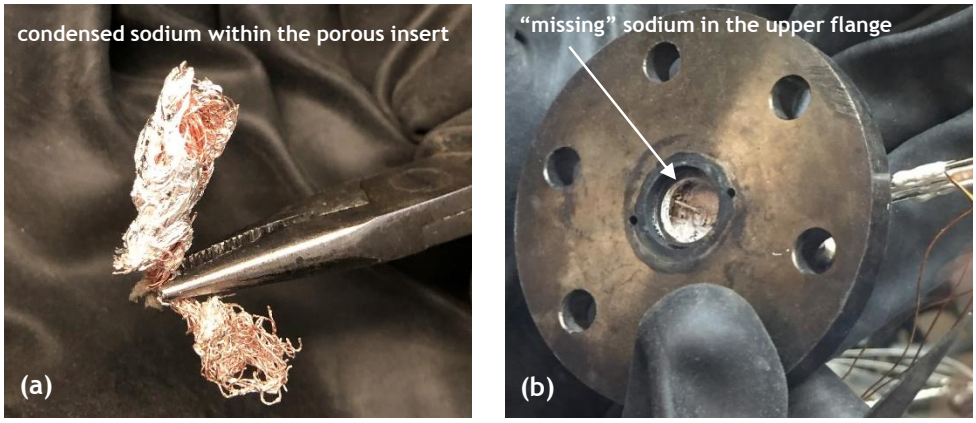

Figure 5.9 (a) Sodium condensation on a copper mesh (used as the porous insert in earlier experimental iterations). The silver colored spots on the brown copper are solidified sodium. (b) Sodium observed missing from the upper flange after an experiment. This is most likely caused by the sodium breakthrough pressure being exceeded, either during the experiment or during its cooldown.

5.5 Summary

In this chapter, an experiment used to demonstrate the feasibility of capillary pumping of liquid sodium using a non-wetting porous structure was discussed. This pump requires the condensation of sodium inside a non-wetting porous structure ($\theta_{ca} > 90^o$), such that the force generated at the solid-liquid-vapor interface transports condensed sodium from a low-pressure vapor into a high-pressure bulk liquid. This process is the reverse of a traditional capillary wick, where sodium is transported from a low-pressure liquid into a higher pressure vapor region through evaporation on a wetting porous structure ($\theta_{ca} < 90^o$). After introducing the design of the experiment, a conjugate transport model was developed to determine the mass flowrate and the temperature distribution in this experiment. It was shown that the one-dimensional Fick's law characterizes the diffusion of sodium vapor in

this experiment well, and that the temperature distribution relies on conduction heat transfer through a quiescent medium. The maximum allowable mass flowrate is determined with this transport model, which guides the operating temperatures for the experiment.

The results of two preliminary pumping experiments were discussed in detail. The first used a thermally conducting porous insert to force the majority of the temperature drop to occur adjacent to the condensation interface. A mass flowrate of 0.089 ± 0.032 mg/h for a pressure difference as high as 205.1 Pa ± 1 Pa was measured. The second experiment used a thermally insulating porous insert, which has the potential to increase the mass flowrate by allowing for the supersaturation of sodium vapor to exceed a value of one inside the porous coupon. For this run, a mass flowrate of 0.21 ± 0.17 mg/h for a pressure difference between 0.2 kPa < P < 7.25 kPa was measured. Several experimental issues have prevented the consistent replication of these results. Most notably, sodium condensation occurring in undesired locations during the experiment proved to be the most deleterious towards successful pumping demonstrations. Many of the experimental issues were addressed through design iterations. By discounting several alternative explanations for the transport of sodium, it is argued that these results show promise towards demonstrating the feasibility of the capillary pumping mechanism. However, additional results at higher pressures are necessary before this mechanism is unambiguously confirmed.

CHAPTER 6. CONCLUSION

As the need for distributed power increases due to rising global residential energy demand, the sodium thermal electrochemical converter (Na-TEC) can have a transformative effect on micro-CHP systems in the 1-10 kW scale. The Na-TEC is an electrochemical heat engine that generates electricity through the isothermal expansion of sodium ions through a β"-alumina solid-electrolyte. Thermal management limitations have constrained previous single-stage devices to thermal efficiencies below 20% despite larger theoretical limits. A dual-stage Na-TEC takes advantage of regeneration and reheating steps, and is amenable to improved thermal management through a reduction of parasitic losses. This dissertation discusses the operating limits of a dual-stage Na-TEC, and a design to minimize thermal parasitic losses. Another challenge for this device is the pumping of liquid sodium. Pumping has traditionally been accomplished with wicking structures in the evaporator, but these can suffer from long-term degradation in the high-temperature operating environment. This dissertation also explores the feasibility of using a non-wetting porous structure in the condenser to enable low-temperature capillary pumping solutions. Section 6.1 summarizes the key scientific findings from this dissertation, and Section 6.2 addresses some of the future research that can be pursued to build upon this work.

6.1 Thesis Questions

The unique intellectual contributions from this dissertation can be summarized by answering the following thesis questions:

i. What are the thermodynamic operating limits for a dual-stage Na-TEC?

Assuming that common electrode materials are employed for the dual-stage Na-TEC, a simple heat transfer model introduced in Chapter 2 is used to estimate the total parasitic heat loss. With this model, the practical efficiency of a dual-stage Na-TEC is shown to approach 26.5%, which is 7.5% points larger than the highest reported efficiency of a single-stage Na-TEC, while the maximum power density approaches 2.22 kW m^{-2}. The maximum power density and the thermal efficiency are determined by considering thermodynamic, electrochemical, and heat transfer variables. The temperatures at the evaporator, the intermediate plenum, and the condenser define the limits of operation for this technology. The voltage depends on the sodium vapor pressure set by these temperatures, which affects the electrochemical polarizations (Ohmic, kinetic, and mass transfer) in each stage. The maximum power density is then determined through optimization with the independent operating variables (*i.e.*, current density and area-ratio between stages). The dual-stage Na-TEC is limited by the irreversibilities that arise from using two electrochemical stages, so it is less practical for high-power applications than a single-stage Na-TEC. The thermal efficiency, however, is most sensitive to the thermal parasitic heat losses in the single- and dual-stage device. These losses can be smaller in a dual-stage Na-TEC due to the lower average temperature for bypass heat transfer (*i.e.*, radiation and conduction directly to the condenser).

ii. To what degree can a reduced-order model be used to effectively design a dual stage Na-TEC to operate at the maximum practical efficiency?

A reduced-order modeling approach, in conjunction with the thermodynamic model discussed in Chapter 2, can be used to analyze the thermal performance of a dual-stage Na-TEC in the early stages of design, guide the selection of materials, and determine the total system size, all while consuming minimal computational resources and maintaining acceptable accuracy. A maximum efficiency of 29% and a maximum power output of 125 W can be achieved with the quasi-axisymmetric dual-stage Na-TEC design presented in Chapter 3. This design is evaluated using a reduced-order finite-element model. Since the efficiency is mostly affected by the thermal parasitic losses, this design uses a vanadium housing and a SS 316 condenser to decrease these losses. The reduced-order model incorporates effective thermal conductivities to account for complex corrugated geometries, and apparent surface emissivities to accommodate the effect of radiation shields. Furthermore, an analytical model is developed to account for conduction bypass through the Na-TEC liquid-return path. The thermal performance of the design is analyzed, using an iterative procedure between the finite-element and thermodynamic models.

iii. What temperature-dependent interfacial pressures can be generated between a stainless-steel porous structure and liquid sodium?

A breakthrough pressure experiment was built to determine the temperature-dependent interfacial pressures that can be generated between liquid sodium and a SS 316L porous structure. Since liquid sodium is non-wetting ($\theta_{ca} > 90^{o}$) to SS 316 at low temperatures, the sodium is incrementally pressurized during the experiment until it

overcomes the interfacial force at the solid-liquid-vapor contact line (*i.e.*, breakthrough pressure) and begins flowing through the experimental coupon. This coupon consists of a porous structure (0.1 μm < d_p < 4.14 μm, φ = 25%) fitted inside a SS 316 cylinder. Electrodes are placed downstream from the experimental coupon to detect the flow of sodium once the breakthrough pressure is exceeded. The highest interfacial pressure recorded is 92.6 ± 5.8 kPa at a temperature of 207 ± 1 °C. The interfacial pressure monotonically decreases with temperature up to the wetting transition temperature, following a general breakthrough pressure function. This function can be determined analytically for simple geometries (*e.g.*, straight capillaries, packed spheres). The wetting transition temperature is linearly extrapolated from the experimental data to 411.6 ± 5.3 °C. There are several sources of uncertainty in this experiment, which are reflected in the error bars for the pressure data. The results from this experiment, and their uncertainty, are discussed in Chapter 4.

iv. To what degree (pressure head and discharge rate) can passive liquid-sodium pumping be maintained through the condensation of sodium vapor within a non-wetting porous structure?

An experiment was built to determine the feasibility of pumping sodium by allowing it to condense within a non-wetting porous structure. As sodium condenses, it is transported from the low-pressure vapor into a higher pressure bulk liquid by the force generated at the solid-liquid-vapor interface. Two successful experiments are discussed in Chapter 5: one using a thermally conducting porous insert with a mass flowrate of 0.089 ± 0.032 mg/h against a pressure head of P < 205.1 ± 1 Pa, and another using a thermally insulating porous insert with a mass flowrate of 0.21 ± 0.17 mg/h against a pressure head of 0.2 kPa < P <

7.25 kPa. By discounting several alternative explanations for the transport of sodium, it is argued that these results show promise towards demonstrating the feasibility of the capillary pumping mechanism. However, more experiments at higher pressures are ultimately needed before making a conclusive determination. This experiment uses an experimental coupon, consisting of the SS 316L porous structure and a porous insert, to support the capillary pumping. An initial supply of sodium is added on top of the porous coupon to create the condensation interface. During the experiment, sodium vapor diffuses through an evaporator plenum and condenses at this interface. For this capillary pumping mechanism to succeed, sodium should not condense elsewhere inside the experimental coupon. Thus there is a maximum allowable mass flowrate for the sodium vapor, which is estimated using a conjugate transport model.

6.2 Future Work

The next step is to build a full-scale dual-stage Na-TEC prototype to determine if its thermal efficiency can surpass that of previous single-stage prototypes ($\eta \leq 19\%$). A preliminary, open-loop, dual-stage module has already been built and tested to satisfy the DOE Apollo SunShot program objectives. Planar β''-alumina disks from Ionotec Ltd. were used for each stage and were mounted inside a SS-253 MA housing (Figure 6.1a). Power vs. current measurements were gathered for these dual-stage modules at low temperatures; a maximum power of 183 μW was generated when operating at T_{evap} = 604 °C, T_{int} = 359 °C, and T_{cond} = 227 °C (Figure 6.1b). One of the technical challenges that hinders higher temperature operation is the lack of a reliable high-temperature metal to ceramic seal for the β''-alumina disks. An aluminum-based thermocompression bond was used to create a seal in each stage for this module, but its efficacy was limited to temperatures below 650

°C. An air braze with Ag-8CuO brazing alloy has shown promise at higher temperatures, but more extensive testing is necessary before it can be used in a prototype.[159] In future design iterations, this module must also be optimized to reduce thermal parasitic losses. Furthermore, a liquid return path needs to be incorporated into the design to create a full, closed-loop prototype. The thermal efficiency of such a closed-loop prototype can then be compared to previously built single-stage devices.

The reduced-order thermal model introduced in Chapter 3 can also be refined in future studies. Most importantly, the effect of sodium pressure drops from various components in the design should be addressed. For example, the thermal efficiency can be optimized as a function of the length of the corrugated structure in the condenser, given that a longer corrugated path reduces parasitic heat conduction but increases the sodium vapor pressure drop. Thus far, none of the component pressure drops (*i.e.*, ΣP_{loss}) have been incorporated into the reduced-order model. Moreover, a Na-TEC prototype would provide information on more detailed features of the design (*e.g.*, thermal contact resistance, heat transfer to the environment through insulation) that can be added to the model.

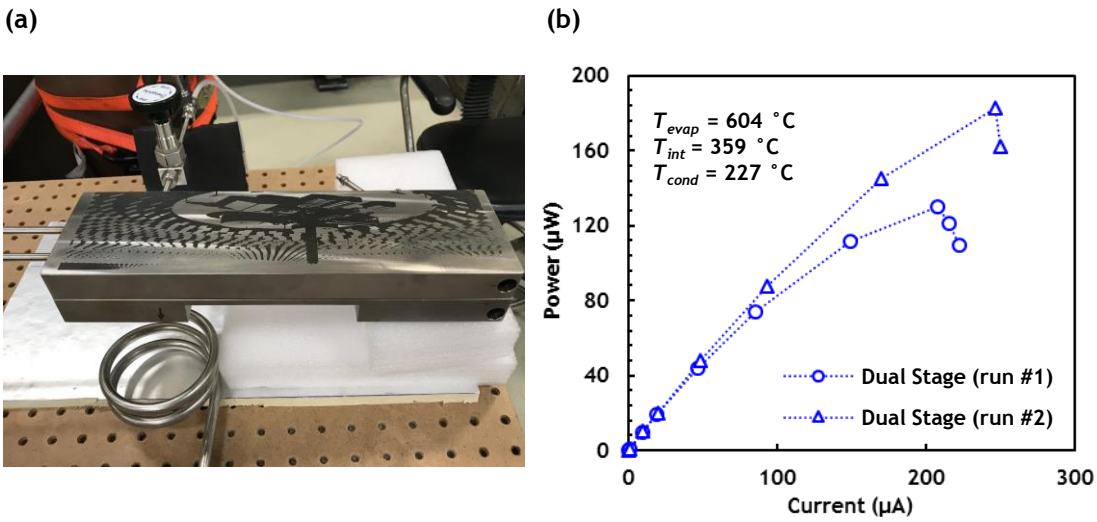

Figure 6.1 (a) Picture of an open-loop dual-stage Na-TEC module. The spiral tube is connected to a vacuum pump to promote a low pressure in the condenser. (b) Power vs. current for one of the dual-stage Na-TEC modules (total electrolyte area: 39.3 cm^2).

Additional work must be undertaken to build a low-temperature capillary pump using a non-wetting porous structure. Before conducting more of the experiments discussed in Chapter 5, a second law analysis of the capillary pumping mechanism is recommended. The entropy generation in this experiment can be calculated using similar techniques applied to heat pipes, where the irreversibilities between the evaporator and the upper flange arise from heat transfer through finite temperature differences, diffusion of sodium vapor, and frictional losses due to fluid transport (negligible in this experiment).[160, 161] By following similar analyses used for evaporation interfaces in microchannels [162], an optimization study can be performed to minimize entropy generation across the condensation interface through a parametric sweep of temperature, pressure, pore size, porosity, and local mean curvature. Once thermodynamically favorable conditions are established, more capillary pumping experiments can be conducted to expand upon the limited results reported herein. These experiments should be conducted at higher pressures

to fill in a pump curve (pressure head vs. discharge rate), which effectively delineates the pumping limits. A pump curve, in conjunction with an appropriate system curve, can be used to design a pump for a dual-stage Na-TEC. Future experiments should also continue to explore the difference between using thermally conducting and thermally insulating porous inserts. One practical experimental improvement is to find a more robust electrically insulating material to mount the electrodes onto the upper flange. Although the high-temperature cement has worked satisfactorily, its degradation increases the uncertainty in the voltage signals used to verify the flow of sodium. Finally, the alternative explanations to sodium pumping discussed in Section 5.4.3 can be tested by performing additional experiments. A limited experimental effort using the capillary pumping assembly (see Figure 5.5) has already been undertaken to validate the thermal expansion model. The initial results generally agreed well with the model, but there was one outlier where the temperature difference between electrode activations was much smaller than the model predictions. Explanations for this outlier are speculative, so further experiments beyond this limited effort are merited to understand what caused it.

The conjugate transport model used to guide these experiments can also be improved. For example, radiation inside the porous structures can be incorporated into the model to determine a more accurate temperature distribution inside the experimental coupon. A parametric study can also be used to optimize the diameter and height of the experimental coupon while allowing for convection on its outer surface. Finally, if a high-temperature vacuum seal can be developed for SS 316, this experiment can be done under vacuum. The upper plenum would be left open to the atmosphere while different vacuum pressures are enforced in the evaporator plenum. Instead of binary diffusion, the sodium

vapor would be limited by viscous transport and natural convection in the rarefied and transitional gas regimes.

Finally, other materials can be considered for the proposed capillary pump, and the breakthrough pressure experiment can characterize the pumping limits for new coupons. To reduce the experimental uncertainty, an ultra-conservative wait time ($> 2 \cdot t_{wait}$) can be employed between pressure increments. Furthermore, to prevent sodium leaks between the boundary of the porous coupon and the SS 316 cylinder, a micro-weld can be implemented around the edge between these two. An even tighter boundary seal can be achieved by directly sintering a metal powder inside the cylinder. The temperature-dependent liquid sodium contact angle can also be measured separately with a sessile drop experiment. This data can help troubleshoot the large breakthrough pressure variability measured with this experiment. To reduce the uncertainty in the permeability measurements, the breakthrough pressure experiment can be supplemented by other experimental techniques, such as measuring the saturation of the structure through porosimetry.

APPENDIX A. VIEW FACTOR BETWEEN WALLS IN THE ZONE 3 CORRUGATED UNIT

The Zone 3 corrugated walls described in Chapter 3 can be treated as a network of linear radiation shields. The view factor between each radiation shield is found by considering that the radiation exchange occurs between an annulus to another coaxial annulus of the same outer radius. Both annuli have a radiation blocking coaxial cylinder on their inner radius. The view factor between two faces with this geometry is found using Equation A.1.[91]

$$F_{1-2}=\frac{1}{\pi A}\left[\begin{array}{l}\frac{A}{2}cos^{-1}\frac{R_c}{R_2}+\frac{B}{2}cos^{-1}\frac{R_c}{R_1}+2R_c\left(tan^{-1}Y-tan^{-1}A^{1/2}-tan^{-1}B^{1/2}\right)\\ -\left[\left(1+C^2\right)\left(1+D^2\right)\right]^{1/2}tan^{-1}\left[\frac{\left(1+C^2\right)\left(Y^2-D^2\right)}{\left(1+D^2\right)\left(C^2-Y^2\right)}\right]^{1/2}\\ +\left\{\left[1+\left(R_1+R_c\right)^2\right]\left[1+\left(R_1-R_c\right)^2\right]\right\}^{1/2}tan^{-1}\left\{\frac{\left[1+\left(R_1+R_c\right)^2\right]\left(R_1-R_c\right)}{\left[1+\left(R_1-R_c\right)^2\right]\left(R_1+R_c\right)}\right\}^{1/2}\\ +\left\{\left[1+\left(R_2+R_c\right)^2\right]\left[1+\left(R_2-R_c\right)^2\right]\right\}^{1/2}tan^{-1}\left\{\frac{\left[1+\left(R_2+R_c\right)^2\right]\left(R_2-R_c\right)}{\left[1+\left(R_2-R_c\right)^2\right]\left(R_2+R_c\right)}\right\}^{1/2}\end{array}\right] \quad \text{(A.1)}$$

$R_1=r_1/h\,,R_2=r_2/h\,,R_c=r_c/h$

$A=R_1^2-R_c^2$

$B=R_2^2-R_c^2$

$C=R_2+R_1$

$D=R_2-R_1$

$Y=\sqrt{A}+\sqrt{B}$

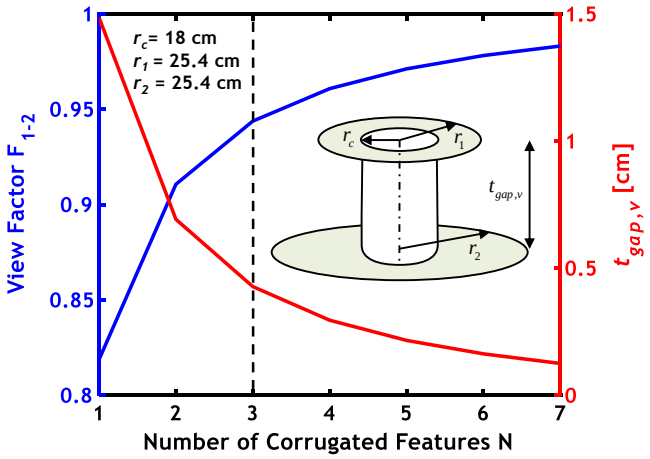

Figure A.1 Radiation view factor between the walls of the Zone 3 corrugated unit (annulus to another coaxial annulus of the same outer radius).

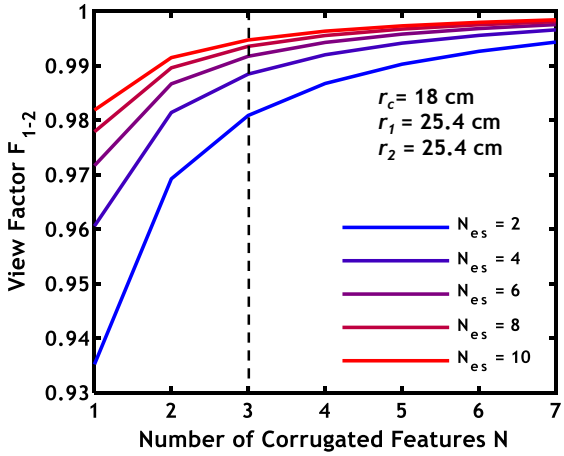

Figure A.2 Radiation view factor between the external shields added in the Zone 3 corrugated unit (annulus to another coaxial annulus of the same outer radius).

APPENDIX B. VIEW FACTOR BETWEEN THE ZONE 4 CYLINDRICAL SHIELDS

The view factor between the cylindrical shields used in Zone 4 (discussed in Chapter 3) is found by considering that the radiation exchange occurs between the exterior of an inner right-circular cylinder of finite length to the interior of an outer right-circular cylinder of finite length.[91] The view factor between two faces with such geometry is found using Eq. S7. The view factor occurs between the two bounding Zone 4 cylindrical shields at $r_a = r_1 = 17.3$ cm and $r_b = r_2 = 17.8$ cm, both with height H = 6.2 *cm*, is 0.927. Thus, the view factor can be reasonably approximated as unity, especially as more cylindrical shields are added between these two bounding shields, causing the view factor to approach closer to unity.

$$F_{1-2} = \frac{1}{\pi R_1}\left[\begin{array}{l} \frac{1}{2}\left(R_2^2 - R_1^2 - 1\right) cos^{-1}\frac{R_1}{R_2} + \pi R_1 - \frac{\pi}{2} AB \\ \quad -2R_1 tan^{-1}\left(R_2^2 - R_1^2\right)^{1/2} + \\ \left\{\left(1+A^2\right)\left(1+B^2\right)\right\}^{1/2} tan^{-1}\left\{\frac{\left(1+A^2\right)B}{\left(1+B^2\right)A}\right\}^{1/2} \end{array}\right] \tag{B.1}$$

$R_1 = r_1/h$
$R_2 = r_2/h$
$A = R_1 + R_2$
$B = R_1 - R_2$

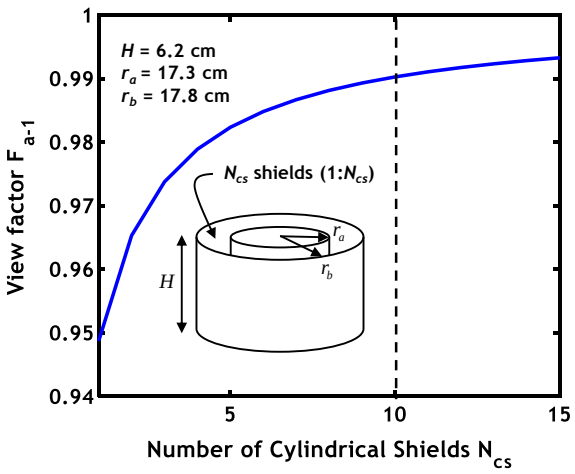

Figure B.1 Radiation view factor between the first two adjacent cylindrical shields (a-1) in Zone 4 (exterior of an inner right-circular cylinder of finite length to the interior of an outer right-circular cylinder of finite length).

.

APPENDIX C. UNCERTAINTY CALCULATION FOR THE SODIUM BREAKTHROUGH PRESSURE EXPERIMENT

The breakthrough pressure data analyzed in Chapter 4 (tabulated in Table C.1) was gathered by two students. Since collecting this data requires some practice, the limited measurements obtained by two other students (which contain outliers) are not included in this analysis due to the students' relative inexperience in running the experiment. There are five sources of uncertainty for each measurement: the pressure transducer instrument uncertainty, the argon glovebox pressure fluctuation, the static pressure fluctuation, the uncertainty resulting from the experiment incremental pressure increase ΔP_{inc}, and the error associated with the wait time between pressure increments. The pressure transducer (MKS 631D Baratron) uncertainty is 0.6% of the measured value according to the manufacturer. The glovebox pressure fluctuation is conservatively estimated to be ± 0.4 kPa. The static pressure uncertainty is caused by the height of the liquid plug, which may be higher/lower (conservatively assumed at ± 2.5 cm) than the height of the porous structure. Next, since the argon pressure during the experiment is increased in increments of ΔP_{inc} = 5 kPa, the true breakthrough pressure value is assumed to lie anywhere in the 5 kPa range below the measured value. Finally, although a conservative wait time was used during each experimental run, the actual wait time required is determined a posteriori for each experiment (see Section 4.1.2). To find a conservative uncertainty, the largest difference between the experiment wait time and the required wait time for each pressure increment is determined. This time difference is subtracted from the absolute time when breakthrough is measured, and the pressure at this new time is recorded. The difference between the

measured breakthrough pressure and the pressure at the corrected time is set as the total error. The error associated with the wait time is the largest source of uncertainty for these measurements. These five errors are added/subtracted from the measured value to establish a maximum/minimum band. The pressure and its uncertainty are then calculated following the recommendation in the NIST Technical Note 1297 for data uniformly distributed within a band that practically represents 100% of the possible values.[156]

The breakthrough pressure experiment is not designed to work in the wetting regime, so the estimate for the wetting transition temperature must be linearly extrapolated from the measured data in the non-wetting regime. For this experiment, the wetting transition occurs in the range where breakthrough pressure is < 5 kPa because this is the smallest pressure increment. A linear extrapolation with two data points surrounding P = 5 kPa is used to estimate this temperature. A Monte Carlo simulation with 10^4 linear extrapolations can estimate the wetting transition temperature by allowing each data point to fluctuate within their respective uncertainties in pressure and temperature. The wetting transition temperature is the mean of these simulations, and the uncertainty is the standard deviation.

The measurement uncertainty for the velocity was determined using a Monte-Carlo approach. The electrode distance (± 0.13 mm for the machining tolerance) and the activation times (± 0.5 s time step) were plotted with their intrinsic uncertainties. The velocity data for a few runs could not be resolved because some electrodes were not activated, the voltage was fluctuating, or the signal was deactivated during the measurement. For some of these runs the velocity could not be resolved, but for the rest these irregularities result in larger uncertainties. Numerous Monte Carlo simulations (10^4)

were undertaken to find the slope of a linear least-squares regression while allowing the data points to fluctuate within their intrinsic uncertainty ranges. The mean velocity is the average of these regression slopes. The velocity uncertainty is composed of two contributions: the standard deviation of all Monte Carlo simulations and the average regression curve error associated with the goodness of fit. The total measurement error is the square root of the sum-of-the-squares of these two contributions, according to standard variance formulas.

For the permeability, the maximum/minimum value is calculated using the highest/lowest input variables (i.e., pressure and velocity measurements, viscosity) based on their standard errors. The permeability is assumed to be normally distributed within this range, which represents a single standard deviation since the errors for the input variables are themselves standardized. Thus, the recommendation from the NIST Technical Note 1297 for normally distributed data containing 67% of the possible values is used for the uncertainty.[156] Finally, the errors for the permeability equations in Table 4.1 are determined by assuming the pore diameters are normally distributed between 0.1 μm < dp < 4.14 μm, and by assuming that this diameter range represents > 99% of the possible values for the pore diameter. The total permeability reported is then average of these values, and it has two associated uncertainties: the standard error found using a Student's T-test statistic, and the propagation of error for the uncertainties of the permeability for each experimental run. The total standard uncertainty is conservatively reported as the square root of the sum of these two contributions.

Table C.1 Breakthrough Pressure Experiment Data

Temperature [°C]	Breakthrough Pressure [kPa]	Darcy velocity [mm/s]	Permeability $\cdot 10^{15}$ [m^2]
207 ± 1	92.6 ± 5.8	0.25 ± 0.02	4.4 ± 0.7
211 ± 1	86.3 ± 4.7	0.23 ± 0.01	4.4 ± 0.6
212 ± 1	82.5 ± 5.9	0.18 ± 0.01	3.4 ± 0.5
240 ± 2	77.4 ± 8	0.12 ± 0.01	2.2 ± 0.4
250 ± 3	79.6 ± 3.2	0.22 ± 0.02	4.3 ± 0.7
252 ± 2	67.9 ± 4.9	0.25 ± 0.06	4.4 ± 1.4
258 ± 3	89.5 ± 7.2	0.14 ± 0.01	2.2 ± 0.3
264 ± 2	63.2 ± 7.6	0.22 ± 0.02	3.7 ± 0.7
281 ± 2	79.5 ± 3.7	0.37 ± 0.03	4.9 ± 0.7
282 ± 2	52.3 ± 12.9	0.07 ± 0.01	1.3 ± 0.2
282 ± 2	53.6 ± 8.7	0.1 ± 0.01	2.2 ± 0.4
283 ± 1	58.1 ± 1.9	0.33 ± 0.03	8 ± 1.4
286 ± 2	52.4 ± 2.9	0.27 ± 0.02	5.7 ± 0.8
295 ± 2	57.3 ± 4.4	0.28 ± 0.04	5 ± 1.2
300 ± 2	59.4 ± 4.7	0.15 ± 0.02	3.2 ± 0.6
347 ± 3	21.2 ± 3.2	NaN	NaN
355 ± 4	55.1 ± 3	0.19 ± 0.01	4.1 ± 0.7
355 ± 4	28.5 ± 1.8	0.11 ± 0.01	4.6 ± 1.2
357 ± 3	23.8 ± 4.4	0.03 ± 0	1.3 ± 0.3
362 ± 3	20.5 ± 3.4	0.02 ± 0	1.1 ± 0.2
378 ± 4	53.6 ± 7.7	0.05 ± 0	0.9 ± 0.2
394 ± 3	13.6 ± 1.7	NaN	NaN
401 ± 1	8.6 ± 1.7	NaN	NaN
407 ± 4	3.3 ± 1.9	0.06 ± 0	25.3 ± 14

APPENDIX D. UNCERTAINTY CALCULATION FOR THE SODIUM CAPILLARY PUMPING EXPERIMENT

The mass flowrate of liquid sodium $\dot{m}$ during the capillary pumping experiments described in Chapter 5 is calculated using Equation D.1, which accounts for thermal expansion in the upper flange by incorporating an effective length L_{eff}. This expression is a function of eight variables, six of which have an associated uncertainty: the effective cross sectional area in the electrode prism A_c; the density of sodium ρ_n, ρ_m when it is in contact with electrodes n and m; the distance between electrodes L_{elec}; the internal volume in the upper plenum up to electrode #1 V_1 (see Figure 5.8a); and the time difference between electrode activations Δt. For all dimensions, the machining tolerance is assumed to be ± 0.13 mm. This leads to a value of V_1 = 337 mm^3 ± 15.7 mm^3 for the upper flange internal volume and L_{elec} = 3.3 mm ± 0.13 mm for the distance between electrodes. The flow volume in the electrode prism consists of the cylindrical flow path and the extra machined volume where each electrode is cemented into place. An effective cross sectional area is defined with a hydraulic diameter to account for the change in cross section as sodium flows upwards. The effective cross-section area is found to be A_c = 1.33 mm^2 ± 0.384 mm^2, which represents the largest source of uncertainty in this experiment. The sodium density when it first makes contact with each electrode is calculated at two geometric-averaged temperatures (T_{out} and the bottom/top of the electrode prism) along the flow path.[120] The sodium density at these two temperatures represents the total range, so the total density and its uncertainty is then calculated following the recommendation in the NIST Technical Note 1297 for data uniformly distributed within a band that practically

represents 100% of the possible values. [156] This is a conservative estimate of the liquid sodium density. Finally, the uncertainty in the electrode activation time is conservatively assumed to be ± 1 h. After calculating the uncertainties for each variable, the total uncertainty for the mass flowrate is then determined using the propagation of error formula (Equation D.2). [156] The total mass flowrate $\dot{m}_{meas}$ is the average of the mass flowrate $\dot{m}$ between each successive electrode activation. The total mass flowrate has two associated uncertainties: the standard error found using a Student's T-test statistic, and the propagation of error for the uncertainties of each value (calculated using Equation D.2 for each $\dot{m}$ between successive electrode activations). The total standard uncertainty is conservatively reported as the square root of the sum of these two contributions.

$$\dot{m} = \frac{\rho_n A_c}{\Delta t} L_{eff} = \frac{\rho_n A_c}{\Delta t}\left((m-n) L_{elec} - \left(\frac{\rho_n}{\rho_m} - 1 \right)\left((n-1) L_{elec} + \frac{V_1}{A_c} \right)\right) \tag{D.1}$$

$$f = f\left(x_1, x_2, \ldots, x_j\right) \quad \rightarrow \quad \delta f = \sqrt{\sum_{i=1}^{i=j} \left(\frac{\partial f}{\partial x_i} \right)^2 \left(\delta x_i \right)^2} \tag{D.2}$$

REFERENCES

1. *International Energy Outlook 2019*. 2019, United States Energy Information Administration. p. 56.

2. Chum, H.L. and R.A. Osteryoung, *Review of thermally regenerative electrochemical systems*. 1981, Solar Energy Research Inst., Golden, CO (USA); State Univ. of New York, Buffalo (USA).

3. Kennedy, J.H., *The β-aluminas*, in *Solid Electrolytes*. 1977, Springer Berlin Heidelberg. p. 105-141.

4. Fergus, J.W., *Ion transport in sodium ion conducting solid electrolytes.* Solid State Ionics, 2012. **227**(0): p. 102-112.

5. Ptácek, P., *Processes during Thermal Treatment*. Strontium Aluminate - Cement Fundamentals, Manufacturing, Hydration, Setting Behaviour and Applications. 2014.

6. Weber, N., *A thermoelectric device based on beta-alumina solid electrolyte.* Energy Conversion, 1974. **14**(1): p. 1-8.

7. Nakata, H., et al., *Ceramic electrodes for an alkali metal thermo-electric converter (AMTEC).* Journal of Applied Electrochemistry, 1993. **23**(12): p. 1251-1258.

8. Moran, M.J. and H.N. Shapiro, *Fundamentals of engineering thermodynamics*. 6th ed. 2008, Hoboken, NJ: Wiley. xv. 928 p.

9. Vining, C.B., et al., *Reversible Thermodynamic Cycle for AMTEC Power Conversion.* Journal of The Electrochemical Society, 1993. **140**(10): p. 2760-2763.

10. Lodhi, M.A.K., P. Vijayaraghavan, and A. Daloglu, *Simulation and analysis of time-dependent degradation behavior of AMTEC.* Journal of Power Sources, 2001. **96**(2): p. 343-351.

11. Wu, S.-Y., L. Xiao, and Y.-D. Cao, *A review on advances in alkali metal thermal to electric converters (AMTECs).* International Journal of Energy Research, 2009. **33**(10): p. 868-892.

12. Zebarjadi, M., et al., *Perspectives on thermoelectrics: from fundamentals to device applications.* Energy & Environmental Science, 2012. **5**(1): p. 5147-5162.

13. Vining, C.B., *An inconvenient truth about thermoelectrics.* Nature Materials, 2009. **8**(2): p. 83-85.

14. Wachsman, E.D. and K.T. Lee, *Lowering the Temperature of Solid Oxide Fuel Cells.* Science, 2011. **334**(6058): p. 935.

15. Kummer, J.T. and N. Weber, *Thermo-electric generator*. 1969, Google Patents.

16. Cole, T., *Thermoelectric Energy Conversion with Solid Electrolytes.* Science, 1983. **221**(4614): p. 915-920.

17. Bankston, C.P., et al., *Experimental and Systems Studies of the Alkali Metal Thermoelectric Converter for Aerospace Power.* Journal of Energy, 1983. **7**(5): p. 442-448.

18. Williams, R.M., et al., *Kinetics and Transport at AMTEC Electrodes: I . The Interfacial Impedance Model.* Journal of The Electrochemical Society, 1990. **137**(6): p. 1709-1716.

19. Williams, R.M., et al., *Kinetics and Transport at AMTEC Electrodes: II . Temperature Dependence of the Interfacial Impedance of Na(g)/Porous Mo/Na-Beta' Alumina.* Journal of The Electrochemical Society, 1990. **137**(6): p. 1716-1723.

20. Underwood, M.L., et al., *An AMTEC vapor-vapor, series connected cell.* AIP Conference Proceedings, 1992. **246**(1): p. 1331-1337.

21. Hendricks, T.J., H. Chendong, and R.K. Sievers. *AMTEC radioisotope power system design and analysis for Pluto Express Fly-By*. in *IECEC-97 Proceedings of the Thirty-Second Intersociety Energy Conversion Engineering Conference (Cat. No.97CH6203)*. 1997.

22. Tournier, J.M., et al. *Performance analysis of a multitube vapor-anode AMTEC cell*. in *Energy Conversion Engineering Conference, 1997. IECEC-97., Proceedings of the 32nd Intersociety*. 1997.

23. Merrill, J.M. and C. Mayberry, *Experimental investigation of multi-AMTEC cell ground demonstration converter systems based on PX-3 and PX-5 series AMTEC cells.* AIP Conference Proceedings, 1999. **458**(1): p. 1369-1377.

24. Hunt, T.K., N. Weber, and T. Cole, *High efficiency thermoelectric conversion with beta"-alumina electrolytes, the sodium heat engine.* Solid State Ionics, 1981. **5**(0): p. 263-265.

25. Merrill, J.M., M. Schuller, and L. Huang, *Vacuum testing of high efficiency multi-base tube AMTEC cells: February 1997–October 1997.* AIP Conference Proceedings, 1998. **420**(1): p. 1613-1620.

26. El-Genk, M.S. and J.-M.P. Tournier, *AMTEC/TE static converters for high energy utilization, small nuclear power plants.* Energy Conversion and Management, 2004. **45**(4): p. 511-535.

27. Wu, S.-Y., et al., *A new AMTEC/TAR hybrid system for power and cooling cogeneration.* Energy Conversion and Management, 2019. **180**: p. 206-217.

28. Ramos, N.D.d.l.R., et al., *Design and construction of the ATEFA facility for experimental investigations of AMTEC test modules.* IOP Conference Series: Materials Science and Engineering, 2017. **228**(1): p. 012014.

29. Onea, A., et al., *AMTEC CLUSTERS FOR POWER GENERATION IN A CONCENTRATED SOLAR POWER PLANT.* Magnetohydrodynamics (0024-998X), 2015. **51**(3).

30. Peng, W., et al., *The optimal operation states and parametric choice strategies of a DCFC-AMTEC coupling system with high efficiency.* Energy Conversion and Management, 2019. **195**: p. 360-366.

31. Açıkkalp, E., L. Chen, and M.H. Ahmadi, *Comparative performance analyses of molten carbonate fuel cell-alkali metal thermal to electric converter and molten carbonate fuel cell-thermo-electric generator hybrid systems.* Energy Reports, 2020. **6**: p. 10-16.

32. Suitor, J.W., et al., *Thermal modeling of AMTEC recirculating cell.* AIP Conference Proceedings, 1992. **246**(1): p. 1325-1330.

33. Schock, A., H. Noravian, and O. Chuen. *Coupled thermal, electrical, and fluid flow analyses of AMTEC converters, with illustrative application to OSC's cell design*. in *Energy Conversion Engineering Conference, 1997. IECEC-97., Proceedings of the 32nd Intersociety*. 1997.

34. Lodhi, M.A.K. and A. Daloglu, *Effect of geometrical variations on AMTEC cell heat losses.* Journal of Power Sources, 2000. **91**(2): p. 99-106.

35. Lodhi, M.A.K. and A. Daloglu, *Design and material variation for an improved power output of AMTEC cells.* Journal of power sources, 2001. **93**(1): p. 32-40.

36. Lodhi, M.A.K. and V.R. Malka, *Optimization of the TIEC/AMTEC cascade cell for high efficiency.* Journal of Power Sources, 2006. **156**(2): p. 685-691.

37. Hendricks, T.J. and C. Huang, *High-Performance Radial AMTEC Cell Design for Ultra-High-Power Solar AMTEC Systems.* Journal of Solar Energy Engineering, 2000. **122**(2): p. 49-55.

38. Wu, S.-Y., et al., *A parabolic dish/AMTEC solar thermal power system and its performance evaluation.* Applied Energy, 2010. **87**(2): p. 452-462.

39. Lee, W.-H., et al., *Study on the Characteristics of an Alkali-Metal Thermoelectric Power Generation System.* Journal of Electronic Materials, 2015. **44**(10): p. 3534-3544.

40. El-Genk, M.S. and J.-M.P. Tournier, *"SAIRS" — Scalable Amtec Integrated Reactor space power System.* Progress in Nuclear Energy, 2004. **45**(1): p. 25-69.

41. Yuan, Y., et al., *Accident analysis of heat pipe cooled and AMTEC conversion space reactor system.* Annals of Nuclear Energy, 2016. **94**: p. 706-715.

42. Ge, L., H. Li, and J. Shan, *Reliability and loading-following studies of a heat pipe cooled, AMTEC conversion space reactor power system.* Annals of Nuclear Energy, 2019. **130**: p. 82-92.

43. Tournier, J.-M. and M.S. El-Genk, *AMTEC Performance and Evaluation Analysis Model (APEAM): Comparison with test results of PX-4C, PX-5A, and PX-3A cells.* AIP Conference Proceedings, 1998. **420**(1): p. 1576-1585.

44. Tournier, J.-M. and M.S. El-Genk, *Sodium vapor pressure losses in a multitube, alkali-metal thermal-to-electric converter.* Journal of thermophysics and heat transfer, 1999. **13**(1): p. 117-125.

45. Tournier, J.M. and M.S. El-Genk, *An electric model of a vapour anode, multitube alkali–metal thermal-to-electric converter.* Journal of Applied Electrochemistry, 1999. **29**(11): p. 1263-1275.

46. Tournier, J.-M. and M.S. El-Genk, *Radiation/conduction model for multitube AMTEC cells.* AIP Conference Proceedings, 1998. **420**(1): p. 1552-1564.

47. Tournier, J.-M. and M.S. El-Genk, *Performance analysis of Pluto/Express, multitube AMTEC cells.* Energy Conversion and Management, 1999. **40**(2): p. 139-173.

48. Tournier, J.M.P. and M.S. El-Genk, *Radiation Heat Transfer in Multitube, Alkali-Metal Thermal-to-Electric Converter.* Journal of Heat Transfer, 1999. **121**(1): p. 239-245.

49. Tournier, J.-M. and M.S. El-Genk, *A thermal model of the conical evaporator in Pluto/Express, multi-tube AMTEC cells.* AIP Conference Proceedings, 1999. **458**(1): p. 1526-1533.

50. Wang, Q., et al., *Analysis of the performance of an alkali metal thermoelectric converter (AMTEC) based on a lumped thermal-electrochemical model.* Applied Energy, 2018. **216**: p. 195-211.

51. Zhu, L., et al., *Optimization of vapor anode multi-tube alkali metal thermoelectric converter based on an integrated model.* Applied Energy, 2020. **259**: p. 114117.

52. Hunt, T.K., et al. *AMTEC/SHE for space nuclear power applications*. in *AIP Conference Proceedings*. 1992. AIP.

53. Sievers, R., et al., *Operation of low temperature AMTEC cells*. 1992, SAE Technical Paper.

54. Anderson, W.G., *Sodium wick pumping experiments for a vapor-fed AMTEC system*. 1992, SAE Technical Paper.

55. Crowley, C.J. and M.G. Izenson, *Condensation of sodium on a micromachined surface for AMTEC.* AIP Conference Proceedings, 1993. **271**(2): p. 897-904.

56. Crowley, C., et al. *Performance of a wick return AMTEC cell with a micromachined condenser*. in *Intersociety Energy Conversion Engineering Conference*. 1994.

57. El-Genk, M.S. and J.-M. Tournier, *Optimization of liquid-return artery in a vapor-anode, multitube AMTEC.* AIP Conference Proceedings, 1998. **420**(1): p. 1586-1594.

58. Tournier, J.-M. and M.S. El-Genk, *Capillary Limit of Evaporator Wick in Alkali Metal Thermal-to-Electric Converters.* Journal of Thermophysics and Heat Transfer, 2002. **16**(1): p. 141-153.

59. Wu, S.-Y., et al., *Parametric study on flow and heat transfer characteristics of porous wick evaporator based on AMTEC.* Journal of Mechanical Science and Technology, 2012. **26**(3): p. 973-981.

60. Wu, S.-Y., X.-F. Zheng, and L. Xiao, *Phase change heat transfer characteristics of porous wick evaporator with bayonet tube and alkali metal as working fluid.* International Journal of Thermal Sciences, 2018. **126**: p. 152-161.

61. Xiao, L., et al., *Parametric Analysis of Condensation Heat Transfer Characteristics of AMTEC Wick Condenser.* Energy Procedia, 2017. **105**: p. 4698-4705.

62. Xiao, L., et al., *Condensation heat transfer characteristics of the alkali metal thermal to electric converter (AMTEC) porous wick condenser.* Thermal Science, 2019. **23**(3 Part B): p. 1911-1922.

63. Hoffman, E.E. and W.D. Manly, *Corrosion Resistance of Metals and Alloys to Sodium and Lithium*, in *Handling and Uses of the Alkali Metals*. 1957, American Chemical Society. p. 82-91.

64. Kamdar, M.H., *Embrittlement by liquid metals.* Progress in Materials Science, 1973. **15**(4): p. 289-374.

65. Rodríguez-Valverde, M.Á. and M. Tirado Miranda, *Derivation of Jurin's law revisited.* European Journal of Physics, 2010. **32**(1): p. 49-54.

66. Bard, A.J. and L.R. Faulkner, *Electrochemical methods : fundamentals and applications*. 2nd ed. 2001, New York: Wiley. xxi, 833 p.

67. Gautam, D., *Characterization of the conduction properties of alkali metal ion conducting solid electrolytes using thermoelectric measurements*. 2006, Universitat Stuttgart.

68. Koryta, J.i., J.i. Dvořák, and L. Kavan, *Principles of electrochemistry*. 2nd ed. 1993, Chichester ; New York: Wiley. xv, 486 p.

69. Steinbruck, M., et al. *Investigations of beta-alumina solid electrolytes for application in AMTEC cells*. in *Intersociety Energy Conversion Engineering Conference*. 1993. AMERICAN NUCLEAR SOCIETY.

70. Tournier, J.-M., et al., *An analytical model for liquid-anode and vapor-anode AMTEC converters.* AIP Conference Proceedings, 1997. **387**(1): p. 1543-1552.

71. Diez de los Rios Ramos, N., et al. *Direct energy conversion of heat to electricity using AMTEC*. in *Energy (IYCE), 2015 5th International Youth Conference on*. 2015.

72. Makansi, M.M., C.H. Muendel, and W.A. Selke, *Determination of the Vapor Pressure of Sodium.* The Journal of Physical Chemistry, 1955. **59**(1): p. 40-42.

73. Kennard, E.H., *Kinetic theory of gases, with an introduction to statistical mechanics*. 1st ed. International series in physics. 1938, New York, London,: McGraw-Hill Book Company, inc. xiii, 483 p.

74. Khayet, M., *Membranes and theoretical modeling of membrane distillation: A review.* Advances in Colloid and Interface Science, 2011. **164**(1): p. 56-88.

75. Schuller, M., U. Azimov, and T. Lalk, *Effect of sample configuration on AMTEC electrode/electrolyte characteristics measurements in a sodium exposure test cell.* Journal of The Electrochemical Society, 2002. **149**(11): p. A1432-A1436.

76. Fuller, T.F. and J.N. Harb, *Electrochemical engineering*. First edition. ed. 2018, Hoboken, NJ, USA: Wiley. xv, 417 pages.

77. Limia, A., et al., *A dual-stage sodium thermal electrochemical converter (Na-TEC).* Journal of Power Sources, 2017. **371**(Supplement C): p. 217-224.

78. Borkowski, C.A., R.C. Svedberg, and T.J. Hendricks. *Parasitic heat loss reduction in AMTEC cells by heat shield optimization*. in *IECEC-97 Proceedings of the Thirty-Second Intersociety Energy Conversion Engineering Conference (Cat. No.97CH6203)*. 1997.

79. Limia, A., et al., *A dual-stage sodium thermal electrochemical converter (Na-TEC).* Journal of Power Sources, 2017. **371**: p. 217-224.

80. Bahiraei, F., et al., *A pseudo 3D electrochemical-thermal modeling and analysis of a lithium-ion battery for electric vehicle thermal management applications.* Applied Thermal Engineering, 2017. **125**: p. 904-918.

81. Jaguemont, J., et al., *Streamline three-dimensional thermal model of a lithium titanate pouch cell battery in extreme temperature conditions with module simulation.* Journal of Power Sources, 2017. **367**: p. 24-33.

82. Zhang, Y., et al., *A model predicting performance of proton exchange membrane fuel cell stack thermal systems.* Applied Thermal Engineering, 2004. **24**(4): p. 501-513.

83. Limia, A., et al., *Thermal modeling and efficiency of a dual-stage sodium heat engine.* Applied Thermal Engineering, 2018. **145**: p. 603-609.

84. King, J.C. and M.S. El-Genk, *Review of refractory materials for alkali metal thermal-to-electric conversion cells.* Journal of Propulsion and Power, 2001. **17**(3): p. 547-556.

85. Zhao, R., et al., *Heat transfer in upper part of electrolytic cells: Thermal circuit and sensitivity analysis.* Applied Thermal Engineering, 2013. **54**(1): p. 212-225.

86. Incropera, F.P., *Fundamentals of heat and mass transfer / Frank P. Incropera ... [et al.]*. 6th ed. 2007, Hoboken, NJ: John Wiley. xxv, 997 p.

87. Ryan, M.A., et al., *Thermophysical properties of sodium β"-alumina polycrystalline ceramic.* Journal of Physics and Chemistry of Solids, 1994. **55**(11): p. 1255-1260.

88. Dunning, E., *The thermodynamic and transport properties of sodium and sodium vapor*. 1960, Argonne National Lab., Ill.

89. Munson, B.R., et al., *Fundamentals of fluid mechanics*. 7th edition. ed. 2013, Hoboken, NJ: John Wiley & Sons, Inc. xix, 747, 6, 10 pages.

90. Vanderhaegen, M. and A.L. Belguet, *A Review on Sodium Boiling Phenomena in Reactor Systems.* Nuclear Science and Engineering, 2014. **176**(2): p. 115-137.

91. Howell, J.R., *A catalog of radiation configuration factors*. 1982: McGraw-Hill Book Company.

92. Modest, M.F., *Radiative heat transfer*. Third Edition. ed. 2013, New York: Academic Press. xxii, 882 pages.

93. Hattori, N., H. Takasu, and T. Iguchi, *Emissivity of liquid sodium.* Nippon Kikai Gakkai Ronbunshu, B Hen, 1983. **49**(447): p. 2493-2496.

94. Barker, M.G. and D.J. Wood, *The corrosion of chromium, iron, and stainless steel in liquid sodium.* Journal of the Less Common Metals, 1974. **35**(2): p. 315-323.

95. Paradis, P.-F., et al., *Thermophysical properties of vanadium at high temperature measured with an electrostatic levitation furnace.* The Journal of Chemical Thermodynamics, 2002. **34**(12): p. 1929-1942.

96. Yee, S.K., et al., *$ per W metrics for thermoelectric power generation: beyond ZT.* Energy & Environmental Science, 2013. **6**(9): p. 2561-2571.

97. Gunawan, A., et al. *Techno-Economic Analysis of Dual-Stage Sodium Thermal Electrochemical Converter (Na-TEC) Power Block for Distributed CSP*. in *ASME 2018 12th International Conference on Energy Sustainability collocated with the ASME 2018 Power Conference and the ASME 2018 Nuclear Forum*. 2018.

98. *National Minerals Information Center: Commodity Statistics and Information*. 2019; Available from: https://minerals.usgs.gov/minerals/pubs/commodity/.

99. Hunt, T.K., *Study of costs for a 1 kWe Sodium Heat Engine/AMTEC system*. 1992, SAE Technical Paper.

100. Gunawan, A., *Cost-Scaling Analysis of Dual-Stage Sodium Thermal Electrochemical Converter (Na-TEC) Power Block for Distributed CSP*, in *2018 Solar Energy Technologies Office Portfolio Review*. 2018: Washington D.C.

101. Gunawan, A., et al., *A Cost-Performance Analysis of a Sodium Heat Engine for Distributed Concentrating Solar Power.* Advanced Sustainable Systems, 2020. **n/a**(n/a): p. 1900104.

102. Rubiolo, P., *Novel, Integrated Reactor/Power Conversion System (LMR-AMTEC).* 2003, Westinghouse Electric Company LLC (US).

103. Ivanenok III, J.F. and R.K. Sievers, *500 Watt Solar AMTEC Power System for Small Spacecraft*. 1995, Advanced Modular Power Systems Inc., Ann Arbor, MI.

104. Ghiaasiaan, S.M., *Two-phase flow, boiling and condensation in conventional and miniature systems*. 2017, New York, NY, USA: Cambridge University Press. pages cm.

105. Gennes, P.-G.d., F.o. Brochard-Wyart, and D. Quéré, *Capillarity and wetting phenomena : drops, bubbles, pearls, waves*. 2004, New York: Springer. xv, 291 p.

106. Smith, J.D., I. Chatzis, and M.A. Ioannidis, *A New Technique to Measure the Breakthrough Capillary Pressure.* Journal of Canadian Petroleum Technology, 2005. **44**(11): p. 7.

107. Chatzis, I. and F.A.L. Dullien, *Mercury porosimetry curves of sandstones. Mechanisms of mercury penetration and withdrawal.* Powder Technology, 1981. **29**(1): p. 117-125.

108. Turner, G., *Liquid Metal Flow Measurement (Sodium) State-of-the-Art Study*. 1968, Atomics International, Canoga Park, Calif. Liquid Metal Engineering Center.

109. Schulenberg, T. and R. Stieglitz, *Flow measurement techniques in heavy liquid metals.* Nuclear Engineering and Design, 2010. **240**(9): p. 2077-2087.

110. Taylor, J. and S. Ford, *Solid Metal-Liquid Metal Interaction Studies. Part II. Contact Angle Relationships for Sodium on Solids*. 1955, United Kingdom Atomic Energy Authority. Research Group. Atomic Energy Research Establishment, Harwell, Berks, England (United Kingdom).

111. Bader, M. and C.A. Busse, *Wetting by sodium at high temperatures in pure vapour atmosphere.* Journal of Nuclear Materials, 1977. **67**(3): p. 295-300.

112. Cummerow, R. and J. Read, *An Experiment on the Rise of Liquid Sodium in Capillary Grooves*. 1951, Knolls Atomic Power Lab.

113. Ganesan, V. and V. Ganesan, *Corrosion of annealed AISI 316 stainless steel in sodium environment.* Journal of Nuclear Materials, 1998. **256**(1): p. 69-77.

114. Wang, J., et al., *Fundamental study on the wetting property of liquid lithium.* Energy Storage Materials, 2018. **14**: p. 345-350.

115. Washburn, E.W., *The dynamics of capillary flow*. Physical review, 1921. **17**(3): p. 273.

116. Mayer, R.P. and R.A. Stowe, *Mercury Porosimetry: Filling of Toroidal Void Volume Following Breakthrough between Packed Spheres.* The Journal of Physical Chemistry, 1966. **70**(12): p. 3867-3873.

117. Mason, G. and N.R. Morrow, *Meniscus Configurations and Curvatures in Non-Axisymmetric Pores of Open and Closed Uniform Cross Section.* Proceedings of the Royal Society of London. Series A, Mathematical and Physical Sciences, 1987. **414**(1846): p. 111-133.

118. Mayer, R.P. and R.A. Stowe, *Mercury porosimetry—breakthrough pressure for penetration between packed spheres.* Journal of Colloid Science, 1965. **20**(8): p. 893-911.

119. Huizenga, D. and D.M. Smith, *Knudsen diffusion in random assemblages of uniform spheres.* AIChE Journal, 1986. **32**(1): p. 1-6.

120. Fink, J. and L. Leibowitz, *Thermodynamic and transport properties of sodium liquid and vapor*. 1995, Argonne National Lab.

121. Carey, V.P., *Liquid-vapor phase-change phenomena : an introduction to the thermophysics of vaporization and condensation processes in heat transfer equipment*. 2nd ed. 2008, New York: Taylor and Francis. xxii, 742 p.

122. Suzuki, T., et al., *Sodium corrosion behavior of austenitic alloys and selective dissolution of chromium and nickel.* Journal of Nuclear Materials, 1986. **139**(2): p. 97-105.

123. Campbell, C., C. Tyzack, and U.A.E. AUTHORITY, *A preliminary model for the carburization of stainless steel at high temperatures in sodium containing carbon at unit activity.* ALKALI: p. 159.

124. Nield, D.A. and A. Bejan, *Convection in porous media*. 4th ed. 2013, New York: Springer Science+Business Media. xxv, 778 p.

125. Bird, R.B., W.E. Stewart, and E.N. Lightfoot, *Transport phenomena*. 2nd, Wiley international ed. 2002, New York: J. Wiley. xii, 895 p.

126. Kennedy, D.P., *Spreading Resistance in Cylindrical Semiconductor Devices.* Journal of Applied Physics, 1960. **31**(8): p. 1490-1497.

127. Rumpf, H.C.H. and A.R. Gupte, *Einflüsse der Porosität und Korngrößenverteilung im Widerstandsgesetz der Porenströmung.* Chemie Ingenieur Technik, 1971. **43**(6): p. 367-375.

128. Higdon, J.J.L. and G.D. Ford, *Permeability of three-dimensional models of fibrous porous media.* Journal of Fluid Mechanics, 2006. **308**: p. 341-361.

129. Dullien, F.A.L., *Porous media : fluid transport and pore structure*. 2nd ed. 1992, San Diego: Academic Press. xx, 574 p.

130. Manly, W.D., U.S.A.E. Commission, and L. Oak Ridge National, *Fundamentals of liquid-metal corrosion*. At head of title:Metallurgy Division. 1956, Oak Ridge, Tenn.: Oak Ridge National Laboratory. iii, 10 p.

131. Hsu, C.T. and P. Cheng, *Thermal dispersion in a porous medium.* International Journal of Heat and Mass Transfer, 1990. **33**(8): p. 1587-1597.

132. Beck, J.L., *Convection in a box of porous material saturated with fluid.* The Physics of Fluids, 1972. **15**(8): p. 1377-1383.

133. Ghiaasiaan, S.M., *Convective heat and mass transfer*. 2011, Cambridge ; New York: Cambridge University Press. xxiv, 524 p.

134. Hossain, M.A., K. Vafai, and K.M.N. Khanafer, *Non-Darcy natural convection heat and mass transfer along a vertical permeable cylinder embedded in a porous medium.* International Journal of Thermal Sciences, 1999. **38**(10): p. 854-862.

135. Ho, C.K. and S.W. Webb, *Gas transport in porous media*. Theory and applications of transport in porous media. 2006, Dordrecht: Springer. vii, 444 p.

136. Veleckis, E., et al., *Solubility of helium and argon in liquid sodium.* The Journal of Physical Chemistry, 1971. **75**(18): p. 2832-2838.

137. Galvin, K.P., *A conceptually simple derivation of the Kelvin equation.* Chemical Engineering Science, 2005. **60**(16): p. 4659-4660.

138. Kumada, T., R. Ishiguro, and Y. Kimachi, *Diffusion Coefficients of Sodium Vapors in Argon and Helium.* Nuclear Science and Engineering, 1979. **70**(1): p. 73-81.

139. Pollard, W.G. and R.D. Present, *On Gaseous Self-Diffusion in Long Capillary Tubes.* Physical Review, 1948. **73**(7): p. 762-774.

140. Vignoles, G., *Modelling Binary, Knudsen and Transition Regime Diffusion Inside Complex Porous Media.* Journal De Physique Iv - J PHYS IV, 1995. **05**.

141. Shen, L. and Z. Chen, *Critical review of the impact of tortuosity on diffusion.* Chemical Engineering Science, 2007. **62**: p. 3748-3755.

142. Pisani, L., *Simple Expression for the Tortuosity of Porous Media.* Transport in Porous Media, 2011. **88**(2): p. 193-203.

143. Tjaden, B., et al., *On the origin and application of the Bruggeman correlation for analysing transport phenomena in electrochemical systems.* Current Opinion in Chemical Engineering, 2016. **12**: p. 44-51.

144. Munson, B.R., T.H. Okiishi, and W.W. Huebsch, *Fundamentals of fluid mechanics*. 6th ed. 2009, Hoboken, NJ: J. Wiley & Sons.

145. Reay, D., R. McGlen, and P. Kew, *Heat Pipes : Theory, Design and Applications*. 2013, Oxford, UNITED KINGDOM: Elsevier Science & Technology.

146. Kaviany, M., *Principles of heat transfer in porous media*. 2nd ed. Mechanical engineering series. 1995, New York: Springer-Verlag. xxii, 708 p.

147. Kim, S.J. and S.P. Jang, *Effects of the Darcy number, the Prandtl number, and the Reynolds number on local thermal non-equilibrium.* International Journal of Heat and Mass Transfer, 2002. **45**(19): p. 3885-3896.

148. Wakao, N., S. Kaguei, and T. Funazkri, *Effect of fluid dispersion coefficients on particle-to-fluid heat transfer coefficients in packed beds: Correlation of nusselt numbers.* Chemical Engineering Science, 1979. **34**(3): p. 325-336.

149. Torabi, M., et al., *Challenges and progress on the modelling of entropy generation in porous media: A review.* International Journal of Heat and Mass Transfer, 2017. **114**: p. 31-46.

150. Nield, D.A., *Resolution of a Paradox Involving Viscous Dissipation and Nonlinear Drag in a Porous Medium.* Transport in Porous Media, 2000. **41**(3): p. 349-357.

151. Mason, E.A. and S.C. Saxena, *Thermal Conductivity of Multicomponent Gas Mixtures. II.* The Journal of Chemical Physics, 1959. **31**(2): p. 511-514.

152. Udell, K.S., *Heat transfer in porous media considering phase change and capillarity—the heat pipe effect.* International Journal of Heat and Mass Transfer, 1985. **28**(2): p. 485-495.

153. Hanamura, K. and M. Kaviany, *Propagation of condensation front in steam injection into dry porous media.* International journal of heat and mass transfer, 1995. **38**(8): p. 1377-1386.

154. Choudhary, M.K., K.C. Karki, and S.V. Patankar, *Mathematical modeling of heat transfer, condensation, and capillary flow in porous insulation on a cold pipe.* International Journal of Heat and Mass Transfer, 2004. **47**(26): p. 5629-5638.

155. Miljkovic, N., et al., *Jumping-Droplet-Enhanced Condensation on Scalable Superhydrophobic Nanostructured Surfaces.* Nano Letters, 2013. **13**(1): p. 179-187.

156. Taylor, B.N. and C.E. Kuyatt, *Guidelines for evaluating and expressing the uncertainty of NIST measurement results.* 1994.

157. Mugele, F. and J.-C. Baret, *Electrowetting: from basics to applications.* Journal of Physics: Condensed Matter, 2005. **17**(28): p. R705-R774.

158. Cavalli, A., et al., *Electrically induced drop detachment and ejection.* Physics of Fluids, 2016. **28**(2): p. 022101.

159. Gunawan, A., et al. *Brazings for Metal-Ceramic Joining in Sodium Thermal Electrochemical Converter (Na-TEC) Devices*. in *ASME 2018 12th International Conference on Energy Sustainability collocated with the ASME 2018 Power Conference and the ASME 2018 Nuclear Forum*. 2018.

160. Khalkhali, H., A. Faghri, and Z.J. Zuo, *Entropy generation in a heat pipe system.* Applied Thermal Engineering, 1999. **19**(10): p. 1027-1043.

161. Bejan, A., *Entropy generation minimization: the method of thermodynamic optimization of finite-size systems and finite-time processes*. 2013: CRC press.

162. Gorla, R.S.R., L.W. Byrd, and D.M. Pratt, *Entropy minimization in micro-scale evaporating thin liquid film in capillary tubes.* Heat and Mass Transfer, 2008. **45**(2): p. 131-138.